Rotating Split-Cylinder Flows

by

Paloma Gutierrez Castillo

A Dissertation Presented in Partial Fulfillment
of the Requirements for the Degree
Doctor of Philosophy

Approved April 2017 by the
Graduate Supervisory Committee:

Juan M. Lopez, Chair
Marcus Herrmann
Rodrigo Platte
Bruno Welfert
Wenbo Tang

ARIZONA STATE UNIVERSITY

May 2017

ABSTRACT

The three-dimensional flow contained in a rapidly rotating circular split cylinder is studied numerically solving the Navier–Stokes equations. The cylinder is completely filled with fluid and is split at the midplane. Three different types of boundary conditions were imposed, leading to a variety of instabilities and complex flow dynamics.

The first configuration has a strong background rotation and a small differential rotation between the two halves. The axisymmetric flow was first studied identifying boundary layer instabilities which produce inertial waves under some conditions. Limit cycle states and quasiperiodic states were found, including some period doubling bifurcations. Then, a three-dimensional study was conducted identifying low and high azimuthal wavenumber rotating waves due to Görtler and Tollmien—Schlichting type instabilities. Over most of the parameter space considered, quasiperiodic states were found where both types of instabilities were present.

In the second configuration, both cylinder halves are in exact counter-rotation, producing an O(2) symmetry in the system. The basic state flow dynamic is dominated by the shear layer created in the midplane. By changing the speed rotation and the aspect ratio of the cylinder, the flow loses symmetries in a variety of ways creating static waves, rotating waves, direction reversing waves and slow-fast pulsing waves. The bifurcations, including infinite-period bifurcations, were characterized and the flow dynamics was elucidated. Additionally, preliminary experimental results for this case are presented.

In the third set up, with oscillatory boundary conditions, inertial wave beams were forced imposing a range of frequencies. These beams emanate from the corner of the cylinder and from the split at the midplane, leading to destructive/constructive interactions which produce peaks in vorticity for some specific frequencies. These frequencies are shown to be associated with the resonant Kelvin modes. Furthermore,

a study of the influence of imposing a phase difference between the oscillations of the two halves of the cylinder led to the interesting result that different Kelvin modes can be excited depending on the phase difference.

DEDICATION

To my family.

ACKNOWLEDGMENTS

First of all, I want to thank my advisor Dr. Juan Lopez for providing me a great support and the necessary tools for becoming and independent researcher in the future. It was a pleasure to discuss with him several topics about our research and admire how he is able to summarize and relate diverse fluid mechanics topics and studies published in the last 20 years. He did so while always transferring his passion about our research and the feeling that the areas to expand our research are infinite. Having the opportunity of traveling with him to some international conferences and knowing some of his collaborators was also extraordinary. Thanks also to the rest of his family for receiving me as another member of it.

Thanks to Arizona State University which provided me the opportunity of persuading a PhD and gave me the great experiences of sharing my research interest with well-known Professors and provide me the wonderful opportunity of teaching my own classes. Especially important for my development as a researcher was the period in which we had weekly group meetings started with the graduate students Jason Yalim and Ke Wu. Later expanded with my advisor and Dr. Welfert who always has an interesting point of view and asked me intriguing questions that prepare me for future talks. I would also like to thank the remainder of my committee. Dr. Marcus Herrmann whose passion teaching is extraordinary, I got a lot of insight about fluid mechanics in the three classes I took with him. Dr. Rodrigo Platte whose computational classes were crucial for my training including learning about spectral methods. Dr. Wenbo Tang who during his class first introduce me most of the dynamical systems concepts. I also want to remark the personal help obtained outside the classroom at ASU. I am very thankful with Dr. Katie Kolossa who was always there to gave me any advice that I would need. I also want to thanks Debbie Olson who was taking care of me since the first week that I arrive at ASU.

I want to mention all the Professors that since I was a child helped me growing up and developing this love for sciences, including my formers advisors Dr. Carlos del Pino and Dr. Luis Parras who believe in the idea of me pursuing a PhD. Also thanks to Dr. Francisco Marques who very kindly took his time to help me understanding some details about my research.

Thanks to Dr. Javier Burguete of Navarra University (Spain) for inviting me to collaborate with his team one and half months. During that time I had the great experience of helping with the creation of a preliminary set up which would reproduce the counter-rotating case of the split geometry. I could learn about the difficulties of creating an experimental device while working with great people as his student Jesus Rodriguez.

Last but not least, I want to thank my family and friends for providing me an exceptional emotional support in the difficult moments and sharing with me the marvelous ones feeling them very close even when sometimes we have thousands of kilometers of distance.

This dissertation would be impossible without the received funding. ASU TA support and ASU Summer Block Grant. NSF grants 'Effects of interfacial viscosities on flow of lung surfactants', 'Catastrophic transition to turbulence in rotation-dominated flows'. NASA grant 'Amyloid fibril formation in microgravity: Distinguishing interfacial and flow effects The 2016-2017 Graduate Education Dissertation Fellowship which allowed me to completely devote my last year to finish writing my dissertation. The funding for my collaboration with Navarra University was provided by the Spanish Government Research Project 'Complejidad en Fluidos' contract FIS2014-54101-P.

TABLE OF CONTENTS

Page

LIST OF TABLES ix

LIST OF FIGURES x

CHAPTER

1 INTRODUCTION 1

1.1 Thesis Plan 5

2 INSTABILITIES OF THE SIDEWALL BOUNDARY LAYER IN A RAPIDLY ROTATING SPLIT CYLINDER 6

2.1 Abstract 6

2.2 Introduction 6

2.3 Governing Equations and Numerical Methods 8

2.4 Basic State 11

2.5 Axisymmetric Instabilities of the Sidewall Layer 19

2.6 Discussion and Conclusions 26

3 INSTABILITIES AND INERTIAL WAVES IN A RAPIDLY ROTATING SPLIT-CYLINDER FLOW 29

3.1 Abstract 29

3.2 Introduction 30

3.3 Governing Equations and Numerical Methods 33

3.4 Results 35

3.4.1 Basic State 35

3.4.2 Overview of the Instabilities 36

3.4.3 Low Azimuthal Wavenumber Rotating Waves 37

3.4.4 High Azimuthal Wavenumber Rotating Waves 47

3.4.5 Quasiperiodic Mixed-modes 50

CHAPTER Page

3.5 Discussion and Conclusions 57
4 THREE-DIMENSIONAL INSTABILITIES AND INERTIAL WAVES IN A RAPIDLY ROTATING SPLIT-CYLINDER FLOW 60
4.1 Abstract 60
4.2 Introduction 61
4.3 Governing Equations and Numerical Methods 63
4.4 Results 67
4.4.1 Basic State BS 69
4.4.2 Circle-pitchfork Bifurcations to Steady $\mathcal{H}$-symmetric States Sm 70
4.4.3 The 2:3 Mode Interaction 74
4.4.4 Parameter Sweep in Re with $\Gamma = 1.45$ 76
4.4.5 Rotating Wave RW from a Drift-pitchfork Bifurcation 78
4.4.6 Direction-reversing Wave DRW from a Hopf Bifurcation 79
4.4.7 Pulse Waves, PWs 82
4.4.8 Symmetry-breaking to PWa 86
4.4.9 Saddle-Node-on-an-Invariant-Circle Bifurcation Destroying PWa 89
4.4.10 Behavior over a Broader Range of Parameter Space 90
4.5 Discussion and Conclusions 97
5 PRELIMINARY EXPERIMENTAL COUNTER-ROTATING SPLIT CYLINDER 101
5.1 Experimental Setup 101
5.2 Measurements 104

CHAPTER Page

6 MODULATED DIFFERENTIALLY RAPIDLY ROTATING SPLIT CYLINDER FLOW . . . 113
6.1 Abstract . . . 113
6.2 Introduction . . . 114
6.3 Governing Equations and Numerical Methods . . . 116
6.4 Results . . . 119
6.4.1 Response with $\phi = \pi$ . . . 119
6.4.2 Nonlinear Waves Beams, Inviscid Kelvin Modes and Retracing Rays. . . . 124
6.4.3 Influence of the Phase Difference . . . 129
6.5 Discussion and Conclusion . . . 135
7 CONCLUSION AND FUTURE WORK . . . 138
7.1 Future Work . . . 139
REFERENCES . . . 141
APPENDIX
A CO-AUTHOR PERMISSIONS . . . 148

LIST OF TABLES

Table Page

3.1 Frequencies in the Stationary and Rotating Frames of Reference and Angles of the Inertial Wave Beam Cones for Different Stable RW States and the Unstable LC, All at $Re = 10^4$ and $Ro = 0.29$. 42

4.1 Summary of the Different States and Their Symmetries. Note that α, γ and β Are Arbitrary Unless Otherwise Indicated. 67

6.1 Frequencies ω Associated with Retracing Rays R_{nk} and Kelvin Modes K_{nk}, for $n \in [1, 5]$ and $k \in [1, 5]$, and γ as indicated. 126

LIST OF FIGURES

Figure Page

2.1 Schematic of the Flow System. The Inset Shows Azimuthal Vorticity Contours of an Axisymmetric Time-periodic State at $Re = 10^5$, $Ro = 0.110$ and $\gamma = 1$. 9

2.2 Profiles of the Regularized Sidewall Boundary Condition for the Azimuthal Velocity, $v(z) = 1 + Ro \tanh(\epsilon z)$, with $Ro = 0.26$ and ϵ as Indicated. The $\epsilon = 50$ Case Shows Open Symbols at the Chebyshev Collocation Points Corresponding to $n_z = 100$. 11

2.3 Contours of the Azimuthal Vorticity η of the Basic State at $Re = 10^4$, $Ro = 0.26$, $\gamma = 1$ and Two Values of ϵ, Both Computed with $n_r = n_z = 100$. 12

2.4 Radial Profiles of w Near the Sidewall at Mid-hieght $z = 0$ Determined From DNS at $Re = 10^5$, $Ro = 10^{-5}$ and $\gamma = 1$, Compared to the Boundary Layer Theory (BLT) of van Heijst [96], Scaled so that the Extremum Nearest the Wall Matches. 13

2.5 Scaled Sidewall Boundary Layer Thickness, $\delta/Re^{-1/3}$, Along the Length of the Cylinder; (a) Nonlinear Numerical Results (DNS) for $Re = 10^5$, $Ro = 10^{-5}$ and $\gamma = 1$, Compared to the Boundary Layer Theory (BLT) of van Heijst [96], (b) Numerical Results for $Ro = 10^{-5}$, $\gamma = 1$, and Re as Indicated, and (c) Numerical Results for $Re = 10^5$, $\gamma = 1$ and Ro as Indicated. 14

2.6 Streamlines and Contours of v Close to the Sidewall of the Cylinder ($0.8 \le r \le 1.0$), for $Re = 10^5$, $\gamma = 1$ and Ro as Indicated. 16

Figure Page

2.7 Streamlines and Contours of v Zoomed Into the Split in the Sidewall ($0.95 \leq r \leq 1.0$ and $-0.2 \leq z \leq 0.2$), for Same Cases as Shown in Fig. 2.6. 17

2.8 Variation of (a) $\sqrt{||\alpha||}$ and (b) $||w||$, with Ro. 18

2.9 Vertical Velocity Profiles Close to the Sidewall of the Cylinder for $Re = 10^5$, $\gamma = 1$ and Ro as Indicated. 19

2.10 Regime Diagram in (Ro, γ)-space, Showing the Various Axisymmetric States Found Near the Double-Hopf Bifurcation for $Re = 10^5$. 20

2.11 Snapshots of η (Left) and the Corresponding Power Spectral Densities of Ek (Right), at $Re = 10^5$ for (a) LC1 at $Ro = 0.11$, $\gamma = 0.5$, (b) LC2 at $Ro = 0.11$, $\gamma = 1$, (c) QP at $Ro = 0.105$, $\gamma = 0.6875$, (d) QP2 at $Ro = 0.12$, $\gamma = 1$, and (e) QP4 at $Ro = 0.11$, $\gamma = 1.0625$. 22

2.12 Snapshots of η at $Re = 10^5$, $\gamma = 0.5$ and Ro as Indicated. 24

2.13 Snapshots of η at $Re = 10^5$, $\gamma = 0.6875$ and Ro as Indicated. 25

3.1 Schematic of the Flow System. The Inset Shows Contour of the Azimuthal Vorticity η of the Basic State at $Re = 1.2 \times 10^4$, $Ro = 0.23$ and $\gamma = 1$. 33

3.2 Regime Diagram Presenting an Overview of the Solutions Obtained. . . . 36

3.3 Variations of the Modal Kinetic Energies E_m of the Various Rotating Waves RW_m ($m \in [1, 4]$) Versus Ro for $Re = 10^4$. The Filled Symbols Correspond to Stable States and Open Symbols to Unstable States (Computed in the Corresponding Subspaces). Panel (b) Is a Zoomed-in Version of Panel (a). 37

Figure Page

3.4 Contours of (a) η, (b) $\eta - \eta_0$ in the Meridional Plane $\theta = 0$, and (c) $\eta - \eta_0$ in the Plane $z = -0.4$, for the Rotating Waves RW_m, $m \in [1, 4]$, at $Re = 10^4$, $Ro = 0.29$. 40

3.5 Isosurfaces of $w - w_0$, at Levels ± 0.001, of (a) RW_1, (b) RW_2, (c) RW_3, and (d) RW_4 at $Re = 10^4$ and $Ro = 0.29$. 41

3.6 Contours of (a) η, (b) $\langle\eta\rangle$ and (c) $\eta - \langle\eta\rangle$ in a Vertical Plane for the Unstable LC Solution at $Re = 10^4$, $Ro = 0.29$. 42

3.7 Contours of $\eta - \langle\eta\rangle \in [-1, 1]$ for the Unstable LC and $\eta - \eta_0$ for the Stable RW_1, RW_2, RW_3 and RW_4 in a Meridional Plane $\theta = 0$ at $Re = 10^4$and $Ro = 0.29$; Snap-shots at Six Equally Spaced Phases Over Their Respective Periods Are Shown 43

3.8 Variation of Principle Modal Kinetic Energies for Various States with Increasing Re for (a) $Ro = 0.28$ and (b) $Ro = 0.27$; E_h Corresponds to the Modal Kinetic Energy for the High Azimuthal Wavenumber Component of the Various QP States. 46

3.9 Variation of Principle Modal Kinetic Energies for Various States with Increasing Re for $Ro = 0.20$; E_h Corresponds to the Modal Kinetic Energy for the High Azimuthal Wavenumber Component of the Various States. 47

3.10 Contours of (a) η and (b) $\eta - \eta_0$ at $\theta = 0$, (c) $\eta - \eta_0$ at $z = -0.4$, and (d) Isosurfaces of $w - w_0$, at Levels and ± 0.001, for RW_{41} at $Re = 1.55 \times 10^4$ and $Ro = 0.20$. 49

Figure Page

3.11 Contours of (a) η and (b,c) $\eta-\eta_0$ at $\theta=0$, (c) $\eta-\eta_0$ at $z=-0.4$, and (d) Isosurfaces of $w-w_0$, at Levels and ± 0.001, for $\mathrm{QP}_{0,36}$ at $Re=1.35\times10^4$, $Ro=0.23$. 51

3.12 Contours of (a) η, (b,c) $\eta-\eta_0$, and Isosurfaces of (d) $w-w_0$, (e) w_2 and (f) w_{39} for $\mathrm{QP}_{2,39}$ at $Re=1.50\times10^4$ and $Ro=0.28$. 53

3.13 Azimuthal (E_m Mean Modal Kinetic Energies) and Temporal (PSD of w at $(r,\theta,z)=(0.98,0,-0.4)$) Spectra for (a,c) $\mathrm{QP}_{1,31}$ at $Re=1.40\times10^4$, (b,d) HNL at $Re=1.55\times10^4$, Both Cases at $Ro=0.27$ 54

3.14 Contours of (a) η and (b,c) $\eta-\eta_0$ at $\theta=0$, (c) $\eta-\eta_0$ at $z=-0.4$, and (d) Isosurfaces of $w-w_0$ at Levels and ± 0.001, for HNL at $Re=1.55\times10^4$, $Ro=0.27$. 56

4.1 Schematic of the Flow System. The Inset Shows Contours of rv (Vortex Lines) for a Basic State BS at $(\Gamma,Re)=(1,115)$. 63

4.2 (a) Axial (z) Profiles of the Three Velocity Components at $r=0.5$ and $\theta=0$ of S2 at $(\Gamma,Re)=(1.45,123)$ Computed with $n_r=40$, $n_\theta=64$ and Either $n_z=120$ (Thick Black Curves) or $n_z=160$ (Thin Colored Curves), and (b) the Absolute Differences Between the Three Velocity Component Computed with the Two Resolutions 65

4.3 Contours in a Meridional Plane ($\theta=0$, $r\times z\in[0,1]\times[-0.5\Gamma,0.5\Gamma]$) of (a) ψ (Streamlines), (b) rv (Vortex Lines), (c) v/r (Angular Velocity), and (d) Isosurfaces of w of BS at $(\Gamma,Re)=(1.45,115)$ for the Split Sidewall Case (a,b,c,d) and the Stationary Sidewall Case (e,f,g,h). . . . 68

4.4 Loci in (Γ, Re) Parameter Space of Circle-pitchfork Bifurcations Where BS Loses Stability to $\mathcal{H}$-symmetric Steady States Sm, with Azimuthal Wavenumber m as Indicated, Upon Crossing from low Values of Re and Γ. 70

4.5 Isosurfaces of w (First Row), $w - w_0$ (Second Row) and Contours of w at $z = 0$ (Third Row), for S2 at $(\Gamma, Re) = (1.45, 123)$, S3 at $(\Gamma, Re) = (1.45, 135)$, S4 at $(\Gamma, Re) = (0.80, 225)$, S5 at $(\Gamma, Re) = (0.60, 250)$, and S6 at $(\Gamma, Re) = (0.50, 300)$. 71

4.6 Bifurcation Curves Near the 2:3 Mode Interaction, Together with Schematic Phase Portraits in the Regions Near the Codim-2 Point at $(\Gamma, Re) = (1.3, 129.5)$; ξ_2 and ξ_3 are the $m = 2$ and $m = 3$ Subspaces. 74

4.7 Variation of Modal Kinetic Energies with Re for Various States as Indicated, with $\Gamma = 1.45$. The Unstable States (Open Symbols) Were Computed in Their Respective Subspaces. 76

4.8 Isosurfaces of (a) w, (b) $w - w_0$, and (c) Contours of w at $z = 0$, for RW at $(\Gamma, Re) = (1.45, 142)$. See the Online Movie for an Animation of $w - w_0$. 77

4.9 Drift Period of RW, T_w, Versus Re, Together with a Curve Fit $T_w = 0.117 + 4.018/\sqrt{Re - 137.872}$. The Unstable RW (Open Symbols) Were Computed in ξ_2. 78

4.10 Snapshots Over One T_E Period Relative to an Arbitrary Reference Time of w-isosurfaces, $w - w_0$-isosurfaces, and w Contours at $z = 0$ for DRW at $(\Gamma, Re) = (1.45, 165)$ Computed in ξ_4. 80

Figure Page

4.11 Time Series of E_4 (Solid Line) and $w(0.98, 0, -0.4\Gamma)$ (Dashed Line) of DRW at $(\Gamma, Re) = (1.45, 165)$, Computed in ξ_4. 80

4.12 (a) Peak-to-peak Amplitude and (b) Period of E_4 for DRW at $\Gamma = 1.45$, Computed in ξ_4. The Stable S4 Are Indicated as (Blue) Diamonds in Order to Show the Region of Hysteresis Between S4 and DRW. 81

4.13 Variation with Re of (a) the Time-averaged Modal Energy $\langle E_2 \rangle$ and (b) the Period T_E of RW and PWs, for $\Gamma = 1.45$, Computed in the Full Space ξ_1. 82

4.14 Time Series of (a) Modal Kinetic Energies E_2 and E_4, and (b) $w(0.98, 0, -0.4\Gamma)$ for PWs at $(\Gamma, Re) = (1.45, 153.5)$. The (Green) Diamonds Correspond to the Numbered Diamonds in Figure 4.16. 83

4.15 Snapshots over One T_E Period Relative to an Arbitrary Reference time of w-isosurfaces, $w - w_0$-isosurfaces, and w Contours at $z = 0$ for PWs at $(\Gamma, Re) = (1.45, 153.5)$. 83

4.16 Phase Portraits, (a) Using $w(0.98, 0, 0, t)$ and $w(0.98, 0, 0.2\Gamma, t)$ and (b) Using E_2 and E_4, for PWs at $(\Gamma, Re) = (1.45, 153.5)$ 85

4.17 Snapshots over One T_E Period Relative to an Arbitrary Reference Time of w-isosurfaces, $w - w_0$-isosurfaces, and w Contours at $z = 0$ for PWa at $(\Gamma, Re) = (1.45, 160)$ Computed in ξ_2. 86

4.18 Phase Portraits, (a) Using $w(0.98, 0, 0, t)$ and $w(0.98, 0, 0.2\Gamma, t)$, and (b) Using E_2 and E_4, for PWa at $(\Gamma, Re) = (1.45, 160)$. 87

4.19 Time Series of (a) Modal Kinetic Energies E_1, E_2, E_3 and E_4, and (b) $w(0.98, 0, -0.4\Gamma)$ for PWa at $(\Gamma, Re) = (1.45, 160)$. The Diamonds Correspond to the Numbered Diamonds in Figure 4.18. 87

4.20 Variation with Re of (a) the Time-averaged Modal Energy $\langle E_2 \rangle$ and (b) the Period T_E of RW, PWs, PWa, and S2 for $\Gamma = 1.45$, Computed in the Full Space ξ_1. Near $Re = 206$, the Period of PWa Has the Fit $T_E = 0.285 + 0.831/\sqrt{206.312 - Re}$. 88

4.21 Phase Portrait in (E_2, E_4) for PWa at $\Gamma = 1.45$ and Re as Indicated. There Are 25 Equispaced-in-time Circular Markers over T_E, Used to Illustrate the Slow-Fast Nonlinear Oscillation. In (c), the (Green) Diamond Corresponds to the Steady S2 at $Re = 206.32$. 89

4.22 Isosurfaces of (a) w, (b) $w - w_0$, and (c) Contours of w at $z = 0$, for S2 at $(\Gamma, Re) = (1.45, 206.32)$. 90

4.23 Loci of Stable States in (Γ, Re), Found by Using BS at $Re = 100$ at Each Γ as the Initial Condition for Simulations for All Re at that Γ. No Attempt Was Made to Show Loci of Multiple Stable States at the Same Point in Parameter Space that Were Found Using Other Initial Conditions. 91

4.24 Snapshots over One T_E Period Relative to an Arbitrary Reference Time $w - w_0$-isosurfaces and w Contours at $z = 0$ for PWa at $(\Gamma, Re) = (1.80, 175)$. 92

4.25 (a) Time Series of E_m and (b) Phase Portrait Using E_2 and E_4 for PWa at $(\Gamma, Re) = (1.80, 175)$. 92

4.26 Time Series of (a) Modal Kinetic Energies E_2 and E_4 and (b) $w(0.98, 0, -0.4\Gamma)$ for PWo at $(\Gamma, Re) = (1.5, 210)$. 93

4.27 Snapshots of $w - w_0$ Isosurfaces and w Contours at $z = 0$ over $2T_E$ Relative to an Arbitrary Reference Time for PWo at $(\Gamma, Re) = (1.50, 210)$. 94

4.28 Time Series of (a) Modal Kinetic Energies E_1, E_2, E_3, and E_4, and (b) $w(0.98, 0, -0.4\Gamma)$ for LC at $(\Gamma, Re) = (1.9, 275)$. 95

4.29 Snapshots of $w - w_0$ Isosurfaces and w Contours at $z = 0$ over $2T_E$ Relative to an Arbitrary Reference Time for LC at $(\Gamma, Re) = (1.90, 275)$. 96

4.30 Variation of the Symmetry Measure S, Using $\mathcal{H}_0$, with the Rotation Angle ϕ for PWo at $(\Gamma, Re) = (1.50, 210)$ and LC at $(\Gamma, Re) = (1.90, 275)$. 96

5.1 (a) Schematic of the Experimental Device and (b) Experimental Cylinder. 101

5.2 Signal Generator. 103

5.3 (a) Picture of the Rheometer and (b) Measurement of the Glycerine Viscosity Using a Rheometer. 104

5.4 (a) Picture of the Laser Generator and (b) Picture of the Experimental Device with the Laser on. 105

5.5 (a) Picture of Cylinder Filled with Particles and (b) Picture of an Even Distribution of the Particles. 106

5.6 Scheme of the Laser Going Through the Different Surfaces. 107

5.7 Velocity Contour Measured in a Meridional Plane for a Case with the Cylinder Containing Water for $\gamma = 1.2$ and $Re = 3808$. 108

5.8 Snapshot of the Pool with Light up with a Laser Plane. 109

5.9 Snapshot of a Light up of a Rectangular and Circular Sections Section at $Re = 136.56$. 109

5.10 Snapshot of a Light up of a Rectangular and Circular Sections for at $Re = 236.71$. 110

5.11 Stream Functions Calculated Using the Experimental Visualizations. . . 111

Figure Page

6.1 Schematic of the Flow System. The Inset Shows Azimuthal Vorticity η for $Re = 10^6$, $\gamma = 1$, $\alpha = 10^{-4}$, $\omega = 0.88$ and $\phi = \pi$ 116

6.2 Azimuthal Vorticity Contours in the Meridional Plane $(r, z) \in [0, 1] \times [-\gamma/2, \gamma/2]$, with $\phi = \pi$ at Various ω as Indicated (the Corresponding Beam Angle β According to the Dispersion Relation is Also Indicated). 120

6.3 Variation of η_{f} with Forcing Frequency ω for $\gamma = 1$ and $\phi = \pi$. 121

6.4 Endwall Boundary Layer Thickness δ Obtained from Simulations (DNS) and Estimated Using Wang's Theory [101] with $c = 8.14$. 122

6.5 Variation of η_{b} with ω, for $\gamma = 1$ and $\phi = \pi$, with the Excluded Portions of the Boundary Layers Indicated. 123

6.6 Retracing Rays (a) R_{41} at $\omega = 1.94$, and (c) R_{45} at $\omega = 1.25$ and, (b, d) η Contours at the Corresponding Frequencies with $\phi = \pi$. 124

6.7 Variation with Forcing Frequency of the Maximum Value of Azimuthal Vorticity over the Forcing Period in the Bulk Flow (Excluding the Endwall and Sidewall Boundary Layers to the Level 1.16δ) for $\phi = \pi$ and γ as Indicated. The Red Squares are the Responses at Frequencies Corresponding to Low-order Retracing Rays and the Black Triangles are the Responses at Frequencies Corresponding to Low-order Kelvin Mode Frequencies. 127

6.8 Comparison Between the Kelvin Eigenmodes (First Row) and Azimuthal Vorticity Contours at the Resonant Frequency, for $\phi = \pi$ and γ as Indicated. 128

6.9 Variation of η_b with ω, for $\gamma = 1$ and ϕ as Indicated. The Black Triangles are the Responses at Frequencies Corresponding to K_{1k} with $k \in [1, 4]$ and the Green Circles Corresponding to K_{2k} with $k \in [1, 3]$. . . 130

6.10 Comparison Between the Kelvin Modes and Azimuthal Vorticity Contours at the Given Frequencies ω, Corresponding to Peaks in η_b, for $\gamma = 1$ and ϕ as Indicated. 131

6.11 Comparison Between the Kelvin Modes and Azimuthal Vorticity Contours at the Given Frequencies ω, Corresponding to Peaks in η_b, for $\gamma = 1$ and ϕ as Indicated. 132

6.12 Azimuthal Vorticity Contours for $\gamma = 1$ at ω and ϕ as Indicated. 133

Chapter 1

INTRODUCTION

The aim of this dissertation is to gain insight into the essential features of rotating flows in a split-cylinder geometry. Rotating geometries studies have a rich history encompassing theoretical, numerical and experimental research due to its fundamental and practical importance. Rotating flows influence ocean currents, produce hurricanes and tornadoes, and affect the climate. Furthermore, turbulent rotating fluids are quite counter intuitive and this is mainly due to their associated Coriolis force which gives rise to inertial waves. This dissertation involves the understanding of these waves that is vital since they influence how energy is transported in rapidly rotating flows. In addition, analogies exist between the behavior of inertial waves generated by Coriolis forces in rotating fluids, internal gravity waves generated by buoyancy forces in stratified fields and Alfén waves generated by Lorenz forces in magnetic fields (Davidson [17]).

Inertial waves have been studied for decades. However, the theory for three-dimensional rotating flows affected by instabilities and inertial waves is not complete, since the flow becomes very complicated from the effects associated with nonlinearity, curvature, and viscous boundary layers. A fist approach is to consider some simplified cases as the inviscid linear theory, where the viscous and nonlinear terms are neglected. For a review of the inviscid linear theory see Greenspan [24]. This theory predicts that inertial waves are only created if the perturbation frequency is less than twice the solid body rotation frequency. This phenomenon has been observed in different rotating flows in a multitude of geometries. It is important to form a complete understanding of inertial waves since they can be used to perturb the flow even in the asymptotic

regime where the Coriolis force dominates viscous forces.

This importance motivates the vast presence in literature of studies involving differential rotating cylinders. A significant part them was focused on the flow contained in a rotating cylinder with only one lid differentially rotating broad range. Hart and Kittelman [27] experimentally found a number of instabilities in the sidewall Stewartson layer in the form of rotating rolls. Additionally, Lopez and Marques [54] investigated numerically the three-dimensional instabilities and inertial waves of the same geometry finding agreement with the previous experimental results. This geometry is studied not only due to its fundamental importance but also because this geometry can be used as an idealized model for ocean circulations. Specifically, studies with aspect ratio order one and appropriate range of Reynolds number can be employed typically to represent the convection cells of the ocean of the representative mesoscale and submesoescale eddies. A good example of a recent study focusing on this application was realized by Pratt *et al.* [81] who obtained interesting results for steady solutions even though the model is only a starting point to represent the behavior of the ocean and some other important physical properties, such as stratification or turbulence of the flow, should be included in the model in future studies.

These studies motivate us to explore a differentially rotating split geometry with both parts of the cylinder co-rotating with differential rotation. The first part of this dissertation target this point and include a review of the few previous studies in this geometry.

The study of the flow contained between counter-rotating disks has also a practical importance and it has been extensively studied in literature. Specifically, there exist some studies focused on counter-rotating lids in completely filled cylinders. However, the influence of a split cylinder with both halves of a cylinder rotating with the same speed as the endwalls has not been studied before to our knowledge for the case of a

finite cylinder. Understanding this geometry and comparing it with counter-rotating disks is the goal of the second part of this dissertation. Before describing in detail the background of these kinds of problems we want to remark that the behavior of this configuration is completely different from the setup reproduced the first part of this project. For this geometry, the instabilities are produced by the shear layer formed by the two regions of opposite azimuthal velocities.

The studies focused on counter-rotating lids in completely filled cylinders are useful as comparison and background for this section. The first decade of the new millennium was very productive in the study of these geometries. Lopez *et al.* [49] reproduced an experimental setup for a fixed aspect ratio and developed full three-dimensional numerical simulations finding good agreement. Gauthier *et al.* [21] developed a study for a fixed aspect ratio $\gamma = 0.05$ expanded later by Moisy *et al.* [67] for a wider range of small aspect ratios finding both negative spirals. Nore and her group presented a variety of work in this field both from the experimental and numerical point of view. They started with Nore *et al.* [75] where they focused on the interaction of 1:2 mode. Followed by Nore *et al.* [74] where their focus was the primary instability threshold for a range of aspect ratios. This range was extended even further in the study Nore *et al.* [76] where they reported the preference of the first instability to break (or not) the axisymmetry of the flow depending on the aspect ratio. This work is complementary to Pecheux and Foucault [79] which encompasses both the experimental a two-dimensional numerical results. A different group reported in the study by Hewitt and Hazel [28] focused on the symmetry breaking in the mid-plane.

The understanding of the symmetries and their influence in the bifurcations is one of our main goals for the counter-rotating case. To achieve it, a variety of three-dimensional numerical simulations were conducted for a range of aspect ratios and velocities of both halves of the cylinder. We also performed a study on the kind of

bifurcations and the states found including a diversity of stationary waves, rotating waves, and time dependent states.

Another branch of studies focused in geometries with imposed oscillatory boundary conditions in relatively simple geometries. These devices are frequently used to design simple experiments that are able to produce inertial waves which penetrate into the bulk of the cylinder. This is also the focus of the last part of this dissertation where we reproduce numerical experiments in a split cylinder with both halves differentially rotating and periodically oscillating. Therefore, there exist two simultaneous effects, namely the background rotation of the cylinder and differential oscillation of both halves. There is a lack of literature in the split cylinder geometry with oscillatory boundary conditions. However, some previous studies in similar geometries can be used to get an idea about the flow behavior and the difficulties to fully understand it. There are two main branches of this kind of studies based on spherical and cylindrical geometries including some in which temperature difference is imposed producing convection. In this introduction, we will focus on the problems without the temperature influence since our study does not present this effect. The first branch based in spherical geometries are mainly motivated by planetary applications. They primarily started with the experimental and theoretical study by Albridge and Toomre [2] and are still very present in literature nowadays including also numerical studies. This branch is also amplified by the inclusion of ellipsoidal geometries. Some of the recent references in spherical geometries can be found in Busse [9], Le Bars *et al.* [43], Noir *et al.* [72]. The study of geometries as cubes Boisson *et al.* [7] or a frustum and a cylinder Klein *et al.* [34] is also active in this decade. A deep review of the previous studies on cylindrical geometries is presented in the introduction of chapter 6 of this dissertation.

1.1 Thesis Plan

This dissertation focus on the study of a split-cylinder geometry that makes numerical simulations and theoretical models tractable. The fluid contained in a rotating split cylinder of radius a and height h is numerically investigated mainly via spectral methods. Three different types of boundary conditions were imposed, creating a multitude of interesting behaviors in the flow including instabilities and inertial waves. The spectral solver used is based on the method described in Mercader *et al.* [66]. This method has been used extensively in a wide variety of enclosed cylinder flows. There exist some small details of its implementation varying depending on the boundary conditions imposed for each problem and they are explained in the respective chapter.

The remaining of this monograph is organized as follows. Chapter 2 studies the geometry with both halves of the cylinder co-rotating with a high background speed and a small differential speed numerically investigated for the axisymmetric case. This work was published in Gutierrez-Castillo and Lopez [25]. Chapter 3 expands that paper with a three-dimensional study of the same geometry. This work was published in Lopez and Gutierrez-Castillo [48].

Chapter 4 investigates the case in which both halves of the cylinder are counter-rotating. This work was published in Gutierrez-Castillo and Lopez [26]. Chapter 5 shows some preliminary results obtained in an experimental set up obtained while collaborating with Navarra University lab.

Chapter 6 describes the flow obtained after imposing a periodic forcing to the slit-cylinder using axisymmetric simulations. Conclusions and future directions are presented in chapter 7.

Chapter 2

INSTABILITIES OF THE SIDEWALL BOUNDARY LAYER IN A RAPIDLY ROTATING SPLIT CYLINDER

2.1 Abstract

The instabilities of the sidewall boundary layer in a rapidly rotating split cylinder are studied numerically. Axisymmetric results are studied extensively where a variety of different states are found. In the basic state, the interior flow is in solid-body rotation with the mean rotation rate of the two cylinder halves. The sidewall boundary layer of the basic state is compared with theoretical results. For sufficiently fast mean rotation and large enough differential rotation between the two halves, instabilities in the boundary layer appear. These instabilities result in periodic and quasi-periodic states in different parameter regimes. The instabilities are localized in the boundary layer, but they may transport shear into the interior if their associated frequencies are less than twice the mean rotation frequency, and then only in the form of inertial wave beams along directions determined by their frequencies.

2.2 Introduction

The structure of the sidewall boundary layer in a rapidly rotating cylinder subjected to some differential rotation has attracted much attention because of both its practical and fundamental importance. Stewartson [92] first showed that when the sidewall rotates at a rate slightly faster than the two endwalls, the sidewall boundary layer has a sandwich structure consisting of an inner layer whose thickness scales as $Re^{-1/3}$ (where Re is the rotation Reynolds number based on the mean angular velocity of

the cylinder, its radius and the kinematic viscosity of the fluid) and an outer layer with a thickness that scales as $Re^{-1/4}$. The $Re^{-1/4}$ layer is where the perturbation to the azimuthal velocity is adjusted and the inner $Re^{-1/3}$ layer is needed to adjust the secondary meridional flow. The boundary layers on the endwalls are of Ekman type, and they scale as $Re^{-1/2}$.

Hocking [30] considered another differentially rotating cylinder flow consisting of a split cylinder with one half rotating slightly faster than the other. His analysis considered the case of an infinitely long cylinder in which case the meridional flow in the sidewall layer due to the flows being pumped out of the Ekman layers at the ends was neglected. The finite split cylinder problem, in which endwall effects are present, was later addressed by van Heijst [96] using boundary layer analysis. His results showed that the quasi-geostrophic (almost independent of the axial direction) $Re^{-1/4}$ layer is unable to provide the matching between the azimuthal interior velocity and the discontinuous velocity of the sidewall, that the non-geostrophic $Re^{-1/3}$ layer is needed to match the discontinuous sidewall velocity but is unable to do so on its own, but that the combination of the two layers does provide the required matching.

The theoretical boundary layer analysis proceeds in the limit of very fast rotation (large Re) and very small differential rotation. The small differential rotation allows one to neglect the inertia terms and leads to linear governing equations, and the large Re leads to boundary layers whose thickness is much smaller than the cylinder radius, allowing one to neglect curvature terms in the sidewall boundary layer analysis. Of course, this raises the question as to what happens as the differential rotation is increased; how is the boundary layer structure altered given that the increased meridional flow driven by the Ekman layers may lead to a fundamental change in the boundary layer structure (e.g., see Redekopp [84]), and at some finite strength of the differential rotation the nonlinear terms will become non-negligible and instabilities

can be expected to ensue. Hart and Kittelman [27] provide some insights from flow visualization experiments in the case where the rapidly rotating cylinder has the top endwall rotating faster than the rest of the cylinder. Lopez [46] simulated this and other related flows solving the axisymmetric Navier–Stokes equations, and Lopez and Marques [54] investigated the three-dimensional instabilities of that flow. The boundary layer analysis van Heijst [96] shows that the relative roles of the $Re^{-1/4}$ and $Re^{-1/3}$ layers are very different when the split in the cylinder is at mid-height compared to when it is at one of the corners where an endwall meets the sidewall. This difference raises the question as to how does the nonlinear behavior differ when the split is at half-height.

For these rapidly rotating split cylinder problems, in the absence of instabilities, the interior flow is in solid-body rotation with the mean rotation rate of the two cylinder halves. For fast enough mean rotation, disturbances from instabilities can only penetrate into the interior if their frequencies are less than twice the mean rotation frequency, and then only in the form of inertial wave beams along directions determined by their frequencies. In the inviscid limit, this is governed by the inertial wave dispersion relation Greenspan [24], but for large but finite Re and finite differential rotation, viscous and nonlinear effects come into play, as well as mean-flow deformations leading to bulk flows that have non-constant angular speed. Furthermore, how these inertial wave beams feed back on the boundary layer and corner instabilities is not obvious, and we also try to address this.

2.3 Governing Equations and Numerical Methods

Consider the flow in a circular cylinder of radius a and height h, completely filled with a fluid of kinematic viscosity ν. The cylinder is split in two, the top half rotates with angular speed $\Omega + \omega$ and the bottom half with angular speed $\Omega - \omega$. Figure 3.1

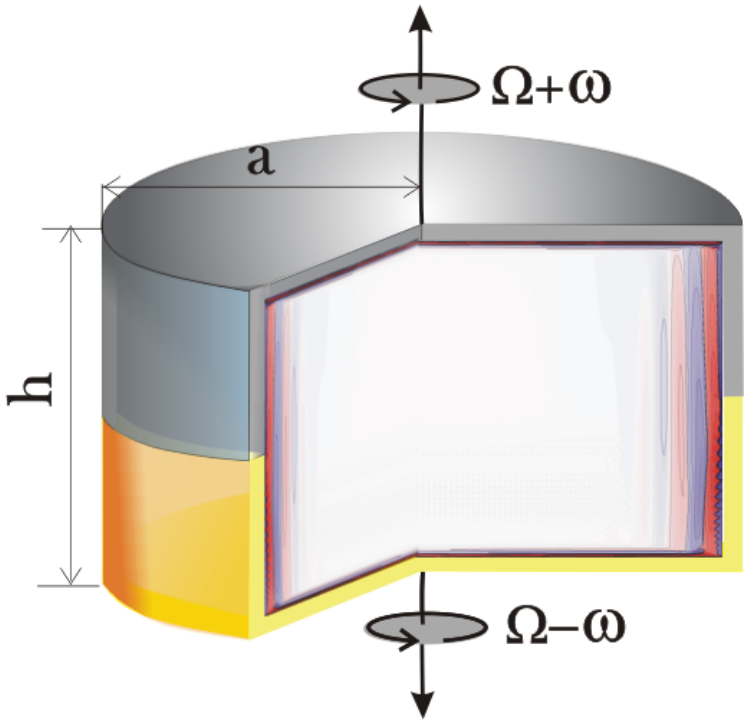


Figure 2.1: Schematic of the flow system. The inset shows azimuthal vorticity contours of an axisymmetric time-periodic state at $Re = 10^5$, $Ro = 0.110$ and $\gamma = 1$.

shows a schematic of the flow.

The Navier–Stokes equations, non-dimensionalized using a as the length scale and $1/\Omega$ as the time scale, are

$$(\partial_t + \boldsymbol{u}\cdot\nabla)\boldsymbol{u} = -\nabla p + 1/Re\nabla^2\boldsymbol{u}\,, \qquad \nabla\cdot\boldsymbol{u} = 0\,, \tag{2.1}$$

where $\boldsymbol{u} = (u, v, w)$ is the velocity field in polar coordinates $(r, \theta, z) \in [0, 1] \times [0, 2\pi] \times [-\gamma/2, \gamma/2]$, and p is the kinematic pressure. There are three governing parameters:

$$\begin{aligned} &\text{Reynolds number} && Re = \Omega a^2/\nu, \\ &\text{Rossby number} && Ro = \omega/\Omega, \\ &\text{aspect ratio} && \gamma = a/h. \end{aligned} \tag{2.2}$$

The boundary conditions are no-slip:

$$\begin{aligned} z = 0.5\gamma : &\qquad (u,v,w) = (0, r(1+Ro), 0), \\ z = -0.5\gamma : &\qquad (u,v,w) = (0, r(1-Ro), 0), \\ r = 1, z \in (0, 0.5\gamma) : &\qquad (u,v,w) = (0, 1+Ro, 0), \\ r = 1, z \in (0, -0.5\gamma) : &\qquad (u,v,w) = (0, 1-Ro, 0). \end{aligned} \tag{2.3}$$

In this present study, we only consider axisymmetric flows. The governing equations (6.1) have been solved using a second-order time-splitting method, with space discretized via Chebyshev collocation in r and z:

$$\boldsymbol{u}(r,z,t) = \sum_{n=0}^{2n_r+1} \sum_{m=0}^{n_z} \hat{\boldsymbol{u}}_{mn}(t) \Xi_n(r) \Xi_m(z), \tag{2.4}$$

where Ξ_n is the n-th Chebyshev polynomial. The spectral solver is based on that described in Ref. Mercader *et al.* [66] and it has been used extensively in a wide variety of enclosed cylinder flows. In the present paper where we focus on flows with $Re = 10^5$, we have typically used $n_r = 100$ and $n_z = 100$ and $\delta t = 4 \times 10^{-4}$. This provides sufficient spacial resolution to have between 6 and 9 collocation points in the bottom and top boundary layers (the two are not symmetric due to the differential rotation Ro), and δt is small enough to capture the dynamics.

The jump discontinuity in the sidewall boundary condition for the azimuthal velocity is problematic when solving the system using a spectral method as it leads to Gibb's phenomenon. This issue can be remedied by regularizing the boundary condition by smoothing out the jump over a small distance, in essentially the same way as the corner discontinuity between a sidewall and a differentially rotating endwall is regularized Lopez and Shen [60]. Specifically, we replace the boundary condition for the azimuthal velocity with

$$v(r=1,z) = 1 + Ro \tanh(\epsilon z), \tag{2.5}$$

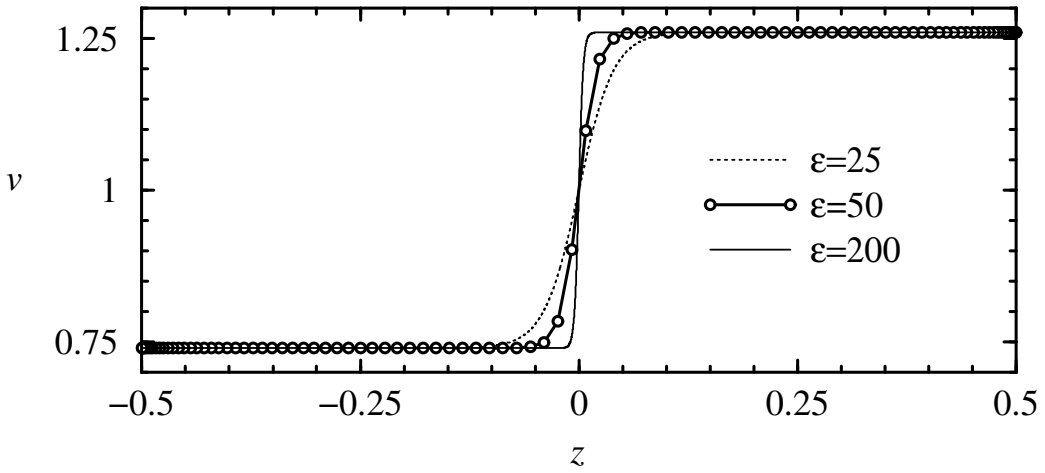


Figure 2.2: Profiles of the regularized sidewall boundary condition for the azimuthal velocity, $v(z) = 1 + Ro \tanh(\epsilon z)$, with $Ro = 0.26$ and ϵ as indicated. The $\epsilon = 50$ case shows open symbols at the Chebyshev collocation points corresponding to $n_z = 100$.

where ϵ governs the distance over which the jump is smoothed out. Figure 2.2 shows the azimuthal velocity profile, η, at the sidewall for $Ro = 0.26$ and various values of ϵ. In the $\epsilon = 50$ case, the open symbols are at the Chebyshev collocation points corresponding to $n_z = 100$. Figure 2.3 shows the azimuthal vorticity for $Re = 10^4$, $Ro = 0.26$, $\gamma = 1$ with $\epsilon = 50$ and $\epsilon = 200$. There is little difference in selecting $\epsilon > 50$, and for the rest of the results presented here, we fix $\epsilon = 50$.

2.4 Basic State

The interior flow of the basic state (BS) in a finite rotating cylinder split into two differentially rotating parts is essentially in solid-body rotation with approximately the mean rotation rate of the two cylinder halves. The top and bottom endwall boundary layers are Ekman like, and the only meridional flow in the interior is a weak axial flow from the slower (bottom) to the faster (top) rotating endwall. The interesting flow structure is associated with the sidewall boundary layer. Van Heijst [96] used

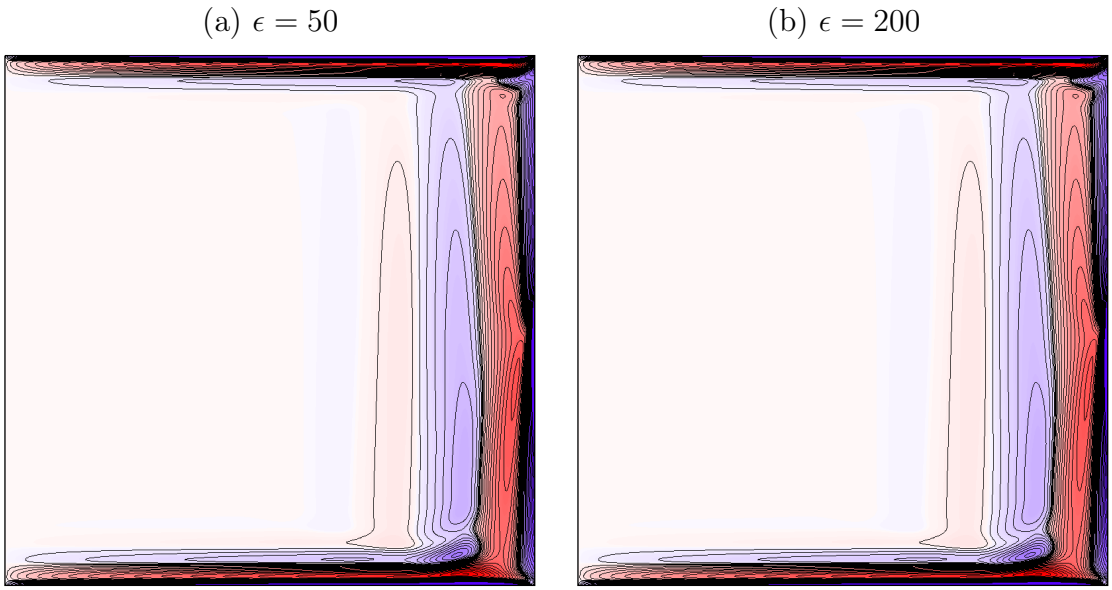


Figure 2.3: Contours of the azimuthal vorticity η of the basic state at $Re = 10^4$, $Ro = 0.26$, $\gamma = 1$ and two values of ϵ, both computed with $n_r = n_z = 100$. There are 20 positive (red) and 20 negative (blue) contours that are quadratically spaced in the range $\eta \in [-5, 5]$.

boundary layer analysis to show that the main effect of the two endwalls is the order $Re^{-1/2}$ transport that appears in the sidewall Stewartson layer. He described how the combination of the $Re^{-1/4}$ and $Re^{-1/3}$ boundary layers matches the boundary conditions. For the case we study here, with the discontinuity in the middle of the cylinder, only the zeroth order field of the $Re^{-1/3}$ appears and the $Re^{-1/4}$ layer is absent in the analysis. The boundary layer analysis results were obtained in the $Ro \to 0$ limit, and both curvature and inertia were neglected.

The boundary layer analysis is very useful in providing basic insight into the problem, but its validity is undetermined with regards to nonlinear effects and subsequent instabilities. In order to simulate cases where the boundary layer analysis is

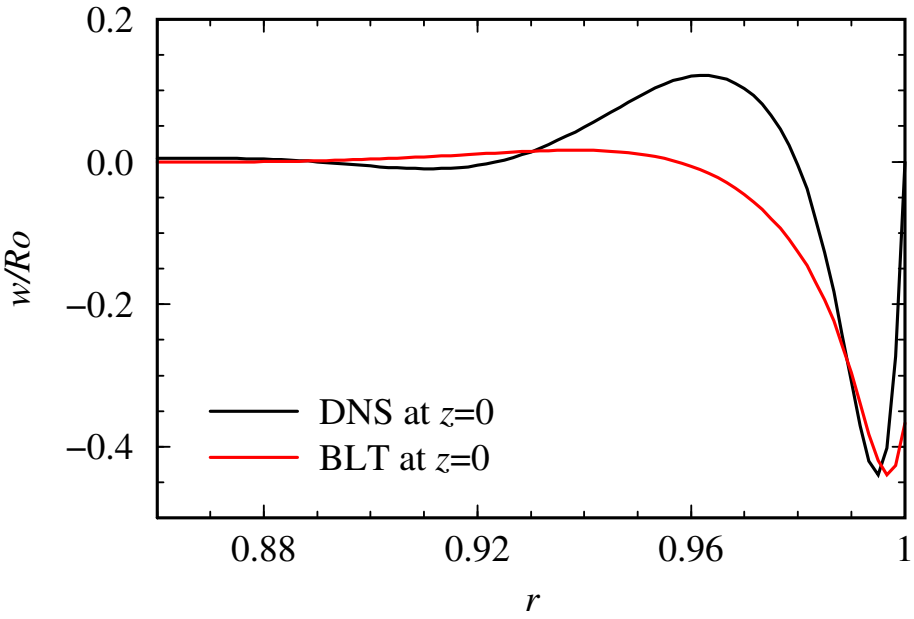


Figure 2.4: Radial profiles of w near the sidewall at mid-hieght $z = 0$ determined from DNS at $Re = 10^5$, $Ro = 10^{-5}$ and $\gamma = 1$, compared to the boundary layer theory (BLT) of van Heijst [96], scaled so that the extremum nearest the wall matches.

valid, we have used Re as large as 10^5 so that the effects of the curvature would be negligible (due to the thinness of the boundary layer) and Ro as small as 10^{-5} in order to approach the asymptotic regime (the boundary layer theory uses Ro as a small parameter). To compare the simulations to the boundary layer theory, we follow the same approach as was used by Kunen *et al.* [38], where they compared the structure of the sidewall boundary layer in rotating convection obtained from nonlinear numerical simulations to that obtained from boundary layer theory. Their flow is different to the one considered here, but the same strategy applies. The theoretical results qualitatively describe the structure of the flow, but the actual value of the velocity is only determined up to a multiplicative constant. That constant is selected such that the peak value of the w-component of velocity closest to the sidewall matches the one

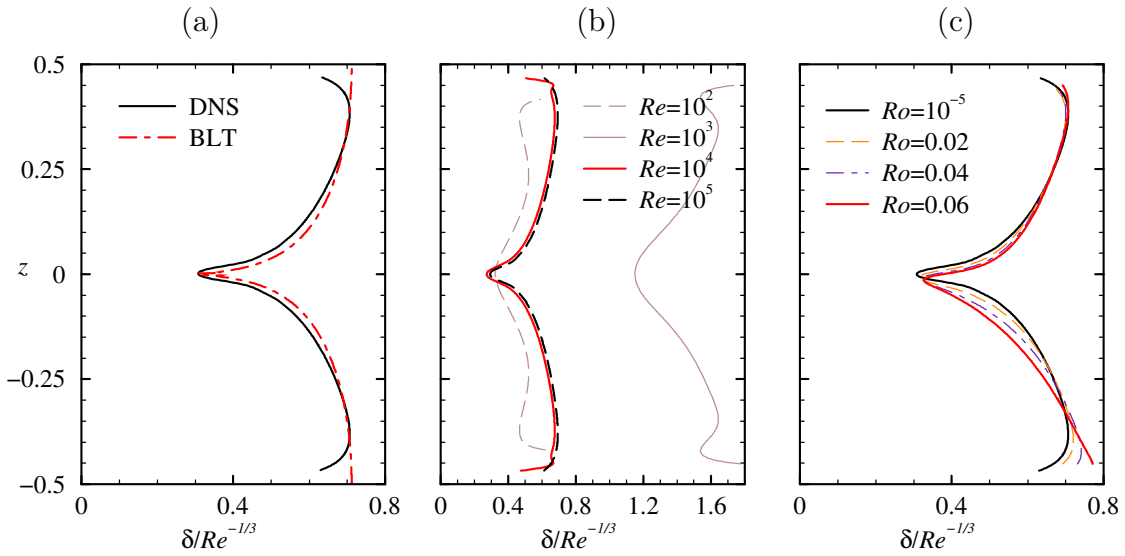


Figure 2.5: Scaled sidewall boundary layer thickness, $\delta/Re^{-1/3}$, along the length of the cylinder; (a) nonlinear numerical results (DNS) for $Re = 10^5$, $Ro = 10^{-5}$ and $\gamma = 1$, compared to the boundary layer theory (BLT) of van Heijst [96], (b) numerical results for $Ro = 10^{-5}$, $\gamma = 1$, and Re as indicated, and (c) numerical results for $Re = 10^5$, $\gamma = 1$ and Ro as indicated.

obtained by numerical simulation. Following the same strategy, for the split cylinder problem studied here, we find this constant to be $C = 0.4252$ in the case presented in Figure 2.4. In this figures the radial profile of w near the sidewall at mid-hieght $z = 0$ determined from DNS at $Re = 10^5$, $Ro = 10^{-5}$ and $\gamma = 1$ is compared with the one obtained from the boundary layer theory (BLT) of van Heijst [96], scaled with the constant C. There are appreciable quantitative differences, such as the radial position of the first extremum from the wall, between the profiles even following this scaling, and these are likely due to the curvature and nonlinear terms not being included in the theoretical profile.

One of the main characteristics of the sidewall boundary layer is its thickness.

Figure 2.5(a) compares the sidewall boundary layer thickness $\delta(z)$ scaled by $Re^{-1/3}$ obtained from numerical simulation in the case $\gamma = 1$, $Ro = 10^{-5}$ and $Re = 10^5$, with the result obtained by van Heijst [96] using boundary layer analysis for the same Reynolds number (his results are described as a function of the Ekman number, which is proportional to Re^{-1}). This boundary layer thickness, $\delta(z)$, is determined as the radial distance from the sidewall where the azimuthal vorticity first changes sign (corresponding to the first peak in the axial velocity w since the radial velocity u in the boundary layer is insignificant). To study this thickness, we use the same idea as in the previous paragraph, and find a multiplicative constant to scale the thickness of the theoretically determined boundary layer thickness such that the position of the peak value of the axial component of velocity closest to the sidewall matches the one obtained by numerical simulation using a least square approach over the whole height. This constant value is $K = 0.78329976$. The figure clearly shows that the shape of the boundary layer is well captured by the theory, except for the regions very close to the top and bottom of the sidewall where the Ekman layers are important.

We now consider the structure of the sidewall boundary layer for parameters outside the asymptotic regime in which the boundary layer equations are derived. The boundary layer theory gives that $\delta \sim Re^{-1/3}$. Figure 2.5(b) shows the scaled sidewall boundary layer thickness $\delta/Re^{-1/3}$. We see that the scaling is attained for $Re \geq 10^4$; for smaller Re there is significant departure from this scaling, suggesting that curvature effects (neglected in the theory) become important as the boundary layer thickness increases with smaller Re.

Increasing the differential rotation, Ro, affects the shape of the boundary layer but essentially not its thickness. The shape is almost symmetric about the cylinder half-height for $Ro \lesssim 0.001$ (perfect reflection symmetry is only attained at $Ro = 0$). However, with increasing Ro, Fig. 2.5(c) shows that it becomes more asymmetric, due

(a) ψ: $Ro = 10^{-5}$ (b) v: $Ro = 10^{-5}$ (c) ψ: $Ro = 0.06$ (d) v: $Ro = 0.06$

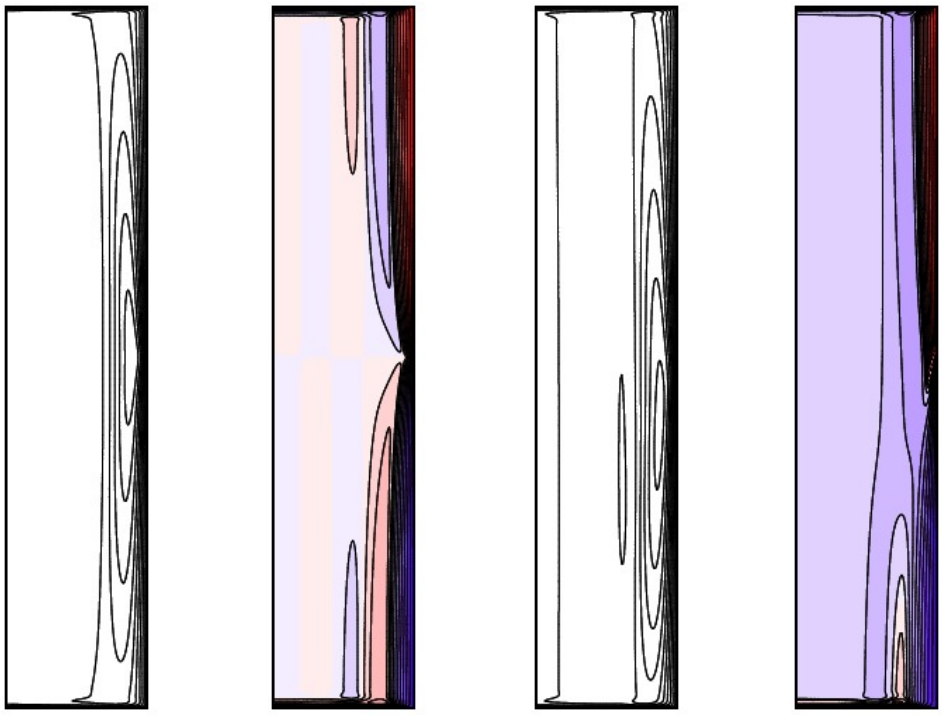


Figure 2.6: Streamlines and contours of v close to the sidewall of the cylinder ($0.8 \leq r \leq 1.0$), for $Re = 10^5$, $\gamma = 1$ and Ro as indicated. There are 10 contour levels, quadratically spaced with $\psi \in [0, 5 \times 10^{-8}]$ and $v \in [-10^{-5}, 10^{-5}]$ for $Ro = 10^{-5}$ and $\psi \in [0, 2.5 \times 10^{-4}]$ and $v \in [-0.06, 0.06]$ for $Ro = 0.06$.

to the increasing strength of the flow being transported from the top (faster rotating) endwall layer to the bottom layer.

Figure 2.6 shows streamlines and contour of the azimuthal velocity in the sidewall region ($0.8 \leq r \leq 1.0$, $-\gamma/2 \leq z \leq \gamma/2$), for $Re = 10^5$, $\gamma = 1$ and $Ro = 10^{-5}$ and $Ro = 0.06$ respectively, and Fig. 2.7 shows zoomed-in views of those plots very close to the split in the wall. These show that the solutions are very smooth and well-behaved in this region, both for small and not so small differential rotations Ro, and that the

(a) ψ: $Ro = 10^{-5}$ (b) v: $Ro = 10^{-5}$ (c) ψ: $Ro = 0.06$ (d) v: $Ro = 0.06$

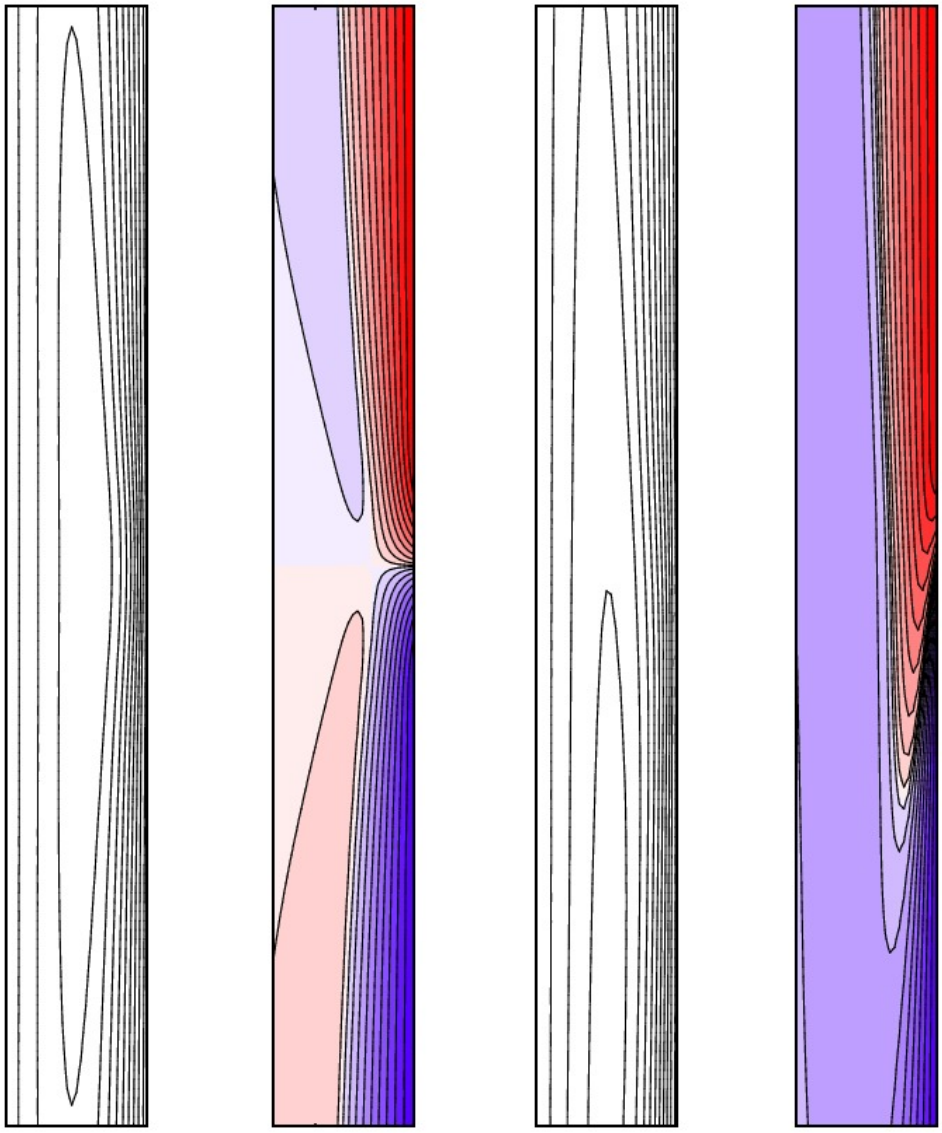


Figure 2.7: Streamlines and contours of v zoomed into the split in the sidewall ($0.95 \leq r \leq 1.0$ and $-0.2 \leq z \leq 0.2$), for same cases as shown in Fig. 2.6. There are 10 contour levels, quadratically spaced with $\psi \in [0, 5 \times 10^{-8}]$ and $v \in [-10^{-5}, 10^{-5}]$ for $Ro = 10^{-5}$ and $\psi \in [0, 2.5 \times 10^{-4}]$ and $v \in [-0.06, 0.06]$ for $Ro = 0.06$.

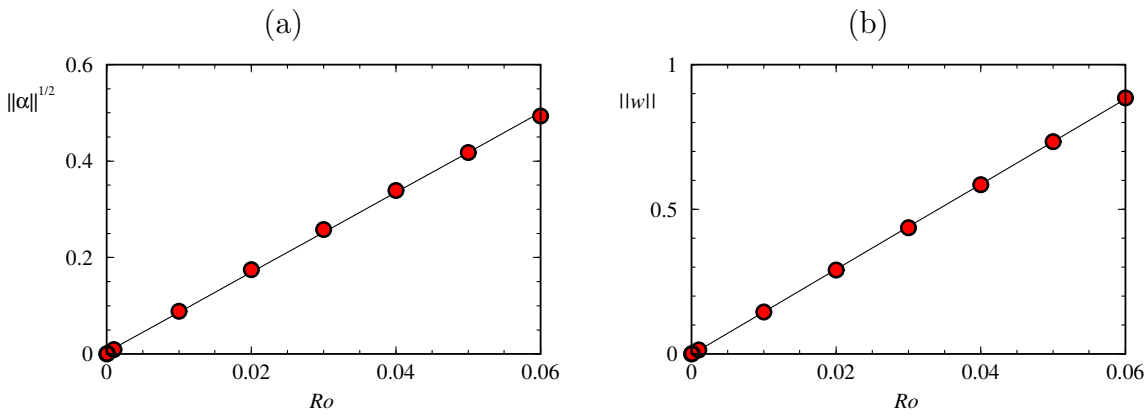


Figure 2.8: Variation of (a) $\sqrt{||\alpha||}$ and (b) $||w||$, with Ro.

vertical gradients in v in the inner boundary layer drive a meridional flow directed downwards. The overall structure remains similar, with evident asymmetry increasing with Ro. In order to quantify the asymmetry of the flow, we introduce a symmetry parameter

$$\alpha(r, z) = w(r, z) - w(r, -z). \tag{2.6}$$

Figure 2.8(a) shows $\sqrt{||\alpha||}$ versus the Rossby number, where $||.||$ is the two norm. The asymmetry in the flow grows proportionally with Ro^2. The strength of the vertical flow responsible for this asymmetry is quantified by $||w||$, the two norm of the vertical velocity. This parameter grows linearly with Ro, as shown in Fig. 2.8(b).

Figure 2.9 presents the radial profiles close to the sidewall of w for $Re = 10^5$, $\gamma = 1$ and various Ro and at various vertical positions in the cylinder. These velocity profiles are scaled with Ro, as suggested by Fig. 2.8(b). From the streamlines in Fig. 2.6 and the radial profiles of w in Fig. 2.9, it is clear that a significant portion of this vertical flow is turned upwards upon reaching the bottom. Upon reaching the top, a portion is turned downwards and so on, until a radial distance of order $Re^{-1/4}$ is reached and then the vertical velocity is very weak and directed upwards. For a given,

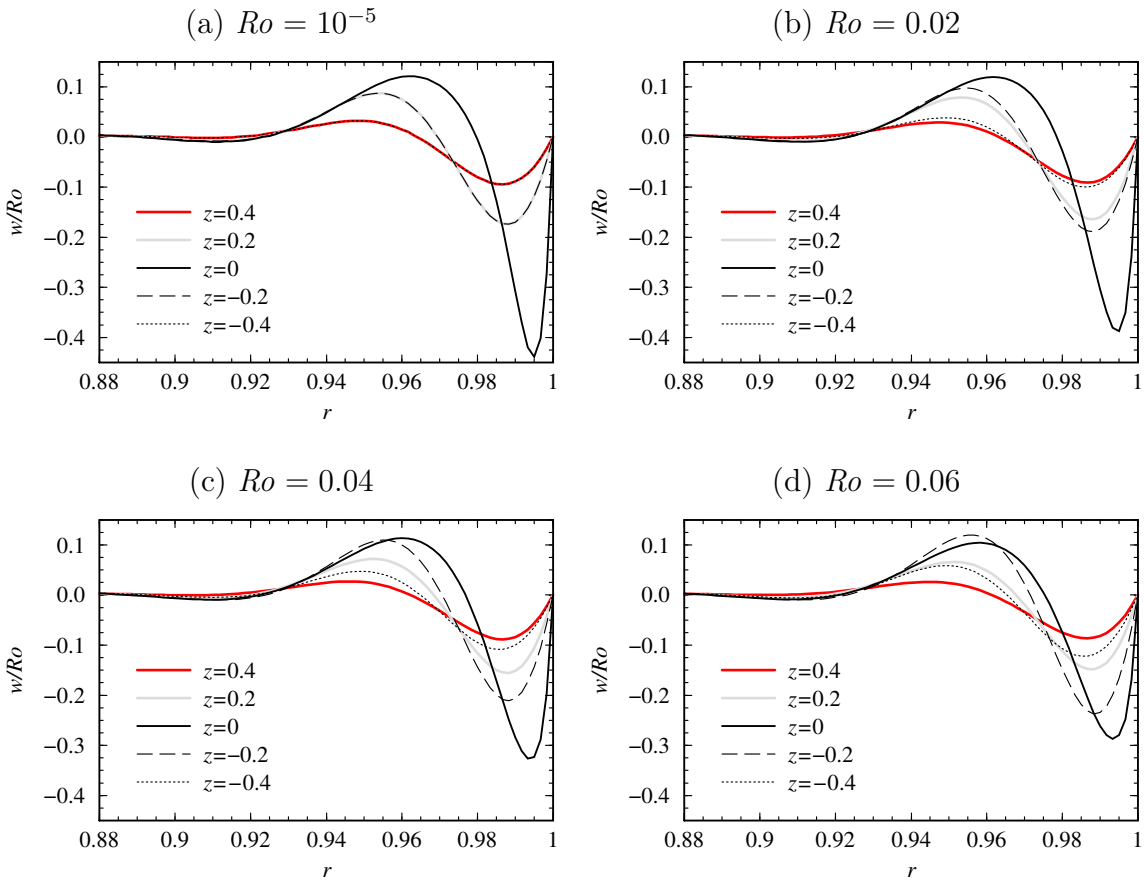


Figure 2.9: Vertical velocity profiles close to the sidewall of the cylinder for $Re = 10^5$, $\gamma = 1$ and Ro as indicated.

large enough Re, the radial position of where the vertical velocity changes sign varies weakly with Ro, as is evident in Fig. 2.9. The growing asymmetry with increasing Ro, and the relative strengths of the upward and downward flows at different radial distances from the sidewall can be also appreciated in this figure.

2.5 Axisymmetric Instabilities of the Sidewall Layer

We now consider the stability of the basic state at $Re = 10^5$, which is large enough for the boundary layer asymptotic regime to hold, as the differential rotation Ro

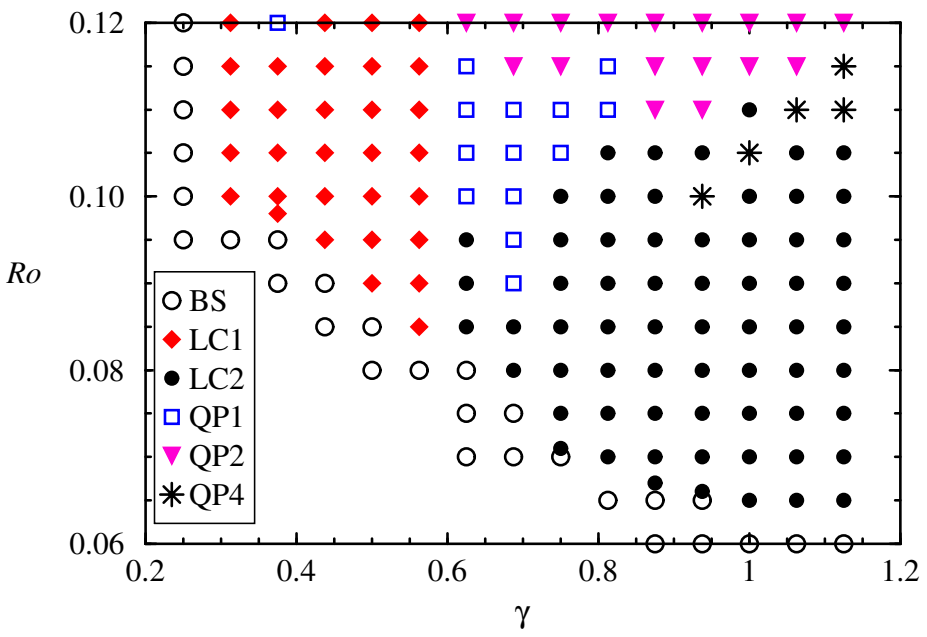


Figure 2.10: Regime diagram in (Ro, γ)-space, showing the various axisymmetric states found near the double-Hopf bifurcation for $Re = 10^5$.

and the cylinder aspect-ratio γ are varied. In this first study, we shall only consider axisymmetric instabilities.

When the differential rotation is sufficiently large, the basic state loses stability in a variety of ways, depending on the aspect ratio. The bottom corner region, which is analytically inaccessible, becomes dynamically important as the flow from the upper half of the sidewall boundary layer reaches it, and along with the sidewall boundary layer in the lower half, plays an important role in the flow instabilities. The regime diagram, Fig. 2.10, shows the loci of different solutions in (Ro, γ)-parameter space for $Re = 10^5$. For small Ro and γ, the basic state is stable and it loses stability to two different time-dependent states, LC1 and LC2, as either Ro or γ are increased. For larger Ro and smaller γ, there is a supercritical Hopf bifurcation to the limit cycle LC1 with frequency ω_1, whereas for larger γ and smaller Ro, there is a different

supercritical Hopf bifurcation to the limit cycle LC2 with frequency ω_2. At about $Ro = 0.08$ and $\gamma = 0.6$, there is a point where the two Hopf bifurcations occur simultaneously, and as is typical in double-Hopf bifurcations Kuznetsov [39], there is a region of parameter space anchored at the double-Hopf point and delimited by Neimark-Sacker bifurcation curves where a mixed mode exists. Since ω_1 and ω_2 are generically incommensurate, the mixed mode QP is quasi-periodic. The regime diagram also includes regions further removed from the double-Hopf point where QP has undergone a pair of period-doubling bifurcations to states QP2 and QP4.

The oscillations in LC1 are localized at the bottom corner where the sidewall and bottom endwall meet. There is a periodic swelling of the sidewall boundary layer near the corner, as can be seen in a snap-shot of the azimuthal vorticity at $Re = 10^5$, $Ro = 0.11$ and $\gamma = 0.5$ shown in Fig. 2.11(a) and more clearly in the accompanying online movie (LC1.avi). The frequency $\omega_1 \approx 1.89$ can be appreciated in the power spectral density of the time-series of Ek in Fig. 2.11(a), where

$$\mathrm{Ek} = 0.5 \int_{-0.5\gamma}^{0.5\gamma} \int_{0}^{1} \boldsymbol{u}^2 r \mathrm{d}r\mathrm{d}z. \tag{2.7}$$

Linear inviscid theory for rapidly rotating flow Greenspan [24] gives that inertial waves can be generated in rapidly rotating flows if the disturbance frequency is less than twice the angular speed Ω of the flow. Since we non-dimensional time with Ω, disturbances with non-dimensional frequency $\omega_\mathrm{d} < 2$ are expected to generate inertial waves, and these should obey the dispersion relation giving the angle at which they propagate with respect to the rotation axis as $\beta = \arccos(\omega_\mathrm{d}/2)$. For $\omega_\mathrm{d} = \omega_1 \approx 1.89$, the inertial wave beams should propagate into the bulk at an angle $\beta_1 \approx 19°$, emanating from the bottom corner region where the periodic disturbance associated with the Hopf bifurcation is localized. Indeed, Fig. 2.11(a) shows such inertial waves.

The LC2 state is very different to LC1. To begin with, the oscillations are localized

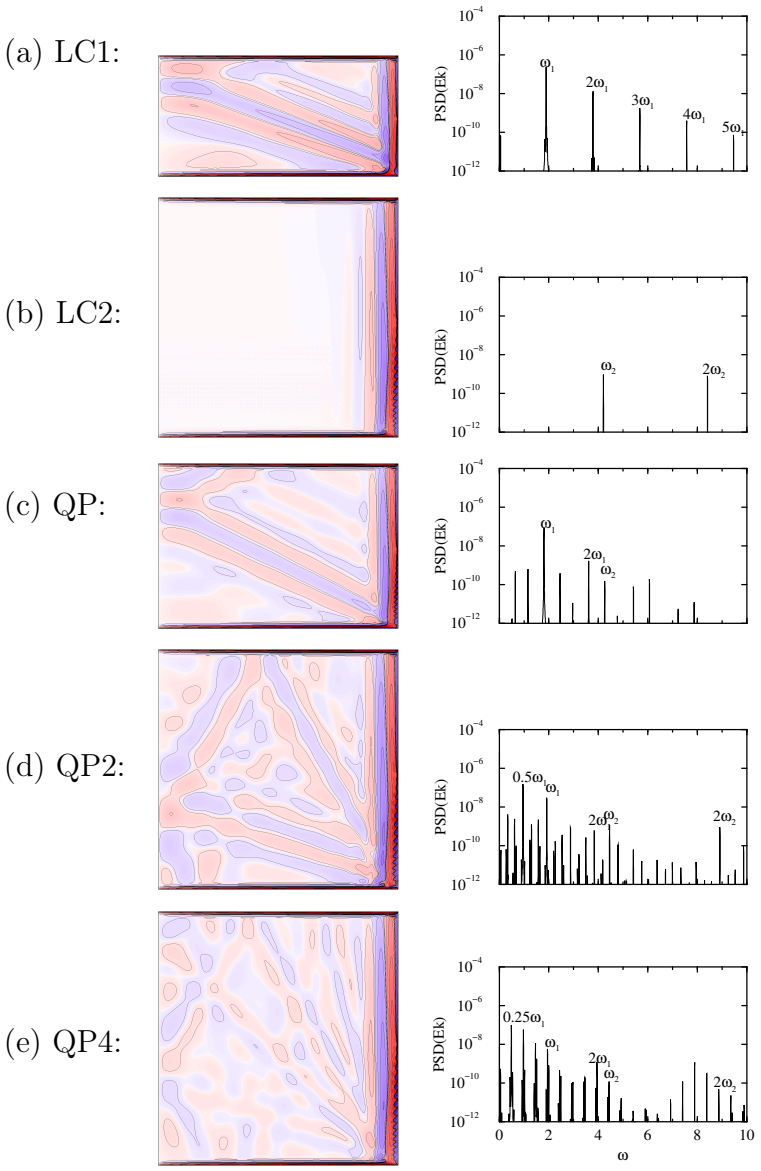


Figure 2.11: Snapshots of η (left) and the corresponding power spectral densities of Ek (right), at $Re = 10^5$ for (a) LC1 at $Ro = 0.11$, $\gamma = 0.5$, (b) LC2 at $Ro = 0.11$, $\gamma = 1$, (c) QP at $Ro = 0.105$, $\gamma = 0.6875$, (d) QP2 at $Ro = 0.12$, $\gamma = 1$, and (e) QP4 at $Ro = 0.11$, $\gamma = 1.0625$. Ten cubically spaced contour levels are in the range $\eta \in [-5, 5]$. Movies of η for each case shown are available online; the corresponding movies are titled LC1.avi, LC2.avi, QP.avi, QP2.avi and QP4.avi.

in the deep sidewall boundary layer just below the split at half-height. They consist of a periodic train of roll vortices traveling down the sidewall all the way to the bottom corner. Furthermore, the frequency associated with this oscillation is $\omega_2 \approx 4.23$, which is too high to generate inertial waves in the interior, which continues to rotate as an essentially solid body, as in the basic state BS. Figure 2.11(b) shows that all the azimuthal vorticity is contained inside the top and bottom Ekman layers and in the sidewall layer, and the LC2 downward traveling rollers in the deep sidewall layer are clearly evident in the accompany online movie (LC2.avi).

For the quasiperiodic state QP, found after crossing either of the Neimark-Sacker bifurcation curves, Fig. 2.11(c) and the accompanying online movie (QP.avi) illustrate the behavior of the mixed mode. The instabilities are present in the bottom half of the sidewall as in LC2, superposed with the instability in the corner resulting from LC1 that drives inertial waves. A power spectral density of the time-series of Ek for QP shown in Fig. 2.11(c) comprises of strong peaks at frequencies ω_1 and ω_2, their relative strengths depend on the distance in (Ro, γ)-space the QP case under consideration is from the two Neimark-Sacker curves, and their linear combinations. The peaks at the linear combinations are weaker than the peaks at ω_1 and ω_2, but there are several peaks at frequencies $m\omega_1 + n\omega_2 < 2$ (m and n integers) and if they are sufficiently strong, they can also generate inertial waves at angles $\arccos(m\omega_1 + n\omega_2)/2$. For the example shown in Fig. 2.11(c), these other frequencies are too weak and the related inertial waves are negligible compared to the inertial wave generated by the peak at ω_1. Note that the frequencies ω_1 and ω_2 are (weak) functions of Ro and γ, and so the angle of the inertial wave in Fig. 2.11(c) differs from that in Fig. 2.11(a).

The dependence of ω_1 and ω_2 on Ro and γ can lead to low order frequency lockings and have combinations $m\omega_1 + n\omega_2$ that give strong peaks at subharmonics of ω_1. This seems to be the case with QP2 and QP4 which have strong peaks at frequencies $\omega_1/2$

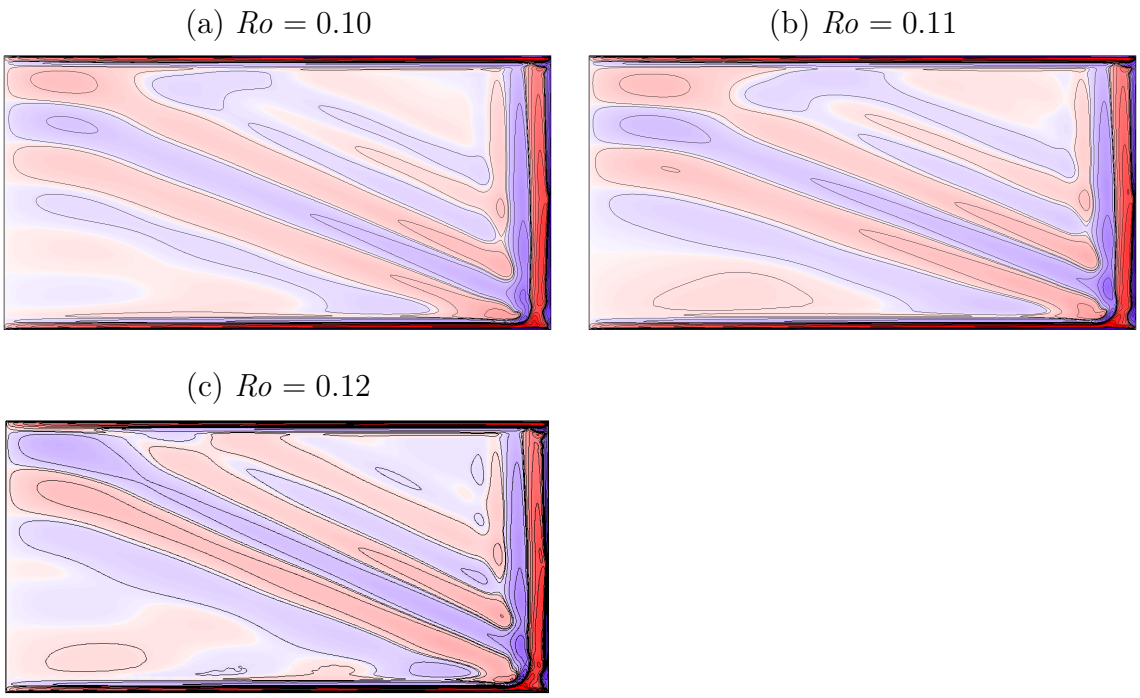


Figure 2.12: Snapshots of η at $Re = 10^5$, $\gamma = 0.5$ and Ro as indicated. Ten cubically spaced contour levels are in the range $\eta \in [-5, 5]$.

and $\omega_1/4$, respectively (see Fig. 2.11d and e). Figure 2.11(d) and the accompanying online movie (QP2.avi) show the azimuthal vorticity of a QP2 case, with an inertial wave beam generated by ω_1 with angle $\beta \approx 20°$, very similar to the QP case in Fig. 2.11(c), and another beam at angle $\beta \approx 62°$ corresponding to the peak at $\omega_1/2$. The QP4 case shown in Fig. 2.11(e) and in the accompanying online movie (QP4.avi) has an even more complicated inertial wave structure, but one can decipher beams at about 20°, 45°, 62° and 76° (corresponding to ω_1, $3\omega_1/4$, $\omega_1/2$ and $\omega_1/4$), but they are not as clean as in the other cases, probably due to interference between the beams and their reflections, as well as further contributions from other linear combinations of frequencies.

As mentioned earlier, the frequencies ω_1 and ω_2 are (weak) functions of Ro and γ

(a) $Ro = 0.11$ (b) $Ro = 0.115$

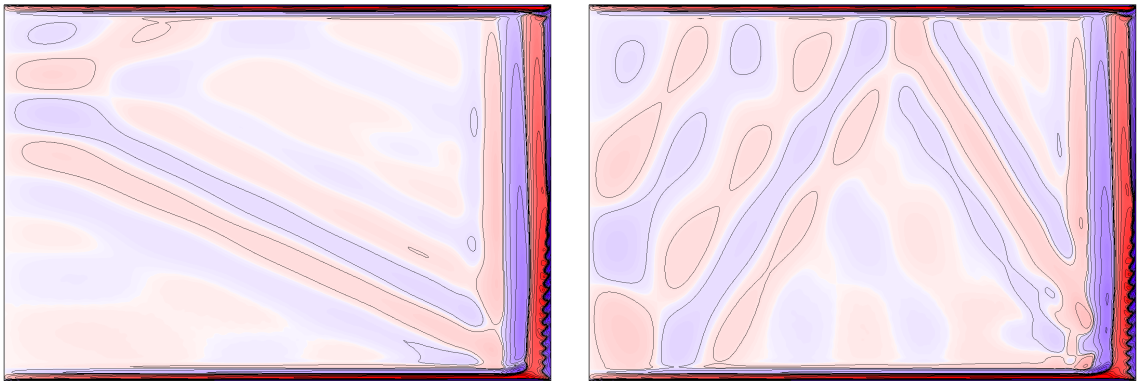


Figure 2.13: Snapshots of η at $Re = 10^5$, $\gamma = 0.6875$ and Ro as indicated. Ten cubically spaced contour levels are in the range $\eta \in [-5, 5]$.

and this variation in frequencies results in changes in the angle of the inertial waves. To illustrate this, we fix $\gamma = 0.5$ and slightly modify Ro from 0.10 to 0.12. For $Ro = 0.10$, the flow is LC1 with frequency $\omega_1 \approx 1.87$, so $\beta_1 \approx 21°$. Figure 2.12(a) shows a snap-shot of the azimuthal vorticity for this case. The LC1 case with $Ro = 0.11$ shown in Fig. 2.12(b) has $\omega_1 \approx 1.89$ and $\beta_1 \approx 19°$. For $Ro = 0.12$, shown in Fig. 2.12(c), LC1 has $\omega_1 \approx 1.84$ and $\beta_1 \approx 23°$. In these relatively simple examples, small changes in Ro of about 10%, lead to changes in the Hopf frequency of about 2% and result in beam angle changes of about 2°. While these changes in the wave beam angle are small, they result in differences in where the beams reflect off the endwalls and lead to larger variations in their constructive and destructive interference as beams interact.

However, sometimes a small change in the parameter Ro can lead to a large change in the predominant frequency owing to period-doubling or period-quadrupling of the instability. For example, for $Re = 10^5$, $\gamma = 0.6875$ and $Ro = 0.110$ the dominant frequency is approximately 1.81 that generates a wave beam with angle $\beta \approx 25°$, as illustrated in Fig. 2.13(a). However, Fig. 2.13(b) shows that with a very small

increase in Ro of only 0.005, the doubled period appears and the dominant frequency is $\omega \approx 1.04$ with corresponding $\beta \approx 58°$. In this case the small change in Ro resulted in a small change in the frequency from 1.81 to 2.08, and it is the 2.08 which is halved to 1.04 that results from period doubling. The frequency 2.08 is too large to drive inertial waves, and the inertial wave pattern we observed corresponds to the period-doubled 1.04 frequency. This figure also very clearly illustrates the reflection of the wave beams at the top and bottom endwalls.

2.6 Discussion and Conclusions

We have analyzed the flow in a split differentially rotating cylinder using numerical simulations of the flow. This flow had been previously considered from a linear boundary layer analysis perspective, which elucidated the complicated structure of the sidewall boundary layer. The basic flow is driven by the radial flow out of the Ekman layer on the faster rotating top endwall being turned into the sidewall boundary layer. The downflow closest to the sidewall continues flowing down past the split in the differentially rotating sidewall until it reaches the bottom corner region. The flow very close to the sidewall is turned into the bottom slower rotating endwall boundary layer, where it continues to swirl radially inward in the Ekman layer and effuses slowly upward to the top endwall layer. This sets up a quasi-geostrophic interior flow that is essentially in solid body rotation at a rotation rate of about the average rate of the top and bottom halves of the cylinder. The rest of the downflow in the sidewall layer is turned back upwards in an outer region of the sidewall layer; this flow is considerably slower than the downflow nearest the sidewall, and upon reach the neighborhood of the top, it is turned back downward, leading to the complicated spatially oscillatory radial structure of the sidewall boundary layer. The boundary layer analysis captures this structure very well when the mean rotation is sufficiently large for the boundary

layer approximation to be valid and when the differential rotation is small enough for nonlinearities to be negligible. Our numerical simulations confirm this, and show that rotation needs to be about 10^4 times faster than viscous dissipation (i.e. $Re > 10^4$) for the boundary layer approximation to be valid. The smallness of the differential rotation is not so restrictive for a similar qualitative picture of the boundary layer structure to emerge. The main effect of the differential rotation not being infinitesimally small is to accentuate the lack of reflection symmetry about the cylinder half-height due to the large scale meridional flow described above.

We have then explored how nonlinearity affects the flow. In a rapidly rotating regime, where the boundary layer analysis is valid ($Re = 10^5$) we have considered variations in both the differential rotation, Ro and the cylinder aspect ratio γ. As Ro is increased the magnitude of the downflow w in the sidewall boundary layer grows linearly with Ro, and the asymmetry in this downflow ($w(r,z) - w(r,-z) \neq 0$) grows even faster, as Ro^2, so that the maximum in w in the sidewall layer is displaced some distance down from the split at the cylinder half-height, $z = 0$. The boundary layer flow in the vicinity of this local maximum in w and in the bottom corner region becomes unstable in a variety of ways.

For small γ (less than about 0.6) and large Ro (greater than about 0.8), the downflow strongly affects the corner region, which periodically swells and deflates. This limit cycle state comes about via a supercritical Hopf bifurcation and the frequency of the oscillations is less than twice the mean rotation rate of the interior bulk flow, and so inertial waves are emitted from the corner region deep into the bulk interior flow. On the other hand, for larger γ and smaller Ro, the longer sidewall boundary layer flow first becomes unstable to a series of rollers traveling downstream of the split in the cylinder (where the local maximum in w squeezes the boundary layer to be thinnest), also via a supercritical Hopf bifurcation. This instability has faster

dynamics with the frequency being about four times the bulk rotation rate, and so in and of itself, it does not drive inertial waves. These two Hopf bifurcations meet at a codimension-two point in (γ, Ro) space, where a mixed mode associated with the double-Hopf bifurcation is spawned. The mixed mode near onset is approximately a super-position of the two limit cycle states resulting from each Hopf bifurcation, and as such it is quasi-periodic. The two frequencies are in general incommensurate, and the linear combinations of these two frequencies that are less than twice the bulk rotation rate, corresponding inertial waves can be driven if the associated power at those frequencies is sufficiently strong. The inertial waves beams reflect off the endwalls, and for the finite viscosity problem we consider ($Re = 10^5$), the reflecting wave beams cause a localized disturbance in the Ekman layers which is transmitted into the sidewall layer providing a feedback to the instability that drives the inertial waves. The waves for which the feedback is strongest can be expected to adjust the frequency of the instability. We have identified a number of such cases where the resulting quasi-periodic flow has a power spectral density with the strongest signal not being at either of the two primary frequencies associated with the double-Hopf bifurcation, but rather it is at one half or one quarter of one of them.

The present axisymmetric study sets the scene for a future investigation into the role of three-dimensional perturbations.

Acknowledgements

This work was supported by the U.S. National Science Foundation grant CBET-1336410.

Chapter 3

INSTABILITIES AND INERTIAL WAVES IN A RAPIDLY ROTATING SPLIT-CYLINDER FLOW

3.1 Abstract

The nonlinear dynamics of the flow in a differentially rotating split cylinder is investigated numerically. The differential rotation, with the top half of the cylinder rotating faster than the bottom half, establishes a basic state consisting of a bulk flow that is essentially in solid-body rotation at the mean rotation rate of the cylinder and boundary layers where the bulk flow adjusts to the differential rotation of the cylinder halves, which drives a strong meridional flow. There are Ekman-like layers on the top and bottom endwalls, and a Stewartson-like sidewall layer with a strong downward axial flow component. The complicated bottom corner region, where the downward flow in the sidewall layer decelerates and negotiates the corner is the epicenter of a variety of instabilities associated with the local shear and curvature of the flow, both of which are very non-uniform. Families of both high and low azimuthal wavenumber rotating waves bifurcate from the basic state in Eckhaus bands, but the most prominent states found near onset are quasiperiodic states corresponding to mixed-modes of the high and low azimuthal wavenumber rotating waves. The frequencies associated with most of these unsteady three-dimensional states are such that spiral inertial wave beams are emitted from the bottom corner region into the bulk, along cones at angles that are well predicted by the inertial wave dispersion relation, driving the bulk flow away from solid-body rotation.

3.2 Introduction

Flow instability, transition and turbulence in systems in fast rotation continue to attract much fundamental interest due to their prevalence in many practical flows, covering a large range from industrial flows, such as in turbo-machinery, to geophysical and astrophysical flows [15, 17, 41, 43]. In enclosed incompressible rotating flows, differential rotation drives secondary flows that are responsible for instability and transition [19, 45, 46]. However, when the mean or background rotation is very fast, the Coriolis restoring force tends to restrict secondary flows to the boundary layers, leading to interior flow essentially in solid-body rotation at the mean rotation rate if the differential rotation is steady and there is no unsteadiness introduced from boundary layer instabilities. If the differential rotation is unsteadily driven, then if the forcing frequency is less than twice the background rotation frequency, the interior flow can be driven away from solid-body rotation, typically by internal wave beams emanating from where the secondary flow abruptly changes its character. Typically, in enclosed cylinders this happens at the corners where the sidewall and the endwalls meet [56], in spherical containers at the critical latitudes [33], and in cubes from the edges [7]. Even when the differential rotation is steady, the boundary layer and corner flows can become unstable, and if the resulting instabilities have appropriate frequency spectra, inertial wave beams can be emitted into the interior flow [55, 88].

When the differential rotation is due to the counter rotation of the endwalls of a cylindrical container, massive boundary layer separations ensue leading to bulk flows with complicated spatio-temporal structure in the interior; the mean rotation rate is typically small and the action of the Coriolis restoring force is essentially not present [50, 74, 75]. However, when the differential rotation is due to co-rotation, the Coriolis force is strong and instabilities are localized within the sidewall boundary layer

[27, 46, 54]. The study of the sidewall boundary layer goes back to Stewartson [92], who considered the structure of the boundary layer in the limit of small differential rotation and small viscosity. Stewartson [92] also considered the cylindrical shear layer that is produced in the interior flow between two rotating disks that are split at a common radial distance from the axis, with the inner part rotating differentially to the outer part. The shear layer problem has an extensive subsequent literature, the most recent being the studies of Vo *et al.* [98, 99, 100]. In both of Stewartson's problems, the radial structure of the interior shear layer and the sidewall boundary layer have thicknesses that scale with the kinematic viscosity of the fluid ν. There is a $\nu^{1/4}$ scaling in which the differential rotation is adjusted, and a $\nu^{1/3}$ scaling in which the driven meridional circulation is adjusted. The meridional flow is driven by the endwall boundary layers whose thickness scale as $\nu^{1/2}$.

In most cases studied where a Stewartson-type sidewall boundary layer exists in a cylindrical geometry, it results from the differential rotation between the sidewall and one or both endwalls, and when the layer becomes unstable it is not clear what role the discontinuity at the corner plays. Stewartson-type layers without the presence of a discontinuous corner have also been studied in the idealized setting of an infinitely long cylinder that is split with the top part rotating differentially to the bottom part [90]. Hocking [30] also studied this flow, but did not analyze the boundary layer structure. For a finite enclosed split-cylinder, van Heijst [96] showed that the meridional flow driven by the endwall boundary layers altered the roles of the $\nu^{1/4}$ and $\nu^{1/3}$ sidewall layers in a subtle fashion depending on where the cylinder was split along the sidewall. In particular, the $\nu^{1/4}$ layer is unable to adjust the differential rotation on its own and neither is the $\nu^{1/3}$ layer able to adjusted the meridional circulation on its own, but a combination of the two accomplishes the correct adjustments. All of these split-cylinder results cited so far are obtained in the limit of small viscosity and small differential

rotation and the stability of the flows was not considered. Gutierrez-Castillo and Lopez [25] relaxed these constraints and considered the nonlinear viscous problem, albeit restricted to the axisymmetric subspace, elucidating the complicated structure of the basic state. The boundary layer at the faster rotating top endwall drives flow radially outward and down into the $\nu^{1/3}$ sidewall layer; the split in the cylinder at half-height locally affects the boundary layer thickness but does not directly impact the flow which continues down and is turned at the bottom corner. The sidewall boundary layer flow that is closest to the sidewall continues past the corner and is feed radially inwards into the bottom boundary layer from which it effuses slowly upward toward the top endwall, setting up the interior flow that is essentially in solid-body rotation. The rest of the sidewall boundary layer flow is turned at the bottom corner and flows upward in the outer part of the sidewall layer. Two axisymmetric instabilities were found, one consisting of a periodic swelling and deflation of the bottom corner flow region at a low enough frequency that inertial wave beams are emitting into the interior from the corner. The other instability consisted of a series of axisymmetric rollers traveling down the inner sidewall layer; their associated frequency was too large (about four times the background rotation frequency) and no inertial wave beams were emitted. Furthermore, over a considerable range of parameters, quasiperiodic states which have characteristics of both limit cycle states were found. Similarities were found between the characteristics of these states and those found in the flow where the differential rotation is driven by a faster rotating top endwall when restricted to the axisymmetric subspace. In that case the base flow is primarily unstable to three-dimensional rather than axisymmetric instabilities [54]. These similarities and the question of the role of the discontinuity motivated us to explore the fully nonlinear three-dimensional rapidly rotating split-cylinder flow.

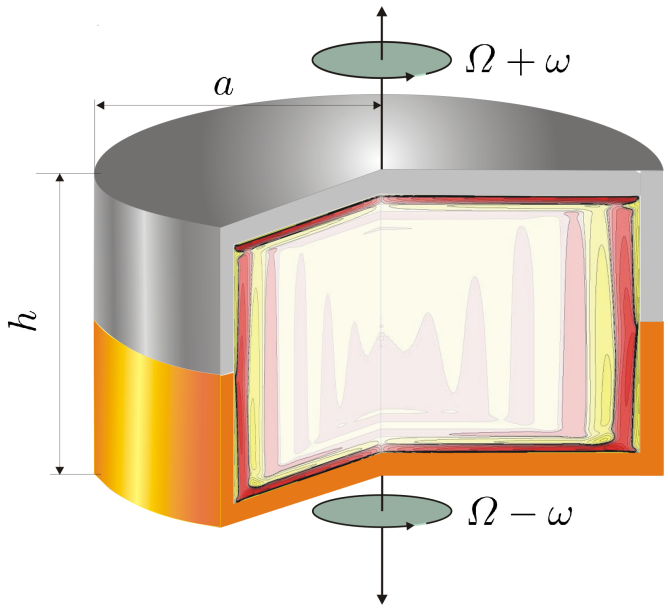


Figure 3.1: Schematic of the flow system. The inset shows contour of the azimuthal vorticity η of the basic state at $Re = 1.2 \times 10^4$, $Ro = 0.23$ and $\gamma = 1$. There are ten contour levels in the range $\eta \in [-5, 5]$, cubically spaced.

3.3 Governing Equations and Numerical Methods

Consider a circular cylinder of radius a and height h, completely filled with a fluid of kinematic viscosity ν, and rotating at a mean angular speed Ω. The cylinder is split in two at mid-height, with the top half rotating faster, with angular speed $\Omega + \omega$, than the bottom half that has angular speed $\Omega - \omega$. A schematic of the flow system is shown in figure 3.1.

The flow is governed by the Navier–Stokes equations, which are non-dimensionalized using a as the length scale and $1/\Omega$ as the time scale, giving

$$(\partial_t + \boldsymbol{u} \cdot \nabla)\boldsymbol{u} = -\nabla p + 1/Re \nabla^2 \boldsymbol{u}\,, \qquad \nabla \cdot \boldsymbol{u} = 0\,, \tag{3.1}$$

where $\boldsymbol{u} = (u, v, w)$ is the velocity field in cylindrical polar coordinates $(r, \theta, z) \in [0, 1] \times [0, 2\pi] \times [-\gamma/2, \gamma/2]$, and p is the kinematic pressure. The corresponding

vorticity field is $\nabla \times \boldsymbol{u} = (\xi, \eta, \zeta)$. There are three governing parameters:

$$\begin{aligned} &\text{Reynolds number} && Re = \Omega a^2/\nu, \\ &\text{Rossby number} && Ro = \omega/\Omega, \\ &\text{aspect ratio} && \gamma = h/a. \end{aligned} \tag{3.2}$$

In the present study, the aspect ratio has been kept fixed at $\gamma = 1$.

The boundary conditions are no-slip:

$$\begin{aligned} &\text{top endwall, } z = 0.5\gamma: && (u, v, w) = (0, r(1 + Ro), 0), \\ &\text{bottom endwall, } z = -0.5\gamma: && (u, v, w) = (0, r(1 - Ro), 0), \\ &\text{top half of sidewall, } r = 1,\ z \in (0, 0.5\gamma]: && (u, v, w) = (0, 1 + Ro, 0), \\ &\text{bottom half of sidewall, } r = 1,\ z \in [-0.5\gamma, 0): && (u, v, w) = (0, 1 - Ro, 0). \end{aligned} \tag{3.3}$$

The system has been solved using a second-order time-splitting method, with space discretized via a Galerkin–Fourier expansion in θ and Chebyshev collocation in r and z:

$$\boldsymbol{u}(r, \theta, z, t) = \sum_{n=0}^{2n_r+1} \sum_{m=0}^{n_z} \sum_{k=-n_\theta/2}^{k=n_\theta/2-1} \hat{\boldsymbol{u}}_{mnk}(t) \Xi_n(r) \Xi_m(2z/\gamma) \mathrm{e}^{\mathrm{i}k\theta}, \tag{3.4}$$

where Ξ_n is the n-th Chebyshev polynomial. The spectral solver is based on the method described in Mercader *et al.* [66] and has been used extensively in a wide variety of enclosed cylinder flows. The results presented in this study were computed with a spatial resolution of $n_r = n_z = 100$, $n_\theta = 202$, and a time resolution of $\delta_t = 2 \times 10^{-3}$; these were sufficient to resolve the spatio-temporally complex flows associated with the sidewall and corner flow instabilities encountered in the parameter regime studied.

The jump discontinuity in the sidewall boundary condition for the azimuthal velocity is regularized by smoothing out the jump over a small distance. Specifically, the boundary condition for the azimuthal velocity is replaced with

$$v(r = 1, \theta, z) = 1 + Ro \tanh(\epsilon z), \tag{3.5}$$

where ϵ governs the distance over which the jump is smoothed out. This parameter is fixed at $\epsilon = 50$ for the simulations presented here. Details of this selection can be found in Gutierrez-Castillo and Lopez [25].

The modal kinetic energies of the Fourier modes corresponding to azimuthal wavenumbers m,

$$E_m = \frac{1}{2} \int_{-0.5\gamma}^{0.5\gamma} \int_0^1 \boldsymbol{u}_m \cdot \boldsymbol{u}_m^* \, r \mathrm{d}r \mathrm{d}z, \tag{3.6}$$

where $\boldsymbol{u}_m$ is the mth Fourier mode of the velocity field and $\boldsymbol{u}_m^*$ is its complex conjugate, provide a convenient way to characterize many of the solutions obtained.

3.4 Results

3.4.1 Basic State

The basic state, BS, is steady and axisymmetric. It is stable for sufficiently small Re and Ro, and consists of a bulk flow in solid-body rotation with $v/r \approx Re$ and boundary layers of Ekman type on the top and bottom endwalls and a Stewartson like boundary layer on the sidewall. A typical BS at $Re = 1.2 \times 10^4$ and $Ro = 0.23$ is presented in figure 3.1, which shows contours of the azimuthal vorticity, η. The contour levels are cubically spaced so that more levels are concentrated about the zero level. For pure solid-body rotation there is no meridional flow and $\eta = 0$. Figure 3.1 shows that this is essentially the case for BS for $r \lesssim 0.7$ and away from the top and bottom Ekman layers. The details of how BS changes with parameters, in particular with Ro, are provided in Gutierrez-Castillo and Lopez [25]. That study only considered axisymmetric flow, and the only instabilities of BS considered were also axisymmetric. However, as detailed in the following sections, over the wide range of parameters considered, the primary instabilities of BS are not axisymmetric.

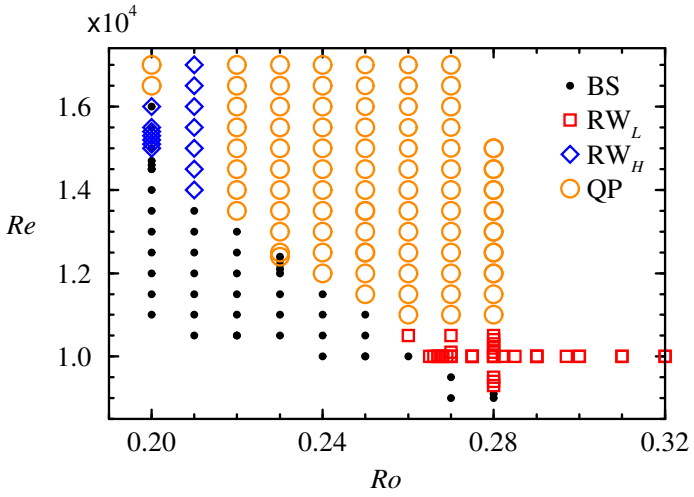


Figure 3.2: Regime diagram presenting an overview of the solutions obtained.

3.4.2 Overview of the Instabilities

Figure 3.2 shows a regime diagram in (Ro, Re) parameter space, summarizing the various types of states obtained following the instabilities of BS. The basic state BS described in the previous section (designated as small filled circles in the figure) is stable for low Ro and Re. As Re and Ro are increased, BS loses stability in a number of different bifurcations. Generally, the bifurcations are supercritical for $Ro \gtrsim 0.245$ and subcritical for $Ro \lesssim 0.245$. Flow curvature and shear in the sidewall boundary layer, and the flow negotiating the corner in the slower rotating half of the cylinder, where the bottom endwall and the sidewall meet, are the primary ingredients for the instabilities. For small Re and large Ro, one class of instabilities leads to low azimuthal wavenumber rotating waves (RW_L) concentrated in the bottom corner, and emitting inertial wave beams into the interior. These are designated by open squares in figure 3.2. For larger Re and smaller Ro, high azimuthal wavenumber rotating waves (RW_H) are found (designated by open diamonds). These are also concentrated near the bottom corner, but more deeply in the sidewall layer. There is an extensive

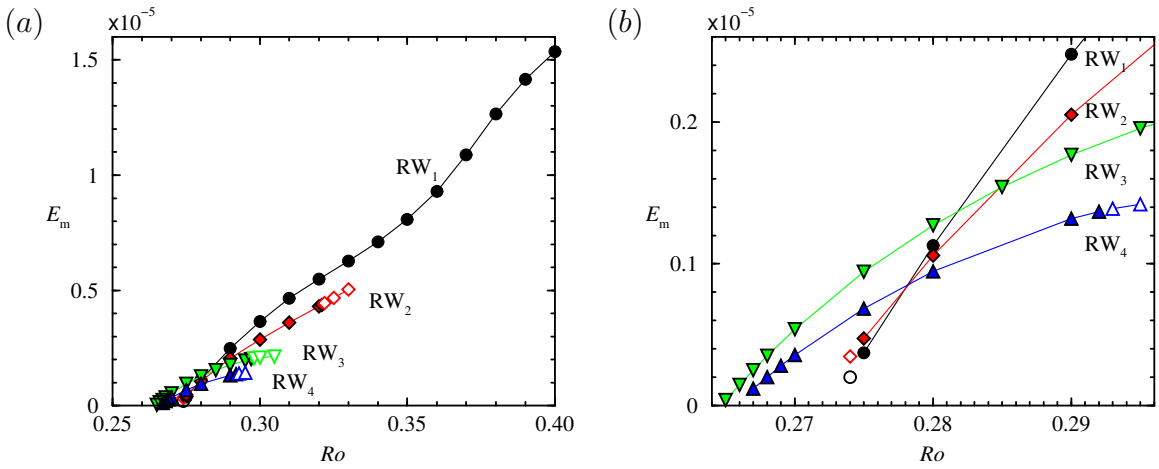


Figure 3.3: Variations of the modal kinetic energies E_m of the various rotating waves RW_m ($m \in [1, 4]$) versus Ro for $Re = 10^4$. The filled symbols correspond to stable states and open symbols to unstable states (computed in the corresponding subspaces). Panel (b) is a zoomed-in version of panel (a).

(Ro, Re) regime in between, where quasiperiodic states (QP) are found that have well-distinguished features of both RW_L and RW_H; these are designated by large open circles. All of these states exist with a range of different azimuthal wavenumbers corresponding to Eckhaus bands. In the following sections, we shall consider a number of one parameter paths in the regime diagram, describing in some detail the various instabilities and flow characteristics.

3.4.3 Low Azimuthal Wavenumber Rotating Waves

With fixed $Re = 10^4$, the basic state is stable for $Ro \lesssim 0.265$. For Ro above that critical value, BS undergoes a supercritical Hopf bifurcation that breaks axisymmetry, resulting in a rotating wave state with azimuthal wavenumber $m = 3$, RW_3. For larger Ro, a complicated bifurcational process ensues that involves a number of RW_L. A

summary of the RW_L solution branches showing their primary modal kinetic energy, E_m for RW_m, as functions of Ro is presented in figure 3.3, where panel (a) presents the overall picture and panel (b) is a zoomed in view near the onset of instability of BS. Very near the first bifurcation from BS, the modal kinetic energy E_3 of the rotating wave RW_3 grows linearly with increasing Ro, and then slower than linearly with larger Ro, until $Ro \approx 0.298$ where RW_3 loses stability. Starting with the stable RW_3 at a slightly lower Ro as the initial condition for a slightly larger Ro results in an evolution to a rotating wave with $m = 2$, RW_2. The unstable RW_3 has also been continued to larger Ro by restricting the computations to the $m = 3$ symmetry subspace. The RW_2 solution branch was also continued to higher and lower Ro; it loses stability for $Ro \gtrsim 0.322$ and $Ro \lesssim 0.275$. At the low Ro end, RW_2 switches to an $m = 4$ branch, RW_4, which itself loses stability for $Ro \lesssim 0.267$, below which it switches to the RW_3 branch, and for $Ro \gtrsim 0.292$, the RW_4 branch loses stability. When the RW_2 branch loses stability for $Ro \gtrsim 0.322$, it switches to another rotating wave branch with $m = 1$, RW_1. This branch loses stability for $Ro \lesssim 0.275$, but remains stable for higher Ro at least up to the highest value considered in this study, $Ro = 0.40$.

The bifurcation scenario just presented is typical of an Eckhaus band [95]. Here, the marginal stability curve is a discrete set of points due to the integer wavenumber m resulting from breaking the azimuthal invariance, SO(2) symmetry, of BS, which gives the critical Ro for the instability of BS to a rotating wave with azimuthal wavenumber m. Only the rotating wave RW_m with the lowest critical Ro will be stable at its onset, in this case RW_3, and the rotating waves corresponding to other m will be unstable at their onset. However, these rotating waves become stable at secondary bifurcations and the local of points in (m, Ro) where these occur form the Eckhaus stability boundary. In principle, at a given Ro above critical, all rotating waves with m inside the Eckhaus band are stable, but can become unstable as Ro is increased,

and spawn unstable modulated rotating waves. Similar dynamics has been studied in rotating convection problems, where the Eckhaus instability for systems with SO(2) symmetry is further detailed [59, 63].

Figure 3.4 shows contours of the azimuthal vorticity, η, as well as its non-axisymmetric component, $\eta - \eta_0$, where η_0 is the $m = 0$ Fourier component of η, in the meridional plane $\theta = 0$ and the plane $z = -0.4$ which is close to the bottom endwall. The four rotating wave states shown in the figure are for $Re = 10^4$ and $Ro = 0.29$, and are inside the Eckhaus band where all four are stable. The boundary layer structure of the rotating wave states is very similar to that of the basic state (see figure 3.1), the main difference being a slight bulge in the lower corner region. This bulge is more readily appreciated when the axisymmetric component is removed; it is seen to be localized in the corner region and has azimuthal wavenumber m, as is evident from the plots in the $z = -0.4$ plane. This bulge structure rotates in the azimuthal direction at a constant rate without change of shape. In the corner region at any fixed point in a reference frame rotating with the cylinder mean rotation rate, the passage of the bulge provides a localized disturbance that emits a wave beam into the interior along a cone. This cone forms an angle β with a plane orthogonal to the cylinder axis given by the dispersion relation $\cos\beta = \omega_R/2$. The dispersion relation is obtained in the inviscid flow limit of infinitesimal perturbations to solid-body rotation [24], where ω_R is the frequency of the perturbation in the frame of reference rotating with the cylinder mean rotation rate Ω, and non-dimensionalized with Ω. When the localized disturbance is axisymmetric, the resulting wave beams are axisymmetric cones, but when the localized disturbance is not axisymmetric, the wave beams are spirals on the cone. The contours shown in the $z = -0.4$ plane in the third column of figure 3.4 illustrate the spiral nature of the wave beams, and the plots in the meridional plane in the second column of the figure show the cone structure.

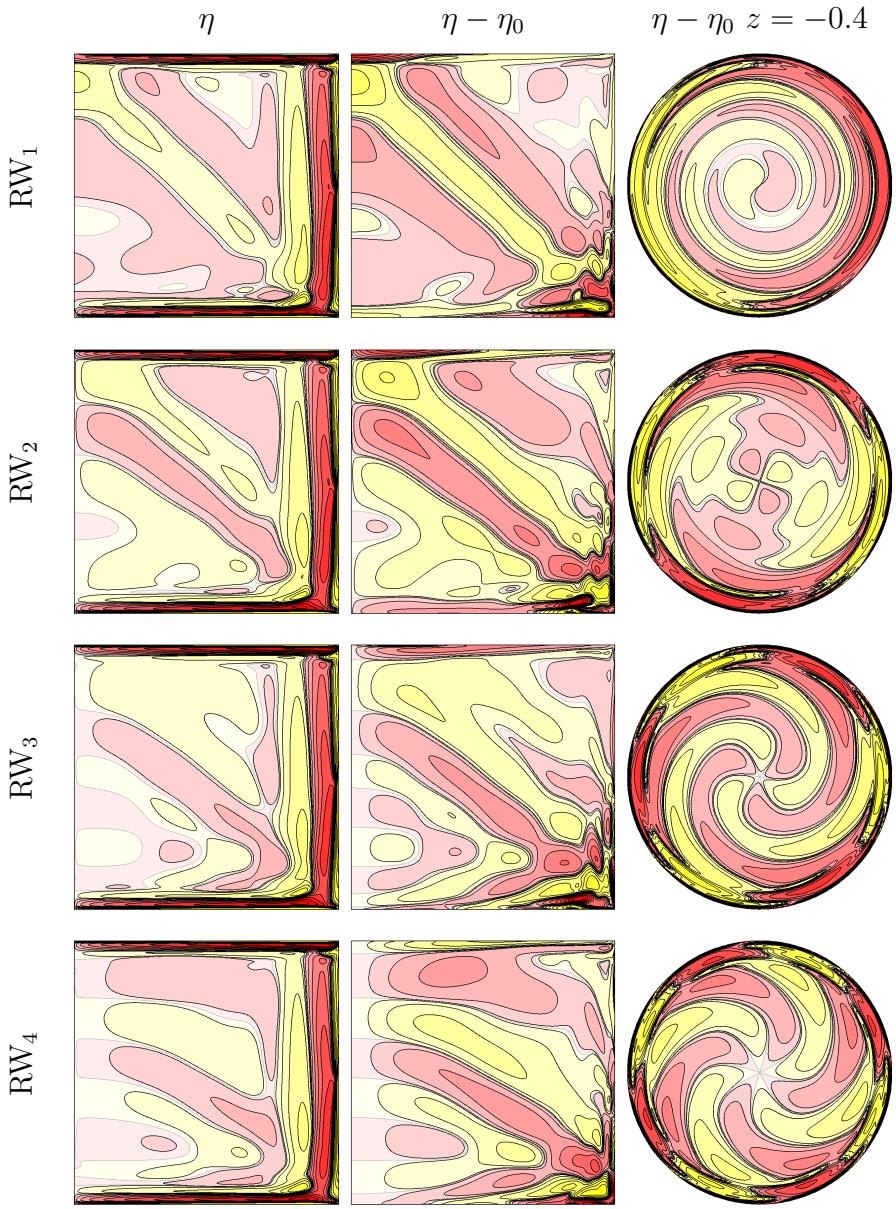


Figure 3.4: Contours of (a) η, (b) $\eta - \eta_0$ in the meridional plane $\theta = 0$, and (c) $\eta - \eta_0$ in the plane $z = -0.4$, for the rotating waves RW$_m$, $m \in [1, 4]$, at $Re = 10^4$, $Ro = 0.29$. There are ten cubically spaced contour levels in the ranges $\eta \in [-5, 5]$ and $\eta - \eta_0 \in [-1, 1]$, with the positive being red (dark gray) and the negative being yellow (light gray).

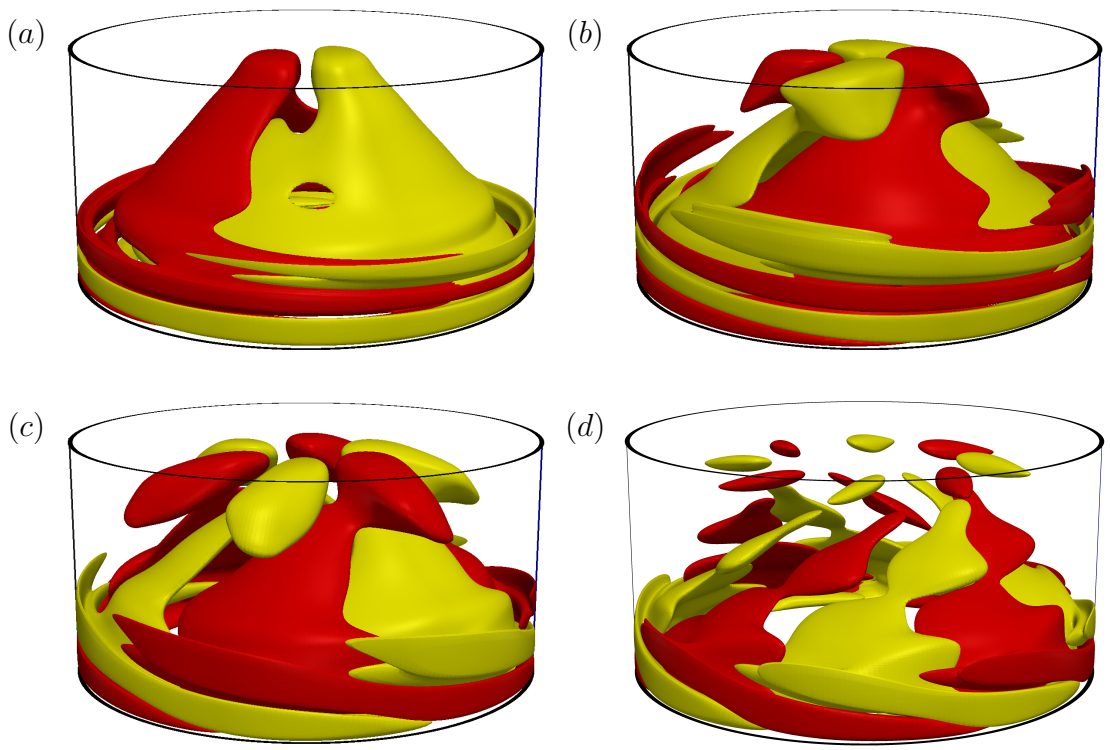


Figure 3.5: Isosurfaces of $w - w_0$, at levels ± 0.001, of (a) RW_1, (b) RW_2, (c) RW_3, and (d) RW_4 at $Re = 10^4$ and $Ro = 0.29$.

Figure 3.5 shows three-dimensional isosurfaces of the non-axisymmetric component of the axial velocity, $w - w_0$, for the four rotating wave states, illustrating the bulges localized near the corner (almost horizontal rollers that are more inclined for larger m), the resulting wave beams being emitted from the corner along the cone, and some reflections off either the top endwall or the axis, depending on the cone angle for each case. Since our simulations are conducted in the stationary frame of reference, to predict the cone angle we need to convert the precession frequency of the rotating wave in the stationary frame ω_S (which is obtained directly from our simulations) to ω_R, the frequency a local observer sees in the rotating frame of reference. Recall that a structure with azimuthal wavenumber m takes $2\pi m/\omega_S$ time units to rotate

	ω_S	ω_R	β
RW_1	-0.47	-1.47	$42.63°$
RW_2	0.39	-1.61	$36.18°$
RW_3	1.35	-1.65	$34.38°$
RW_4	2.22	-1.78	$27.11°$
LC	1.68	1.68	$32.86°$

Table 3.1: Frequencies in the stationary and rotating frames of reference and angles of the inertial wave beam cones for different stable RW states and the unstable LC, all at $Re = 10^4$ and $Ro = 0.29$.

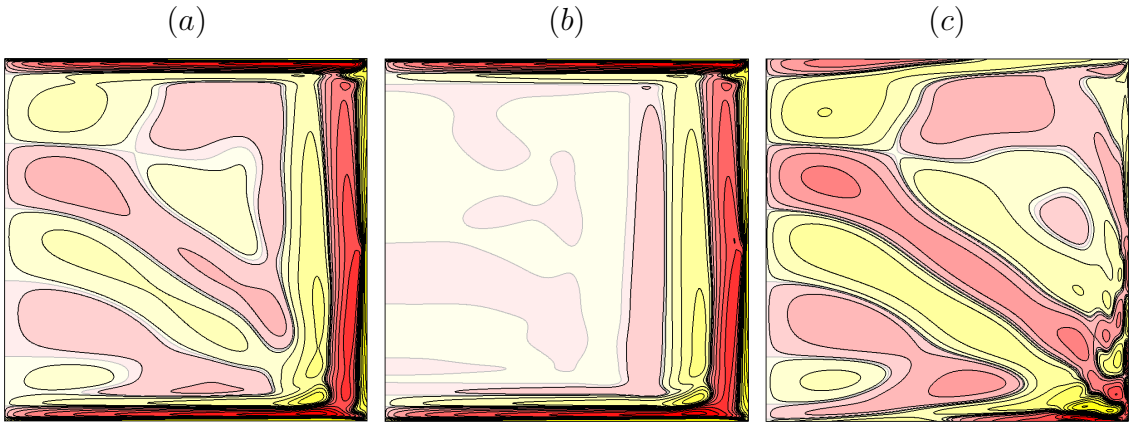


Figure 3.6: Contours of (a) η, (b) $\langle\eta\rangle$ and (c) $\eta - \langle\eta\rangle$ in a vertical plane for the unstable LC solution at $Re = 10^4$, $Ro = 0.29$. There are ten contour levels in the range $\eta \in [-5, 5]$, $\langle\eta\rangle \in [-5, 5]$ and $\eta - \langle\eta\rangle \in [-1, 1]$, cubically spaced, with the positive being red (dark gray) and the negative being yellow (light gray).

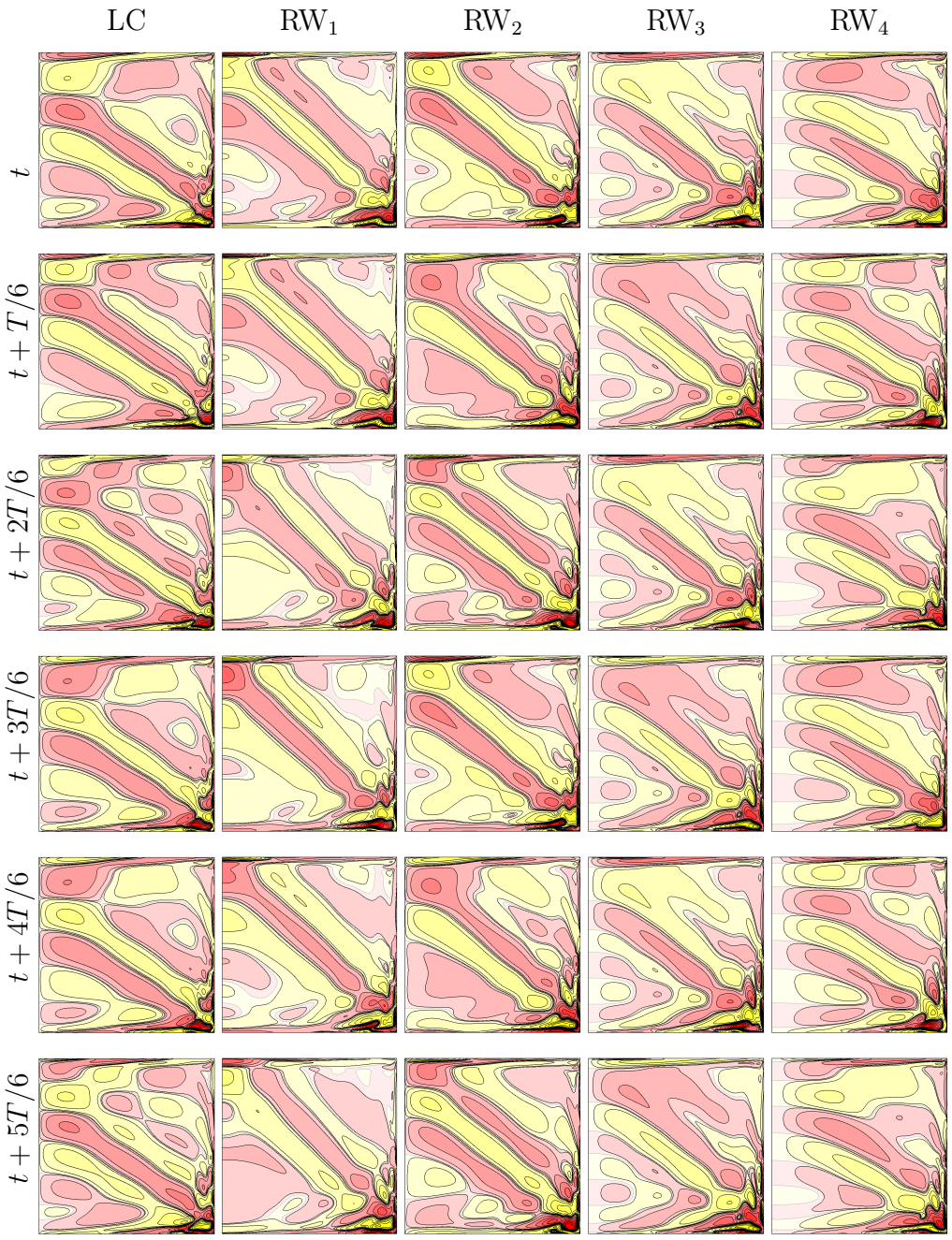


Figure 3.7: Contours of $\eta - \langle\eta\rangle \in [-1, 1]$ for the unstable LC and $\eta - \eta_0$ for the stable RW_1, RW_2, RW_3 and RW_4 in a meridional plane $\theta = 0$ at $Re = 10^4$and $Ro = 0.29$; snap-shots at six equally spaced phases over their respective periods are shown.

2π in the stationary frame of reference. To calculate the frequency in the rotating frame of reference, the background rotation speed (non-dimensionalized to 1) has to be subtracted from the angular speed of the rotating wave (ω_S/m) to obtain the angular speed of the rotating wave in the rotating frame of reference (ω_R/m), leading to $\omega_R = \omega_S - m$. Table 3.1 lists ω_S, ω_R and the corresponding cone angle β for the four rotating waves shown in figures 3.4 and 3.5. The linear inviscid dispersion relation does a very good job of predicting the cone angle β, even though the simulations are quite viscous, with $Re = 10^4$, and highly nonlinear with $Ro = 0.29$. In the stationary frame of reference, the precession rates of the rotating waves vary considerably, with RW_1 precessing retrograde with respect to the sense of mean rotation of the cylinder (hence the negative frequency), and the other three are prograde. However, when viewed in the rotating frame, all are retrograde with much smaller variation in frequencies. For the lowest $m = 1$, the cone angle is such that the wave beam almost perfectly retraces itself as it is emitted from the corner region $(r, z) = (1, -0.5)$ and is reflected back from the axis at the top endwall $(r, z) = (0, 0.5)$. For increasing m, the wave beams do not penetrate all the way to the axis; for RW_4, there is a clear quiescent zone near the axis. This is consistent with the analysis of Wood [102], who showed that the radial extent of the quiescent axial zone increases with m.

It is of interest to compare the rotating wave states with the axisymmetric limit cycle that bifurcates from the basic state, that was first described in Gutierrez-Castillo and Lopez [25]. We again fix $Re = 10^4$ and increase Ro, but compute in the axisymmetric subspace, since BS is first unstable to non-axisymmetric disturbances. Doing so, BS becomes unstable via a Hopf bifurcation at $Ro \approx 0.28$, spawning an axisymmetric limit cycle LC, which like BS in this parameter regime is unstable to non-axisymmetric perturbations. Figure 4.29(a) shows a snap-shot of the azimuthal vorticity η of LC at $Ro = 0.29$. Its time average, $\langle\eta\rangle$, shown in figure 4.29(b) is very

similar in structure to BS, as is to be expected near the Hopf bifurcation. What is particularly of interest is the structure of the Hopf mode, which can be approximated by $\eta - \langle\eta\rangle$ and compared directly with the Hopf modes associated with the rotating waves, that are approximated by $\eta - \eta_0$. Figure 4.29(c) shows $\eta - \langle\eta\rangle$ of LC and it is clear that is has very similar structure to $\eta - \eta_0$ of the rotating waves, shown in the second column of figure 3.4. The corner region where the sidewall and lower endwall meet is the center of localized unsteadiness. For LC, the pulsing in the corner is axisymmetric and an axisymmetric wave beam is emitted into the bulk. As LC is axisymmetric, the frequency of oscillation is the same in the stationary frame and in any rotating frame (reported in last line of table 3.1).

To make the connection between the limit cycle and rotating waves more succinct, figure 3.7 shows snapshots at six equally-spaced phases in one period of $\eta - \langle\eta\rangle$ for LC and $\eta - \eta_0$ for RW_1, RW_2, RW_3 and RW_4; the period for each case is different, as indicated by their frequencies, reported in table 3.1. Looking at a given meridional plane over time, it is difficult to distinguish between the LC and RW cases (except perhaps for the RW with larger m due to the small quiescent axial zone). This type of duality between limit cycles and rotating waves in axisymmetric systems has been examined previously, such as in Lopez [47], Lopez and Marques [51], Marques *et al.* [64].

Now, we fix $Ro = 0.28$ (RW_1, RW_2, RW_3 and RW_4 are all stable for $Re = 10^4$ at this Ro), and consider a one-parameter sweep increasing Re from a smaller value where BS is stable. At $Re \approx 9.2 \times 10^3$, BS loses stability in a supercritical Hopf bifurcation, and RW_2 emerges. Figure 3.8(a) shows how the modal energies E_0 and E_2 vary with Re. RW_2 remains stable until $Re \approx 1.1 \times 10^4$, at which point it undergoes a secondary Hopf bifurcation, spawning a quasiperiodic (QP) state, the details of which are discussed later, in section 3.4.5. We already know that RW_1, RW_3 and RW_4 are also

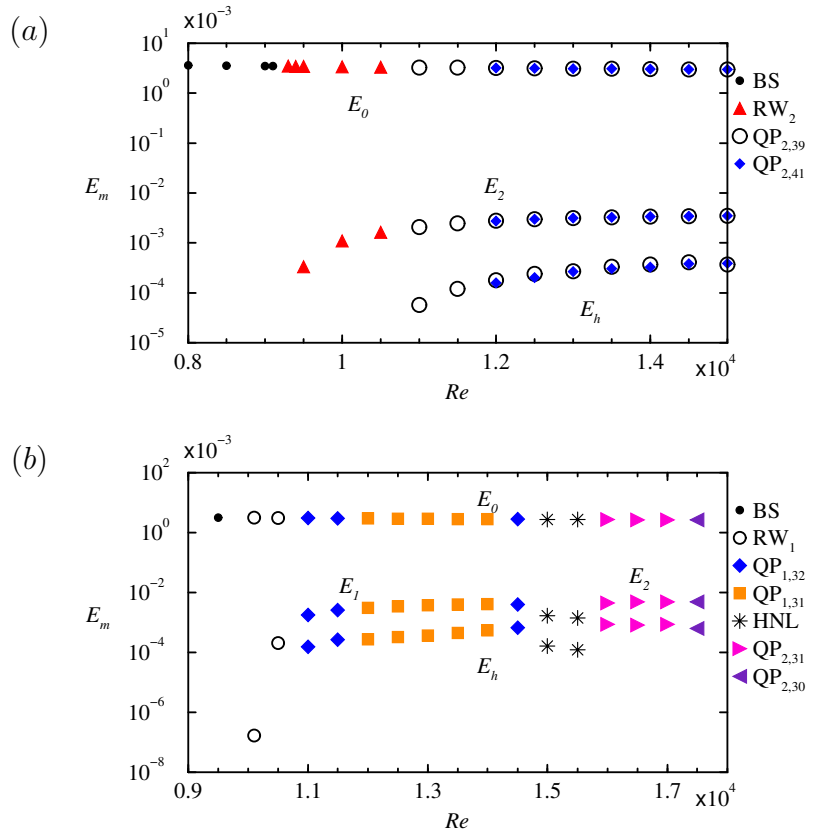


Figure 3.8: Variation of principle modal kinetic energies for various states with increasing Re for (a) $Ro = 0.28$ and (b) $Ro = 0.27$; E_h corresponds to the modal kinetic energy for the high azimuthal wavenumber component of the various QP states.

stable in the neighborhood of $Re \sim 10^4$ for this Ro, but the fate of these rotating waves has not been pursued any further. The point we wish to make here is that RW_2 is the state that is selected in this one-parameter sweep and that there is no obvious reason for its selection — for example, figure 3.3(b) shows that at $(Re, Ro) = (10^4, 0.28)$, RW_2 is not the most energetic of the four rotating waves. Repeating the one-parameter sweep, but with $Ro = 0.27$, we find similar behavior, but with RW_1 being spawned from BS in a supercritical Hopf bifurcation at $Re \approx 1.01 \times 10^4$, and then undergoing a secondary Hopf bifurcation to a QP state at $Re \approx 1.08 \times 10^4$ (see figure 3.8b). It

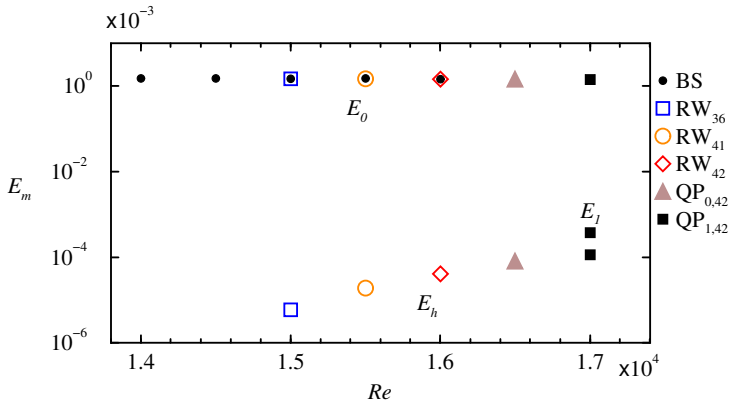


Figure 3.9: Variation of principle modal kinetic energies for various states with increasing Re for $Ro = 0.20$; E_h corresponds to the modal kinetic energy for the high azimuthal wavenumber component of the various states.

should be noted that figure 3.3(b) shows that at $(Re, Ro) = (10^4, 0.27)$, RW_3 and RW_4 are the only rotating waves that have bifurcated from BS and are stable, and yet the one-parameter sweep performed selected RW_1 at Re slightly above 10^4. Similar behavior is found for the one-parameter sweep with $Ro = 0.26$.

In order to get insight into the nature of the QP states that result from secondary Hopf bifurcations from RW states as Re is increased, it is convenient to first examine the rotating wave states at lower Ro, which have much higher azimuthal wavenumbers than the rotating waves RW_L examined so far. As a group, the high-m rotating waves are designed as RW_H (individually, H is replaced with the corresponding m). The QP states will be shown to be mixed-modes of RW_L and RW_H.

3.4.4 High Azimuthal Wavenumber Rotating Waves

Figure 3.2 indicates that RW_H are found at the low end of the Ro range considered. Fixing $Ro = 0.20$ and conducting a one-parameter sweep with increasing Re, we find that BS is stable up to $Re \approx 1.6 \times 10^4$. A further small increase in Re results in a

jump to a QP state. Continuation from the QP state to lower Re reveals a series of rotating waves with high azimuthal wavenumbers. This is a clear indication that BS at $Ro = 0.20$ loses stability in a subcritical bifurcation. Figure 3.9 shows the modal kinetic energies of the states encountered in this one-parameter sweep. The RW_H found have $m = 36$, 41, and 42 with increasing Re; one was obtained from the other as initial condition going from higher to lower Re. The transients involved are very slow (on the order of a viscous time or longer), as is typically found when undertaking one-parameter paths within an Eckhaus band of states [59]. This together with the cost of following multiple rotating wave branches with a large range of high azimuthal wavenumbers makes a detailed study prohibitive.

A typical example of a high azimuthal wavenumber rotating wave is RW_{41} at $Ro = 0.20$ and $Re = 1.55 \times 10^4$; figure 3.10 shows contours of η in a meridional plane, and of $\eta - \eta_0$ in a meridional plane and in the plane $z = -0.4$. Since the modal kinetic energy E_{41} is five orders of magnitude smaller then E_0, the η contours of RW_{41} (figure 3.10*a*) are virtually indistinguishable from those of BS (not shown) at the same point in parameter space, where both are stable. The contours of $\eta - \eta_0$ however, show that the perturbation of RW_{41} away from BS is localized in the bottom half of the sidewall boundary layer and concentrated in the lower corner region, much as is the case for the RW_L. The three-dimensional isocontours of $w - w_0$ for RW_{41} (figure 3.10*d*) show a clear distinction from the $w - w_0$ isocontours of RW_L. Apart from the large difference in azimuthal wavenumber m, for RW_L, the low-m spirals very near the corner have a small negative helix angle, whereas the perturbation structures of RW_{41} have a large positive helix angle. Another distinction between the two classes of rotating waves is that all the RW_L emitted inertial wave beams into the interior, whereas no wave beams are evident for RW_{41}. In the stationary frame of reference, the $m = 41$ rotating wave structure has a very fast frequency $\omega_S = 39.47$; this is two

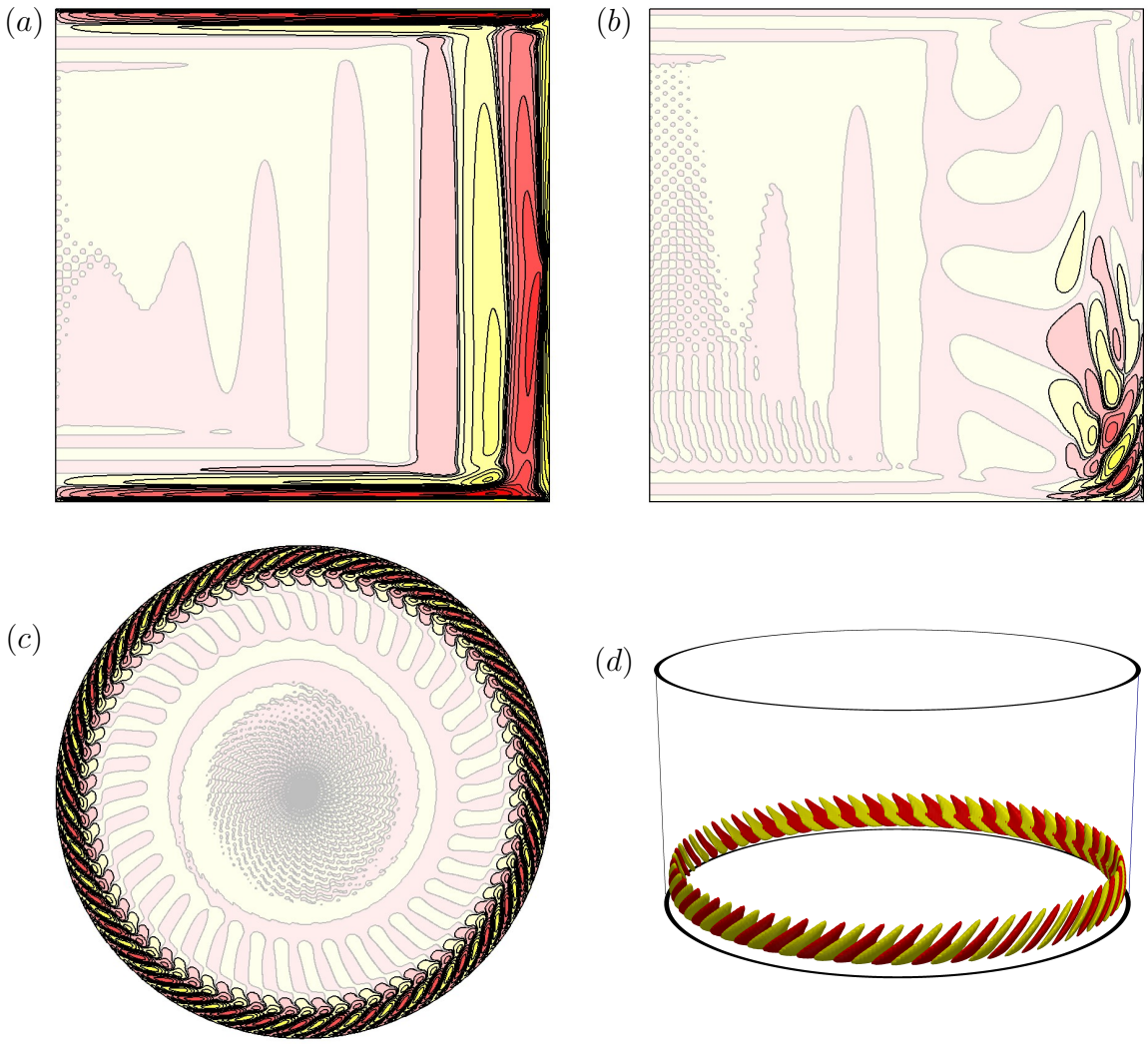


Figure 3.10: Contours of (a) η and (b) $\eta - \eta_0$ at $\theta = 0$, (c) $\eta - \eta_0$ at $z = -0.4$, and (d) isosurfaces of $w - w_0$, at levels and ± 0.001, for RW_{41} at $Re = 1.55 \times 10^4$ and $Ro = 0.20$. There are ten cubically spaced contour levels in the range $\eta \in [-5, 5]$ and $\eta - \eta_0 \in [-1, 1]$.

orders of magnitude faster than that of the RW_L. However, in the frame of reference rotating at the mean rotation rate of the cylinder, RW_{41} has $\omega_R = -1.53$, which is in the middle of the range of ω_R for the RW_L, suggesting that inertial wave beams at an angle of approximately 40° should be emitted from the corner region, but these are not evident. This is likely a result of the enlargement of the quiescent axial zone for the much larger azimuthal wavenumber $m = 41$ [102], and perhaps the larger m structures are also subjected to more viscous dissipation as their spatial gradients are larger [11, 61]. Also, it should be noted that the relative strength of RW_{41}, E_{41}/E_0, is about two orders of magnitude smaller than that of the RW_L, and this also contributes to the muting of any associated inertial wave beams. The other RW_H found in the low-Ro regime are similar to RW_{41}.

3.4.5 Quasiperiodic Mixed-modes

The parameter regime where rotating waves RW_L and RW_H are found is quite small, and most of the regime diagram (figure 3.2) where BS is unstable is dominated by quasiperiodic states. Near where rotating waves exist, the QP states are seen to emerge following secondary bifurcations from the rotating waves. The QP states have oscillations associated with two distinct azimuthal wavenumbers that correspond to RW_H and RW_L (and in some cases to $m = 0$ from LC). It is tempting to think of this as resulting from a double-Hopf bifurcation where at a codimension-2 point (i.e. a single point in (Re, Ro) parameter space), a RW_L and a RW_H bifurcate simultaneously from BS, and in some neighborhood of the codimension-2 point there is a mixed-mode $\mathrm{QP}_{L,H}$. This type of scenario has been observed in other differentially rotating cylinder systems [50, 62, 64], but in the present problem the situation is much more complicated, primarily due to the RW_L and RW_H coming in Eckhaus bands, as well as due to the subcritical nature of the instability of BS at the lower end of the Ro range.

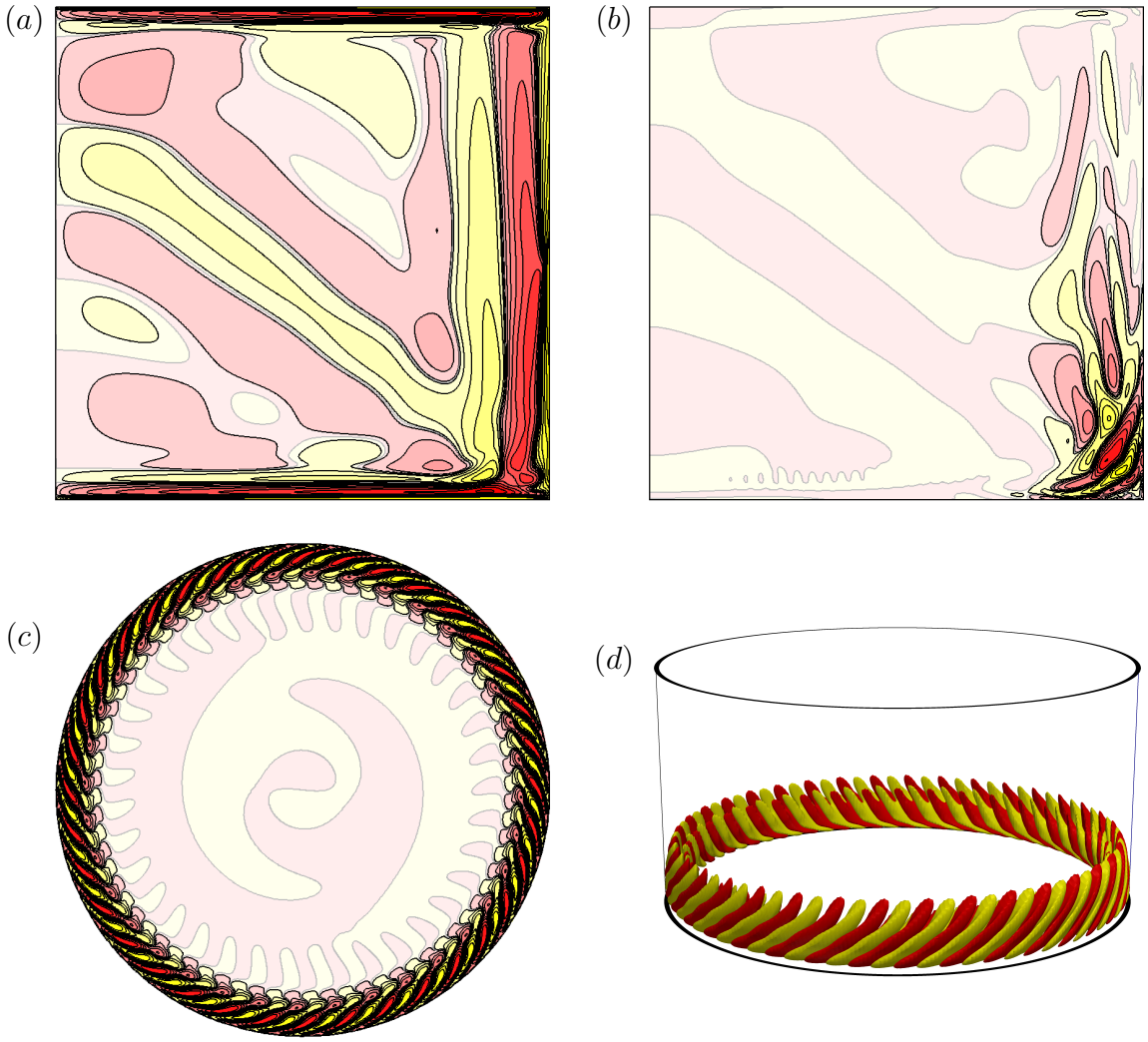


Figure 3.11: Contours of (a) η and (b, c) $\eta - \eta_0$ at $\theta = 0$, (c) $\eta - \eta_0$ at $z = -0.4$, and (d) isosurfaces of $w - w_0$, at levels and ± 0.001, for $\mathrm{QP}_{0,36}$ at $Re = 1.35 \times 10^4$, $Ro = 0.23$. There are ten cubically spaced contour levels in the range $\eta \in [-5, 5]$ and $\eta - \eta_0 \in [-1, 1]$.

Figure 3.11 presents an example of a mixed-mode $\mathrm{QP}_{0,36}$, showing contours of η and $\eta - \eta_0$ in different planes, and isosurfaces of $w - w_0$. $\mathrm{QP}_{0,36}$ is a mixed-mode with contributions from LC that drives inertial wave beams and RW_{36} which does not. Contours of η in a meridional plane (figure 3.11a) clearly show the inertial waves, and are very similar to the η contours of the pure LC shown in figure 4.29. Removing the axisymmetric component, the contours of $\eta - \eta_0$ shown in figures 3.11(b, c) and the isosurfaces of $w - w_0$ shown in figure 3.11(d) are very similar to those of a pure RW_H, such as those of RW_{41} shown in figure 3.10.

Figure 3.12 is an example of a mixed-mode $\mathrm{QP}_{2,39}$. In this case, there is a mix of RW_2 and RW_{39}. The contours of η shown in figure 3.12(a) are very similar to those of $\mathrm{QP}_{0,36}$ in figure 3.11(a), however, subtracting off the axisymmetric component ($\eta - \eta_0$ shown in figures 3.12b and c) does not remove the inertial wave beams as it did for $\mathrm{QP}_{0,36}$, as they are driven by the $m = 2$ component of $\mathrm{QP}_{2,39}$. This is further illustrated by the three-dimensional isosurfaces of the axial velocity. Figure 3.12(d) shows isosurfaces of the full solution minus its axisymmetric component, $w - w_0$, and is rather complicated. However, plotting only the $m = 2$ component of w, w_2 in figure 3.12(e) and only the $m = 39$ component, w_{39} in figure 3.12(f) clearly shows that $\mathrm{QP}_{2,39}$ is indeed a mixed-mode of RW_2 and RW_{39}; compare these isosurfaces with those of RW_2 in figure 3.5(b) and RW_{41} in figure 3.10(d). The quantitative differences between the low and high azimuthal wavenumber components of the QP and the corresponding RW_L, or LC, and RW_H are due primarily to the different points in (Re, Ro) parameter space where the comparisons are made.

To obtain the frequencies associated to the QP states, we follow the procedure used for RW_L and RW_H. The fast Fourier transform of the time-series of w at a point close to the bottom corner of the cylinder provides a temporal spectrum of the flow in the stationary frame of reference, ω_S, which for a quasiperiodic flow

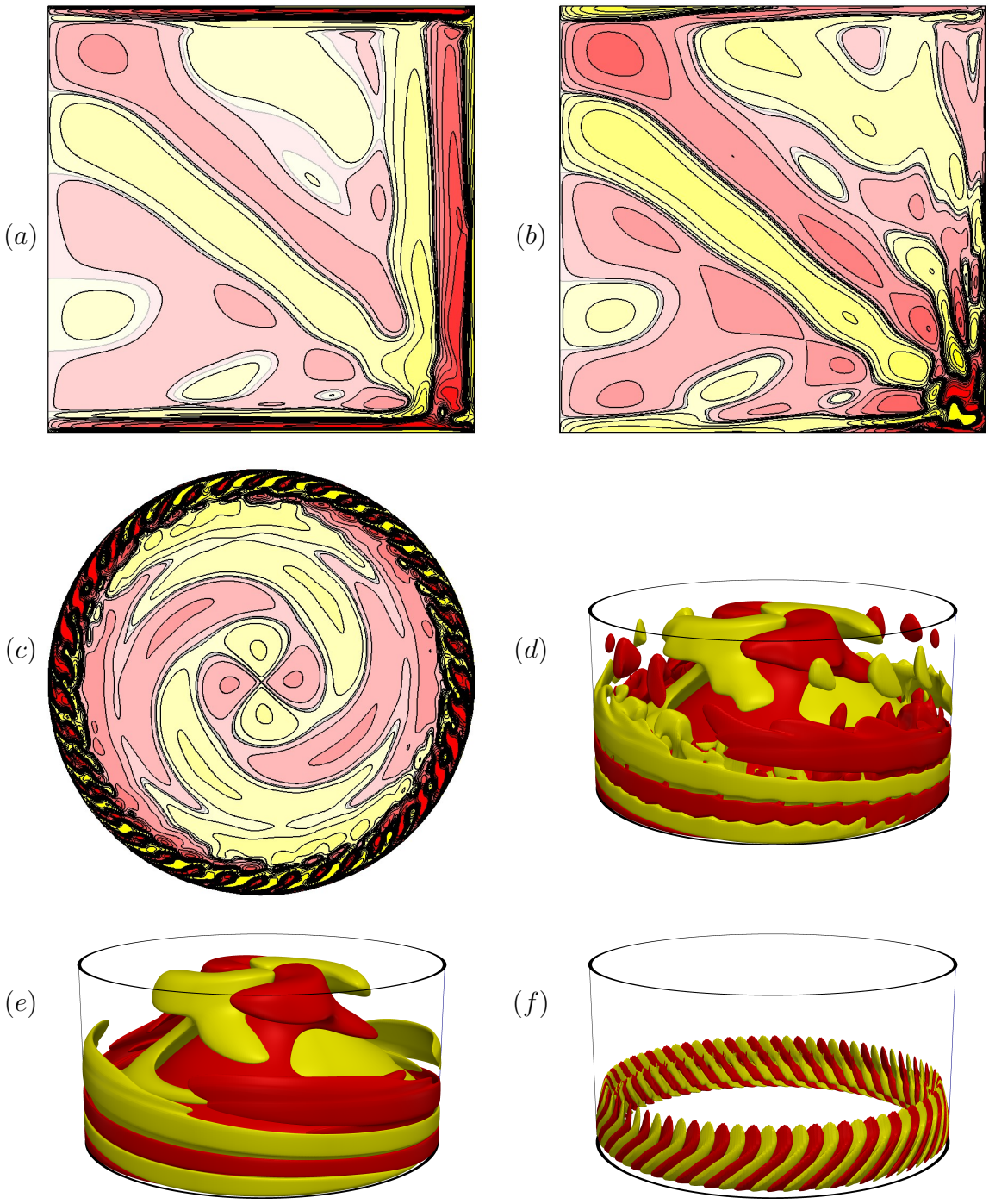


Figure 3.12: Contours of (a) η, (b,c) $\eta - \eta_0$, and isosurfaces of (d) $w - w_0$, (e) w_2 and (f) w_{39} for $\mathrm{QP}_{2,39}$ at $Re = 1.50 \times 10^4$ and $Ro = 0.28$. There are ten cubically spaced contour levels in the range $\eta \in [-5, 5]$ and $\eta - \eta_0 \in [-1, 1]$, and the isosurfaces are at ± 0.001.

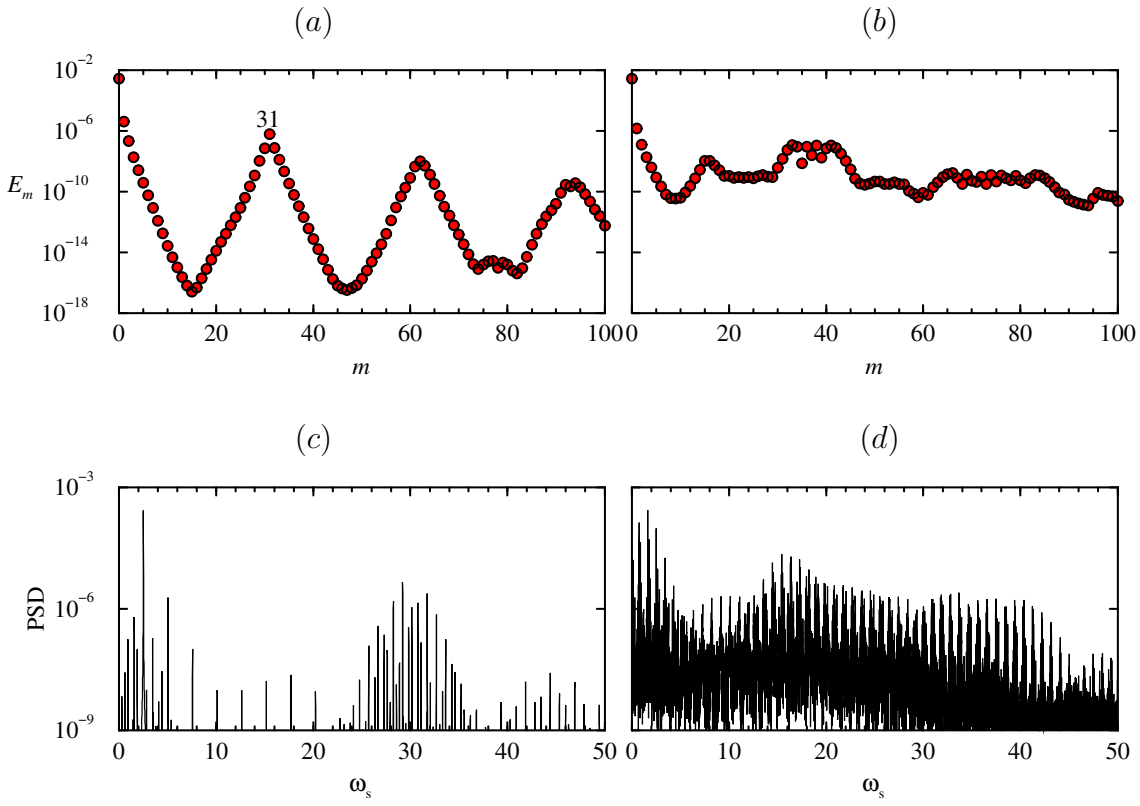


Figure 3.13: Azimuthal (E_m mean modal kinetic energies) and temporal (PSD of w at $(r, \theta, z) = (0.98, 0, -0.4)$) spectra for (a, c) $\mathrm{QP}_{1,31}$ at $Re = 1.40 \times 10^4$, (b, d) HNL at $Re = 1.55 \times 10^4$, both cases at $Ro = 0.27$.

consists of two frequencies and all their linear combinations. These two frequencies are associated with either the RW_L or LC and the RW_H components of which QP is comprised. To calculate the corresponding frequencies in the rotating frame of reference, ω_R, two intermediate steps are needed. First, we produce a movie of the low and high m components of QP independently, with a very high time resolution over a short time interval, to determine if they are retrograde or prograde with the mean cylinder rotation in the stationary frame of reference; if it is prograde (retrograde) the associated frequency is positive (negative). Such movies are also useful for verifying

which frequency is associate with the low and high m components. Then, to determine the frequency of the low and high m components of QP in the rotating frame of reference, m is subtracted from the corresponding frequency in the stationary frame of reference.

Figure 3.13(a) shows the modal kinetic energy for each azimuthal wavenumber m in a $\mathrm{QP}_{1,31}$ state for which two peaks at $m = 1$ and $m = 31$ are evident (the peak at $m = 0$ corresponding to the mean flow is always dominant). Figure 3.13(c) shows the corresponding temporal spectrum of that state, determined from the time-series of w at $(r, \theta, z) = (0.98, 0, -0.4)$. It also consists of two peaks and all their linear combinations; these are at $\omega_S = 2.53$ associated with the $m = 1$ component of $\mathrm{QP}_{1,31}$ (verified to be prograde) and $\omega_S = 29.20$ associated with the $m = 31$ component of $\mathrm{QP}_{1,31}$ (also prograde). The two frequencies associated with $\mathrm{QP}_{1,31}$ in the rotating frame of reference are $\omega_R = 1.53$ and $\omega_R = -1.80$ respectively.

On the other hand, some of the QP states have spatial and temporal spectra that are broad-band, and they are not straightforward to decompose into simple mixed-modes as done above. Such cases are termed highly nonlinear HNL. The spatial and temporal broad-band spectra of a HNL at $Re = 1.55 \times 10^4$ and $Ro = 0.27$ are shown in figures 3.13(b, d). This HNL is found between two different QP, $\mathrm{QP}_{1,31}$ and $\mathrm{QP}_{2,32}$, as Re is increased with $Ro = 0.27$ fixed (see figure 3.8b). Figure 3.14 shows η and $\eta - \eta_0$ contours and isocontours of $w - w_0$ of this HNL. The meridional plots are similar to those of the various QP states previously described. The contours of $\eta - \eta_0$ at $z = -0.4$ show a strong $m = 1$ modulation of the high-m wall structure; this can be interpreted as coming from both the $m = 1$ component of $\mathrm{QP}_{1,31}$ and the nonlinear interaction between the $m = 31$ component of $\mathrm{QP}_{1,31}$ and the $m = 32$ component of $\mathrm{QP}_{2,32}$. The wave beam in this HNL seems to be driven by the $m = 1$ component of HNL. The wave beam cone is clearly identified in the $w - w_0$ isosurfaces

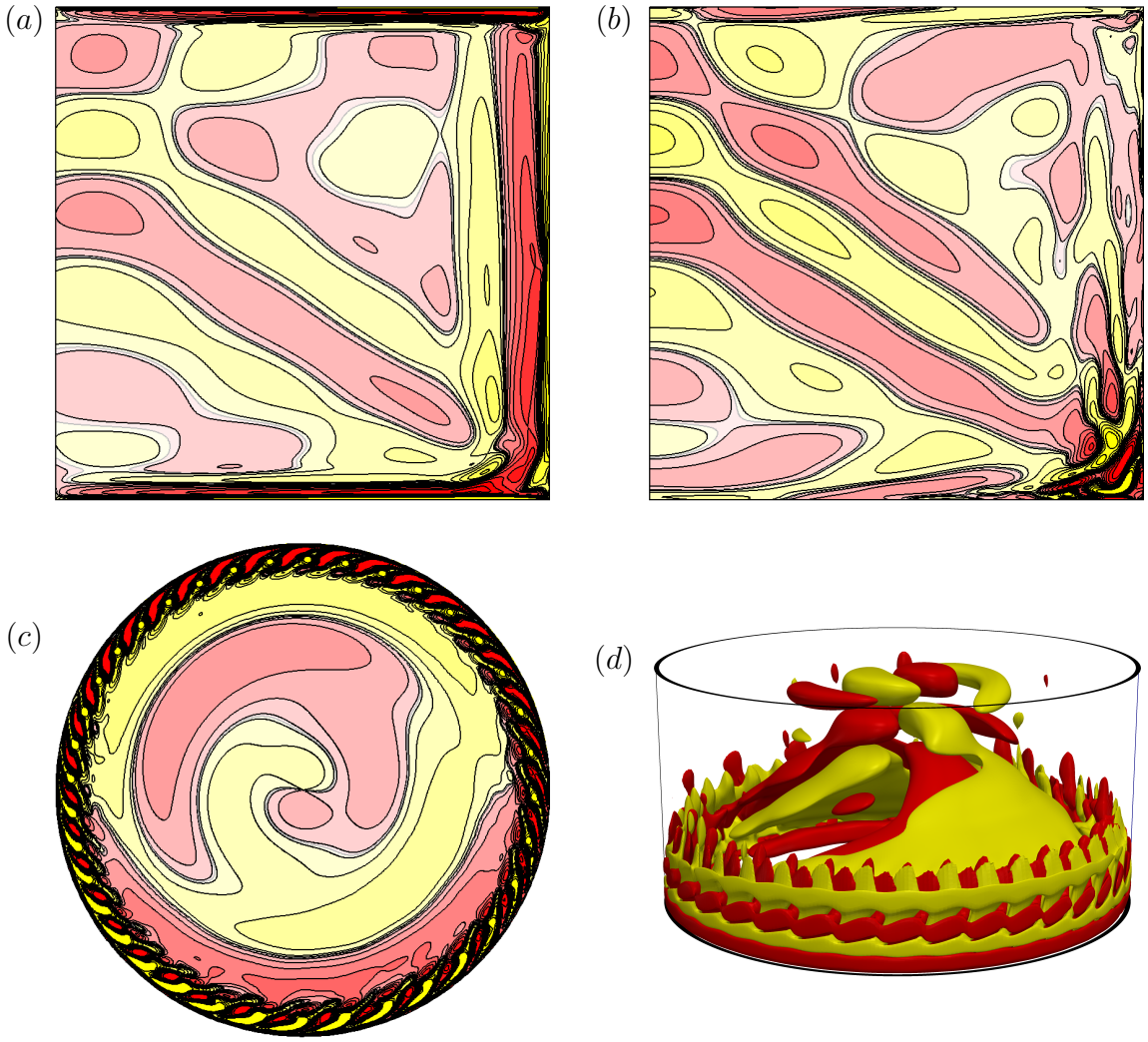


Figure 3.14: Contours of (a) η and (b,c) $\eta - \eta_0$ at $\theta = 0$, (c) $\eta - \eta_0$ at $z = -0.4$, and (d) isosurfaces of $w - w_0$ at levels and ± 0.001, for HNL at $Re = 1.55 \times 10^4$, $Ro = 0.27$. There are ten cubically spaced contour levels in the range $\eta \in [-5, 5]$ and $\eta - \eta_0 \in [-1, 1]$.

(figure 3.14*d*), but the $m = 1$ wave beam is not as clean as it is for RW_1 (figure 3.5*a*). This is mainly due to the broad-band nature of its temporal spectrum. The HNL were found to persist for long times in parameter regimes separating some QP states with differing primary azimuthal wavenumbers.

3.5 Discussion and Conclusions

The nonlinear dynamics of the flow in a rapidly rotating split-cylinder has been investigated numerically for moderate differential rotations between the top and bottom halves of the cylinder, Ro. The flow becomes unstable to a variety of three-dimensional instabilities localized in the bottom half of the sidewall boundary layer and the corner where the sidewall and bottom endwall meet. For stronger differential rotation, the instability modes are low azimuthal wavenumber rotating waves, RW_L, consisting of spiral vortex structures of alternating sign that are roughly aligned with the mean flow direction in the bottom corner. Their structure and flow alignment is suggestive of a centrifugal instability as they are akin to Görtler vortices [87], but it is difficult to estimate a Görtler number as the flow curvature and speed are not uniform in this region. Perhaps these non-uniformities are partially responsible for the multiplicity of such states that co-exist stably in this parameter regime. The multiplicity of RW_L come about supercritically in a fashion typical of Eckhaus bands [95].

At smaller Ro and larger Re, the flow is also unstable to rotating waves, RW_H, but these have high azimuthal wavenumbers that are an order of magnitude larger than those of RW_L, and their onset is subcritical so that there is a large hysteretic region of parameter space where both the basic state and RW_H are stable. Their instability modes consist of a large ($m \sim 40$) number of pairs of counter-rotating vortical structures that are aligned orthogonally to the mean flow direction in the corner region. Their structure and flow alignment is suggestive of Tollmien–Schlichting

waves [89] in the sidewall and corner region closest to the wall, but again the analogy is only qualitative due to the non-uniformity of the boundary layer shear flow near the corner.

For a large range of *Ro* and *Re* in between where RW_L and RW_H are found, the flow is quasiperiodic, QP, consisting of states displaying a mix of the characteristics of both RW_L and RW_H. As *Ro* and *Re* are varied in this regime, either the high or low azimuthal wavenumbers of QP shift around (somewhat reminiscent of crossing Eckhaus boundaries) and some highly nonlinear states, HNL, that have broadband spectrum in both space and time, are found to persist for long times (order of a viscous time), however, they still retain the broader characteristics of being mixed-modes of various RW_L and RW_H.

The rotating waves are three-dimensional structures that do not change but simply drift in the azimuthal direction. Viewing this drift from a frame of reference that is rotating at the mean rotation rate of the split cylinder gives a frequency of the rotating wave. For all RW_L and RW_H, this frequency is seen to be in a relatively tight range of about 1.45 to 1.8 times the mean rotation frequency of the cylinder. From a linear inviscid analysis of periodic perturbations to solid-body rotation [24], such perturbation frequencies from a localized disturbance (the bottom corner region in the split-cylinder flow) would emit inertial wave beams at angles in the range 26°–44°. For the aspect ratio $\gamma = 1$ of the cylinder under consideration, this means that the inertial wave beams (approximately) retrace themselves from the bottom corner to and from the top of the cylinder axis. This was also true of the wave beams that resulted when the flow was numerically restricted to being axisymmetric, and in those cases Gutierrez-Castillo and Lopez [25] also investigated variation in γ and found that the Hopf bifurcations leading to periodic states had the Hopf frequency varying with γ such that the resultant wave beams would continue to approximately retrace themselves

from the bottom corner to top of the axis in a primary bifurcation. This seems to be a fairly general phenomenon when wave beams are the result of an instability rather than due to an extraneously imposed periodic forcing. Analogous frequency selections leading to approximately retracing wave beams have been more extensively studied in stratified flows [57, 70, 94], which are well-known to have analogous wave properties to rotating flows, with buoyancy providing the restoring force instead of Coriolis [97].

Acknowledgements

This work was supported by the U.S. National Science Foundation grant CBET-1336410.

Chapter 4

THREE-DIMENSIONAL INSTABILITIES AND INERTIAL WAVES IN A RAPIDLY ROTATING SPLIT-CYLINDER FLOW

4.1 Abstract

The flow in a split cylinder with each half in exact counter rotation is studied numerically. The exact counter rotation, quantified by a Reynolds number Re based on the rotation rate and radius, imparts the system with an O(2) symmetry (invariance to azimuthal rotations as well as to an involution consisting of a reflection about the mid-plane composed with a reflection about any meridional plane). The O(2) symmetric basic state is dominated by a shear layer at the mid-plane separating the two counter-rotating bodies of fluid, created by the opposite-signed vortex lines emanating from the two endwalls being bent to meet at the split in the sidewall. With the exact counter rotation, the additional involution symmetry allows for steady non-axisymmetric states, that exist as a group orbit. Different members of the group simply correspond to different azimuthal orientations of the same flow structure. Steady states with azimuthal wavenumber m (the value of m depending on the cylinder aspect ratio Γ) are the primary modes of instability as Re and Γ are varied. Mode competition between different steady states ensues, and further bifurcations lead to a variety of different time-dependent states, including rotating waves, direction reversing waves, as well as a number of slow-fast pulse waves with a variety of spatio-temporal symmetries. Further from the primary instabilities, the competition between the vortex lines from each half cylinder settles on either a $m = 2$ steady state or a limit cycle state with a half-period-flip spatio-temporal symmetry. By computing in symmetric subspaces as

well as in the full space, we are able to unravel many details of the dynamics involved.

4.2 Introduction

Flows driven between differentially rotating disks have a long history due to their relevance to many processes in nature and technology, as well as being of fundamental interest [4, 42, 46, 85, 91, 103]. The fundamental issue concerning the nature of the bulk flow between differentially rotating disks depends critically on the lateral conditions at large radii, and for enclosed systems, the sidewall boundary condition plays a major role in determining the bulk flow, due to the induced meridional flow. For the most part, these types of flows have been studied in cylindrical containers, and when the differential rotation is sufficiently strong, the axisymmetry of the flow is broken leading to rotating waves, modulated rotating waves and other spatio-temporally complicated states [5, 6, 21, 47, 50, 52, 62, 68].

The case when the two endwalls (disks) are exactly in counter rotation and the sidewall is stationary, the so-called von Kármán swirling flow, is special as the system is more than just axisymmetric (invariance to rotations about the axis, SO(2) symmetry), it is also invariant to a Z_2 symmetry (involution). This involution is a combination of a reflection through any meridional plane composed with a reflection about the mid-plane [74, 75, 77], and is equivalent to a rotation of π about an axis through the center of the cylinder that is orthogonal to the cylinder axis. This involution does not commute with the rotation, and together these symmetries form an O(2) symmetry group. In general, differentially rotating cylinder flows only have SO(2) symmetry, and it is well established that flows with O(2) symmetry can have fundamentally different behavior to flows with SO(2) symmetry [13, 36]. In particular, when axisymmetry is broken in an SO(2) system, rotating waves result, whereas in O(2) systems, steady three-dimensional states can result.

The flow in a cylinder with exactly counter-rotating endwalls and a stationary sidewall, the von Kármán swirling flow, has attracted much attention as a possible laboratory scale dynamo. The motivation comes from the torsional forcing of the counter-rotating endwalls providing a global scale dynamo action. However, the stationary sidewall imparts significant viscous drag, substantially reducing the effectiveness of the counter-rotating endwalls driving a torsional flow. Experimentally, the flat endwalls are replaced by impellers to counteract the sidewall effects [8, 14, 18, 22, 69, 82, 83]. The O(2) symmetry of the problem leads to interesting dynamics when it is broken, resulting from mode interactions which have strong spatial resonances. Nore *et al.* [75] studied the competition between states with azimuthal wavenumbers $m = 1$ and 2. Such 1:2 resonances have drawn considerable attention from a dynamical systems perspective as there are associated robust heteroclinic cycles in reduced-order models (normal form equations) of such systems [3, 16, 31, 37, 80]. In particular, Nore *et al.* [75] have found slow-fast dynamic states that they have associated to the heteroclinic cycles in the normal form model. Nore *et al.* [73] have observed such states in experiments, the so-called near-heteroclinic cycles, albeit influenced to some degree by noise and geometrical defects.

Here, we study a flow related to the von Kármán swirling flow, with the essential difference being that instead of having a stationary sidewall, the sidewall is split at the half height, with each half rotating with the corresponding endwall. This flow has significantly less sidewall drag on the global torsional flow since the split sidewall halves also counter rotate at the same rate as their corresponding endwalls, and so may provide an enhanced dynamo action. This configuration has the same O(2) symmetry as the von Kármán swirling flow, but the shear at mid-height is much stronger for the same aspect ratio and rotation rates of the endwalls. As in the von Kármán swirling flow, the primary instabilities are dominated by the dynamics associated with O(2)

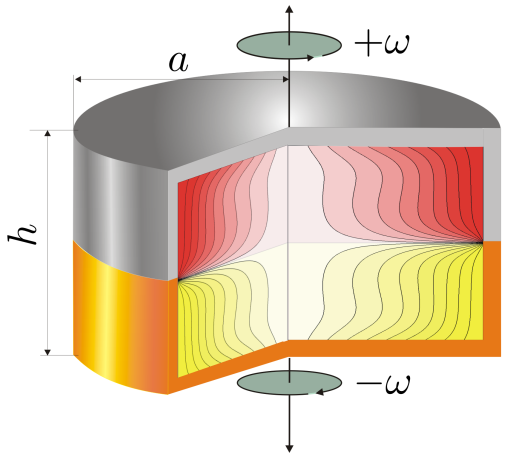


Figure 4.1: Schematic of the flow system. The inset shows contours of rv (vortex lines) for a basic state BS at $(\Gamma, Re) = (1, 115)$. There are ten quadratically spaced contour levels of $rv \in [-Re, Re]$, with positive being red and negative being yellow.

symmetry breaking, mode interactions and competitions, but in the split sidewall flow these occur at significantly lower Reynolds numbers (non-dimensional endwall rotation rates). Over a considerable portion of the range of Reynolds numbers and aspect ratios considered, the dynamics are dominated by pulse wave states that are associated to the O(2) symmetry breaking.

4.3 Governing Equations and Numerical Methods

The flow of a fluid of kinematic viscosity ν contained in a rotating split cylinder is studied numerically. The cylinder of radius a and length h is split in two at mid-height and the two halves are counter-rotating with angular speeds $\pm\omega$. A schematic of the problem is shown in figure 4.1. Using a as the length scale and a^2/ν as the time scale, the non-dimensional Navier–Stokes equations are

$$(\partial_t + \boldsymbol{u}\cdot\nabla)\boldsymbol{u} = -\nabla p + \nabla^2\boldsymbol{u}, \qquad \nabla\cdot\boldsymbol{u} = 0. \tag{4.1}$$

The no-slip boundary conditions are:

$$\begin{aligned}
&(u,v,w) = (0, rRe, 0) \text{ at the top endwall, } z = 0.5\Gamma,\\
&(u,v,w) = (0, -rRe, 0) \text{ at the bottom endwall, } z = -0.5\Gamma,\\
&(u,v,w) = (0, Re, 0) \text{ at the top half of the sidewall, } r = 1,\ z \in (0, 0.5\Gamma),\\
&(u,v,w) = (0, -Re, 0) \text{ at the bottom half of the sidewall, } r = 1,\ z \in (-0.5\Gamma, 0),
\end{aligned} \tag{4.2}$$

where the two governing parameters are

$$\begin{aligned}
&\text{aspect ratio:} && \Gamma = h/a,\\
&\text{Reynolds number:} && Re = \omega a^2/\nu.
\end{aligned} \tag{4.3}$$

In polar coordinates $(r, \theta, z) \in [0,1]\times[0,2\pi]\times[-0.5\Gamma, 0.5\Gamma]$, the velocity is $\boldsymbol{u} = (u, v, w)$ and the vorticity is $\nabla \times \boldsymbol{u} = (\chi, \eta, \zeta) = (w_\theta/r - v_z,\ u_z - w_r,\ v_r + v/r - u_\theta/r)$.

The Navier-Stokes equations are solved using a spectral code based on Mercader *et al.* [66], using a second-order time-splitting method and space discretized via a Galerkin–Fourier expansion in θ and Chebyshev collocation in r and z:

$$\boldsymbol{u}(r,\theta,z,t) = \sum_{i=0}^{2n_r+1} \sum_{j=0}^{n_z} \sum_{k=-0.5n_\theta}^{k=0.5n_\theta-1} \hat{\boldsymbol{u}}_{ijk}(t)\Xi_i(r)\Xi_j(2z/\Gamma)\mathrm{e}^{\mathrm{i}k\theta}, \tag{4.4}$$

where Ξ_n is the nth Chebyshev polynomial. The modal kinetic energies corresponding to azimuthal wavenumbers m are

$$E_m = \frac{1}{2}\int_{-0.5\Gamma}^{0.5\Gamma}\int_0^1 \boldsymbol{u}_m \cdot \boldsymbol{u}_m^* r\mathrm{d}r\mathrm{d}z, \tag{4.5}$$

where $\boldsymbol{u}_m$ is the mth Fourier component of the velocity field and $\boldsymbol{u}_m^*$ is its complex conjugate.

To avoid Gibb's phenomenon due to the discontinuity in the sidewall boundary condition for the azimuthal velocity, we regularized the boundary condition by smoothing the discontinuity over a small distance. Specifically, we replaced the boundary

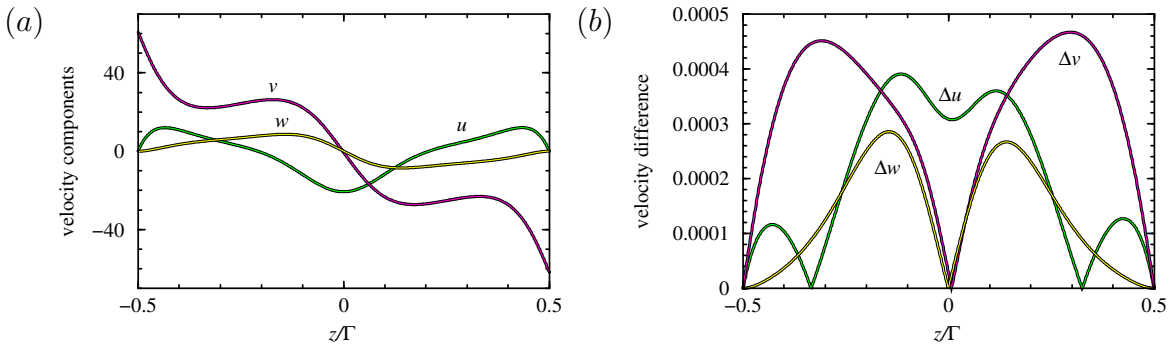


Figure 4.2: (a) Axial (z) profiles of the three velocity components at $r = 0.5$ and $\theta = 0$ of S2 at $(\Gamma, Re) = (1.45, 123)$ computed with $n_r = 40$, $n_\theta = 64$ and either $n_z = 120$ (thick black curves) or $n_z = 160$ (thin colored curves), and (b) the absolute differences between the three velocity component computed with the two resolutions.

condition for the azimuthal velocity with

$$v(r = 1, \theta, z) = Re \tanh(\epsilon z), \tag{4.6}$$

where ϵ governs the distance over which the jump is smoothed; $\epsilon = 50$ was used in this study, as was done in related rotating split-cylinder problems [25, 48]. A spatial resolution of $n_r = 40$, $n_z = 160$ and $n_\theta = 64$, and a time resolution of $\delta_t \in [10^{-4}, 10^{-5}]$ was used for the parameter range studied, $\Gamma \in [0.5, 2.0]$ and $Re \in [100, 300]$. In this parameter range, the resolution used results in spectral convergence in the coefficients in (6.3) of over sixteen orders of magnitude in θ, six orders of magnitude in r and three orders of magnitude in z. The slower convergence in z is due to using the L_∞ norm; the convergence is slowest in the neighborhood of the sidewall split, but this slow convergence is very localized and constrained by the viscous boundary layer. The convergence in z away from the split is comparable to that in r. Also, with this resolution, there are at least 15 collocation points across boundary layers, resulting in very well resolved solutions. Figure 4.2 illustrates how well the solutions are resolved

by presenting the axial velocity profiles of the three velocity components at $r = 0.5$ and $\theta = 0$ of a typical state, S2 at $(\Gamma, Re) = (1.45, 123)$, computed with $n_r = 40$, $n_\theta = 64$ and either $n_z = 120$ (thick black curves) or $n_z = 160$ (thin colored curves). On the scale of the plot, the two solutions are indistinguishable. Also shown in the figure are the absolute differences between the three velocity components computed with the two resolutions, showing that the difference resulting from a 33% increase in the axial resolution, from $n_z = 120$ to $n_z = 160$, only affects the solution in the fifth significant digit in the interior.

The system (6.1) and (4.2) is invariant to two spatial symmetries and a time translation $\mathcal{T}_\beta$. One spatial symmetry is $\mathcal{R}_\alpha$, the invariance to arbitrary rotations about the cylinder axis. It is isomorphic to the SO(2) symmetry group. The other spatial symmetry is $\mathcal{H}_\gamma$, the combined action of a reflection in any meridional plane $\theta = \gamma$ and a reflection in the mid-plane $z = 0$. This combined reflection is equivalent to a rotation of π about a direction through the center of the cylinder that is orthogonal to the cylinder axis and in the $\theta = \gamma$ plane. The $\mathcal{H}_\gamma$ involution is isomorphic to the Z_2 symmetry group; applying it twice is equivalent to the identity operation. The actions of $\mathcal{R}_\alpha$, $\mathcal{H}_\gamma$, and $\mathcal{T}_\beta$ on the velocity are

$$\begin{aligned}
\mathcal{R}_\alpha(u,v,w)(r,\theta,z,t) &= (u,v,w)(r,\theta+\alpha,z,t), \quad \alpha \text{ arbitrary},\\
\mathcal{H}_\gamma(u,v,w)(r,\theta,z,t) &= (u,-v,-w)(r,2\gamma-\theta,-z,t), \quad \gamma \text{ arbitrary},\\
\mathcal{T}_\beta(u,v,w)(r,\theta,z,t) &= (u,v,w)(r,\theta,z,t+\beta), \quad \beta \text{ arbitrary}.
\end{aligned} \tag{4.7}$$

The two spatial symmetries, $\mathcal{R}_\alpha$ and $\mathcal{H}_\gamma$, do not commute, and together they are isomorphic to the O(2) symmetry group.

Much of the nonlinear dynamics involves the breaking of some aspects of the symmetries of the problem. Table 4.1 lists the various states encountered in this study together with their symmetries. Each is described in detail in the following section. It is useful to be able to compute the unstable flows following the symmetry breaking

State	Symmetries
Basic state BS	$\mathcal{R}_\alpha \boldsymbol{u} = \boldsymbol{u}$, $\mathcal{H}_\gamma \boldsymbol{u} = \boldsymbol{u}$, $\mathcal{T}_\beta \boldsymbol{u} = \boldsymbol{u}$
Steady $\mathcal{H}$-symmetric Sm	$\mathcal{R}_{2\pi/m} \boldsymbol{u} = \boldsymbol{u}$, $\mathcal{H}_\gamma \boldsymbol{u} = \boldsymbol{u}$ for $2m$ angles γ, $\mathcal{T}_\beta \boldsymbol{u} = \boldsymbol{u}$
Rotating waves RW	$\mathcal{R}_\pi \boldsymbol{u} = \boldsymbol{u}$, $\mathcal{R}_\alpha \boldsymbol{u} = \mathcal{T}_{(\alpha T_w)/2\pi} \boldsymbol{u}$, $\mathcal{T}_{T_w} \boldsymbol{u} = \boldsymbol{u}$
Direction-reversing DRW	$\mathcal{R}_{\pi/2} \boldsymbol{u} = \boldsymbol{u}$, $\mathcal{T}_{T_E} \boldsymbol{u} = \boldsymbol{u}$
Pulse waves PWs	$\mathcal{R}_\pi \boldsymbol{u} = \boldsymbol{u}$, $\mathcal{R}_\alpha \boldsymbol{u} = \mathcal{T}_{T_E} \boldsymbol{u}$; α not a rational fraction of π
Pulse waves PWa	$\mathcal{R}_\alpha \boldsymbol{u} = \mathcal{T}_{T_E} \boldsymbol{u}$; α not a rational fraction of π
Pulse waves PWo	$\mathcal{R}_\pi \boldsymbol{u} = \boldsymbol{u}$, $\mathcal{T}_{2T_E} \boldsymbol{u} = \boldsymbol{u}$, $\mathcal{T}_{T_E} \boldsymbol{u} = \mathcal{R}_{\phi-2\gamma} \mathcal{H}_\gamma \boldsymbol{u}$ for a given ϕ
Limit cycles LC	$\mathcal{T}_{2T_E} \boldsymbol{u} = \boldsymbol{u}$, $\mathcal{T}_{T_E} \boldsymbol{u} = \mathcal{R}_{\phi-2\gamma} \mathcal{H}_\gamma \boldsymbol{u}$ for a given ϕ

Table 4.1: Summary of the different states and their symmetries. Note that α, γ and β are arbitrary unless otherwise indicated.

bifurcations. This can be readily done by restricting the computations to invariant symmetric subspaces. The most useful subspaces for this problem are the subspaces ξ_m, in which the flow is restricted to only having azimuthal wavenumbers $m = 0$ and multiples of m. Numerically, this is done by setting to zero the coefficients $\hat{\boldsymbol{u}}_{ijk}$ in (6.3) which do not correspond to these wavenumbers. There are two special such subspaces, ξ_0 which is the axisymmetric subspace and ξ_1 which is the full space.

4.4 Results

In the following subsections, we begin describing the features of the basic state, and consider its primary instabilities to group orbits of steady states. Then, we study in detail the 2:3 mode interaction, primarily in the neighborhood of the codimension-two (codim-2) point at $(\Gamma, Re) = (1.30, 129.5)$, and how some of the secondary bifurcation curves from that codim-2 point connect to the other 2:3 codim-2 point at

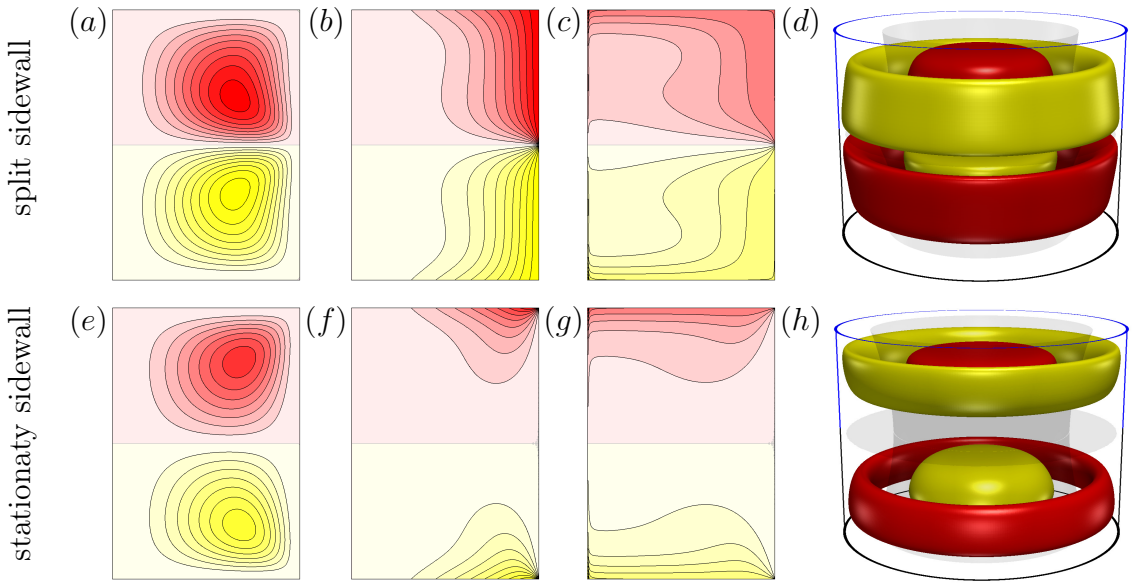


Figure 4.3: Contours in a meridional plane ($\theta = 0$, $r \times z \in [0,1] \times [-0.5\Gamma, 0.5\Gamma]$) of (a) ψ (streamlines), (b) rv (vortex lines), (c) v/r (angular velocity), and (d) isosurfaces of w of BS at $(\Gamma, Re) = (1.45, 115)$ for the split sidewall case (a, b, c, d) and the stationary sidewall case (e, f, g, h). The contour levels are linearly spaced (positive are red and negative are yellow) in the intervals $\psi \in [-1.25, 1.25]$, $rv \in [-Re, Re]$ and $v/r \in [-2Re, 2Re]$; the isosurfaces are at $w = \pm 0.05Re$ and at $w = 0$ (translucent).

$(\Gamma, Re) = (1.77, 118.6)$. We then consider in detail the dynamics as Re is increased while keeping $\Gamma = 1.45$ fixed. By computing not only in the full three-dimensional space ξ_1, but also by restricting the simulations to various symmetry subspaces ξ_m, we are able to provide a fairly complete picture of the complex dynamics involved. Finally, we provide a general overview of the various mode interactions and subsequent nonlinear dynamics over the broader parameter regime with $\Gamma \in [0.5, 2.0]$ and $Re \in [100, 300]$.

4.4.1 Basic State BS

The basic state, BS, is invariant to all symmetries of the system; it is steady and O(2) symmetric. The streamlines (contours of ψ, where $u = -1/r\,\partial\psi/\partial z$ and $w = 1/r\,\partial\psi/\partial r$), vortex lines (contours of rv), contours of angular velocity v/r, and isosurfaces of the axial velocity w of a typical BS at $(\Gamma, Re) = (1.45, 115)$ are shown in the top row of figure 4.3. Note that for an axisymmetric velocity $(u, v, w) = (-1/r\,\partial\psi/\partial z, v, 1/r\,\partial\psi/\partial r)$ and the corresponding vorticity is $(-1/r\,\partial(rv)/\partial z, \eta, 1/r\,\partial(rv)/\partial r)$, so that vortex lines in a meridional plane are tangent to the isocontours of rv. The dominant feature of BS is the shear layer formed at the cylinder mid-height resulting in two meridional recirculation cells indicated by the streamlines. The flow in each half cylinder would be in solid-body rotation (constant angular velocity), with opposing senses, if not for the presence of the flow in the other half cylinder. These two counter-rotating bodies of fluid meet at the mid-plane $z = 0$ and the vortex lines cannot be aligned with the axis at the mid-plane. The vortex lines emerge from the rotating endwalls and bend to be parallel to the mid-plane as they approach the split in the cylinder sidewall for the symmetric BS flow state. This vortex line bending produces the mid-plane shear layer and drives the meridional circulation, characterized by the streamlines in each cylinder half where flow is driven radially in toward the axis from the split in the sidewall along $z = 0$. By about mid-radius, the meridional flows turn toward the respective endwalls at $z = \pm 0.5\Gamma$. The meridional flows in the endwall boundary layers are toward the sidewall. In the sidewall layer, the meridional flow is returned to the vicinity of the split at $z = 0$, completing the meridional circulation. A consequence of the meridional flows in the two halves is that the interior flows rotate slower than the respective endwalls, as evidenced from the angular velocity plot.

For comparison purposes, the corresponding plots for BS in the von Kármán swirling

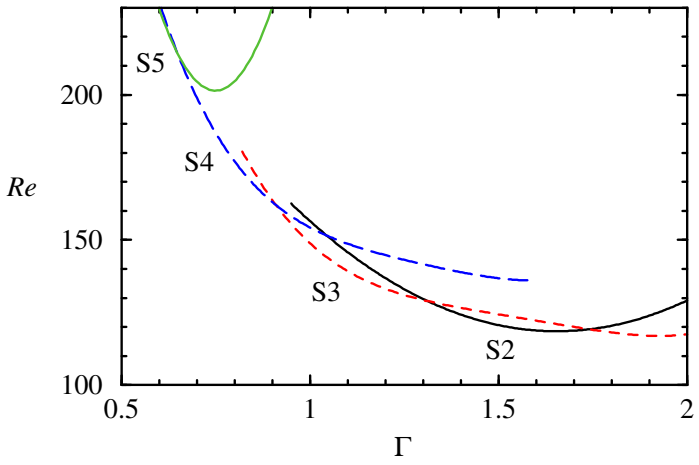


Figure 4.4: Loci in (Γ, Re) parameter space of circle-pitchfork bifurcations where BS loses stability to $\mathcal{H}$-symmetric steady states Sm, with azimuthal wavenumber m as indicated, upon crossing from low values of Re and Γ.

flow at the same (Γ, Re) are shown in the bottom row of figure 4.3. The vortex lines still emerge from the rotating endwalls, but due to the sidewall being stationary, they terminate at the corners where the sidewall and the endwalls meet. This results in the azimuthal shear at the mid-plane, $\partial v/\partial z|_{z=0}$, being much weaker than in the split cylinder case, and the angular velocity in the interior is also considerably weaker. The resultant meridional flow is strongest near the corners where the vortex lines terminate, in contrast to the split sidewall case where the meridional flow is strongest near the sidewall split, which is where its vortex lines terminate. All in all, the split sidewall case produces a more intense azimuthal shear layer at mid-height with a stronger meridional jet flow at mid-height.

4.4.2 Circle-pitchfork Bifurcations to Steady $\mathcal{H}$-symmetric States Sm

For small enough Re, depending on Γ, the steady O(2)-symmetric BS flow is stable. Over the range of aspect ratios considered, $\Gamma \in [0.5, 2.0]$, the basic state

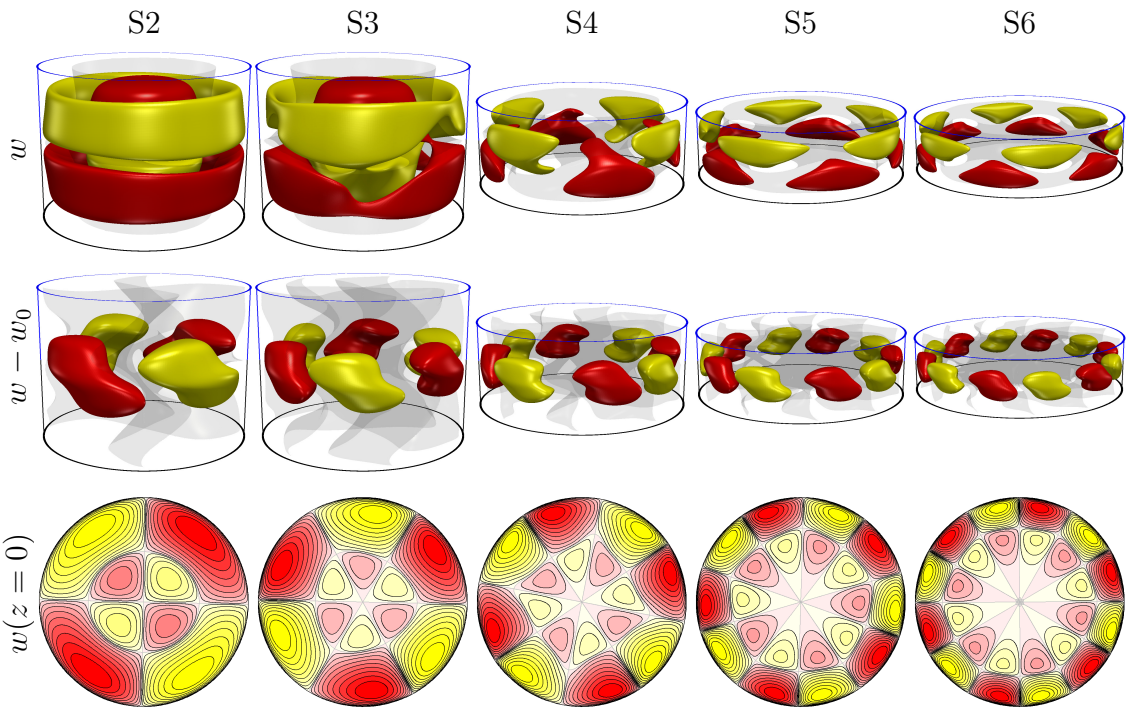


Figure 4.5: Isosurfaces of w (first row), $w - w_0$ (second row) and contours of w at $z = 0$ (third row), for S2 at $(\Gamma, Re) = (1.45, 123)$, S3 at $(\Gamma, Re) = (1.45, 135)$, S4 at $(\Gamma, Re) = (0.80, 225)$, S5 at $(\Gamma, Re) = (0.60, 250)$, and S6 at $(\Gamma, Re) = (0.50, 300)$.

BS loses stability as Re is increased via circle-pitchfork bifurcations where the flow loses axisymmetry (the $\mathcal{R}_\alpha$ invariance is broken), but remains steady ($\mathcal{T}_\beta$ invariant). Figure 4.4 shows the loci of the various circle-pitchfork bifurcations in (Γ, Re) parameter space. Although the continuous invariance $\mathcal{R}_\alpha$ (with α any angle) is broken, the flow retains a discrete invariance $\mathcal{R}_{2\pi/m}$, where m is the dominant azimuthal wavenumber of the flow. The value of m depends on Γ. We shall refer to these steady flows as Sm. Figure 4.5 shows typical Sm states, with $m \in [2, 6]$, where for each case, isosurfaces of the axial velocity w, and of the non-axisymmetric component $w - w_0$, where w_0 is the azimuthal average of w, are shown, together with contours of w at the mid-plane

$z = 0$ (note that for these steady states, $w_0 = 0$ at $z = 0$). The isosurface levels depicted in this and in subsequent figures are all at ± 0.4 of the maximum of w and $w - w_0$, respectively. The contour levels of w at the mid-plane are quadratically spaced in $\pm \max(w|_{z=0})$, to enable comparisons between solutions at different points in (Γ, Re) parameter space. The bifurcating states Sm are $\mathcal{H}_\gamma$ invariant, but instead of γ being any angle, now there are only $2m$ angles differing by multiples of π/m for which the states are $\mathcal{H}$-symmetric. The angles are easily identified, they correspond to the orientations of the straight lines, along which $w = 0$, through the origin the cylinder mid-plane (see figure 4.5). For any m, there is a group orbit of stationary $\mathcal{H}$-symmetric states Sm with azimuthal wavenumber m. All members of the group are obtained from any one of them by rotating it in azimuth, giving a whole circle of solutions. Which one is realized depends on initial conditions.

In summary the Sm have the invariances $\mathcal{R}_{2\pi/m}\boldsymbol{u} = \boldsymbol{u}$, $\mathcal{H}_\gamma\boldsymbol{u} = \boldsymbol{u}$ for $2m$ angles differing by multiples of π/m, and $\mathcal{T}_\beta\boldsymbol{u} = \boldsymbol{u}$ for arbitrary β.

For the von Kármán swirling flow, it has been suggested that the shear layer at mid-height in the basic state loses stability via a Kelvin–Helmholtz type of instability leading to steady states with azimuthal wavenumbers $m \approx 2/\Gamma$ [74, 75]. In our flow, we do not find strong evidence for this. Figure 4.4 shows that S2 bifurcates for $\Gamma \sim 1.5$, and S3 bifurcates for both $\Gamma \sim 1$ and $\Gamma \sim 2$, and both co-exist over a large range of Γ. Another mechanism that is acting to make BS unstable is the counter rotation. Vortex lines in a rotating system have a tendency to align with the rotation axis. When the flow is axisymmetric, the exact counter rotation of the two halves of the cylinder results in the vortex lines being forced to be tangential to the mid-plane. By breaking axisymmetry, some of the vortex lines from one half can penetrate partially into the other half, resulting in the interface between the two counter-rotating bodies of fluid being undulated. The axial velocity w at $z = 0$ is a proxy for the interface undulation;

this is shown in the third row of figure 4.5 for the different Sm found. Furthermore, for the Kelvin–Helmholtz instability of shear flow in a constant density fluid, the base flow velocity vector is planar two-dimensional and the vorticity vector is orthogonal to the velocity (i.e. the helicity, dot product of the velocity and vorticity vectors, is zero). In the problem under study, where the shear layer is due to counter-rotating bodies of fluid, the flow has non-zero helicity even in the absence of any instability, and the helicity is more intense when axisymmetry is broken. Large values of helicity indicate that the velocity and vorticity vectors are more aligned, and this leads to intensification of the vorticity via vortex stretching. Viscous dissipation can limit this process. In a related flow, consisting of a rotating cylinder with a counter-rotating top endwall [50], a shear layer emanating from the corner where the sidewall and the counter-rotating top meet separates the counter-rotating bodies of fluid. That flow loses axisymmetry at Re about an order of magnitude larger than in the present split-cylinder arrangement. The instability is also associated with the vortex lines trying to align themselves with the rotation axis and in doing so they try to penetrate through the shear layer. With the larger Re, this penetration is not as viscously damped, and the result is a number of funnels of counter-rotating fluid, intensified by vortex stretching, penetrating all the way to the opposite endwall boundary layer. This type of behavior is also present in the split-cylinder problem, but the penetration is symmetric into both halves, and not as intense due to the viscous dissipation in the lower Re flow.

The bifurcation curves in figure 4.4 indicate that there are several codim-2 points where two different circle-pitchfork bifurcation curves intersect. As is typical in many problems with O(2) symmetry, these codim-2 points correspond to curves with wavenumbers m and $m+1$. These points organize the mode interaction dynamics. Dangelmayr [16] has shown that these mode interactions lead to rather distinct

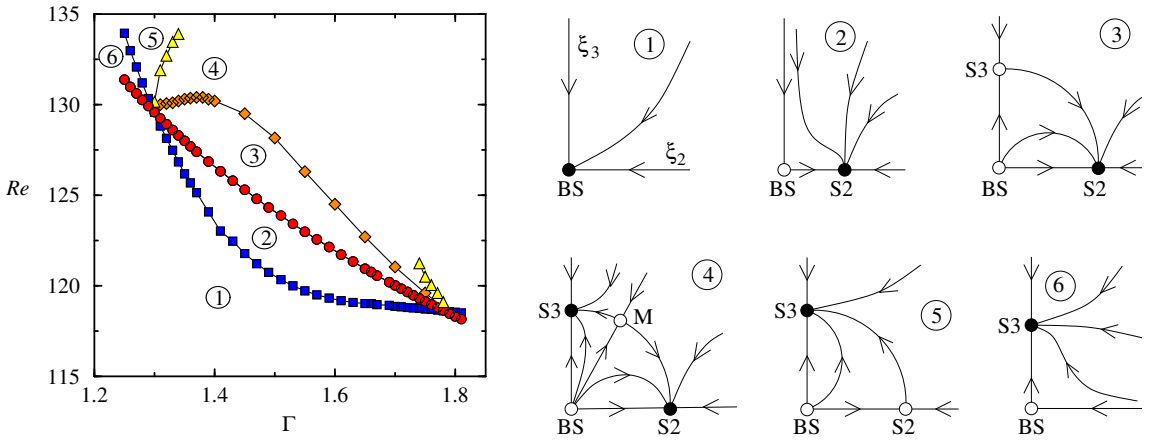


Figure 4.6: Bifurcation curves near the 2:3 mode interaction, together with schematic phase portraits in the regions near the codim-2 point at $(\Gamma, Re) = (1.3, 129.5)$; ξ_2 and ξ_3 are the $m = 2$ and $m = 3$ subspaces.

behavior depending on if $m = 1$ or $m > 1$. The case $m = 1$ gives rise to the 1:2 resonant interaction, which has attracted much theoretical interest and was found and studied in the von Kármán swirling flow by Nore *et al.* [75]. In our flow for the range of Γ considered, there is no circle-pitchfork bifurcation with $m = 1$. However, for $\Gamma \in (1.3, 1.75)$, a circle-pitchfork bifurcation with $m = 2$ is flanked by two others with $m = 3$, and Dangelmayr [16] showed that the 2:3 mode interaction also has distinct behavior compared to mode interactions with higher wavenumbers.

4.4.3 The 2:3 Mode Interaction

Figure 4.6 shows the circle-pitchfork bifurcation curves along which S2 and S3 bifurcate from BS together with schematics of phase portraits in distinct regions in the neighborhood of the codim-2 point where S2 and S3 bifurcate simultaneously. Generically, these circle-pitchfork bifurcation curves either do not intersect or they intersect at two points [16, 29]. In figure 4.6, there are two such intersection points,

$(\Gamma, Re) = (1.3, 129.5)$ and $(1.78, 118.7)$. We now consider a circular parameter sweep around one of these codim-2 points. In region 1, BS is the unique solution and it is stable. On increasing Re, BS loses stability to either S2 or S3, depending on Γ. S2 and S3 belong to the subspaces ξ_2 and ξ_3, respectively. Crossing from region 1 to region 2, the circle-pitchfork bifurcation renders BS unstable, and a stable group of S2 emerges. There are no other equilibria, stable or unstable, in region 2. Crossing into region 3 from region 2, BS undergoes another circle-pitchfork bifurcation and a group of S3 emerges and are unstable. Crossing from region 3 to region 4, S3 undergoes a steady-state bifurcation where it becomes stable. The normal form theory [see 16, 29, for more details] says that two types of unstable mixed-modes are spawned at the bifurcation (which we simply call M in the figure). These mixed-modes have non-zero $m = 2$ and $m = 3$ azimuthal Fourier components. Since the mixed-modes M are unstable and they do not reside in either the ξ_2 or ξ_3 subspace and they are not directly detectable.

Crossing from region 4 into region 5, another steady-state bifurcation takes place rendering S2 unstable (by absorbing the unstable mixed-mode M). Crossing from region 5 to region 6, S2 is absorbed into BS at the circle-pitchfork bifurcation. In region 6, the only equilibria are the stable S3 and unstable BS. Crossing from region 6 back to region 1 completes the parameter sweep around the codim-2 point, and S3 is absorbed into BS at the circle-pitchfork bifurcation where BS regains stability. The two circle-pitchfork bifurcations where S2 and S3 bifurcate from BS were found by direct simulations in the ξ_2 and ξ_3 subspaces, respectively. The steady-state bifurcations where S2 and S3 change stability were found by simulations in the full space ξ_1.

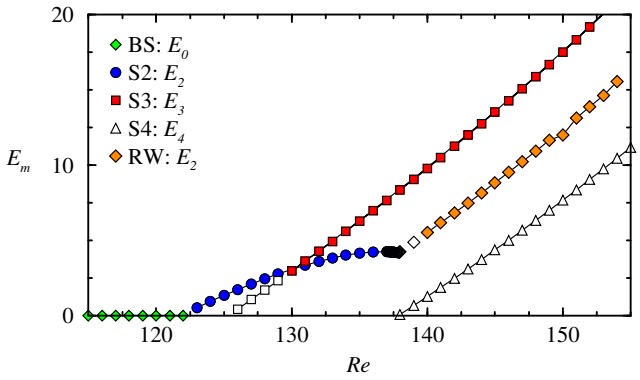


Figure 4.7: Variation of modal kinetic energies with Re for various states as indicated, with $\Gamma = 1.45$. The unstable states (open symbols) were computed in their respective subspaces.

4.4.4 Parameter Sweep in Re with $\Gamma = 1.45$

In order to investigate the nonlinear dynamics beyond the circle-pitchfork bifurcations, we focus on varying Re while keeping $\Gamma = 1.45$ fixed, which provides a parameter sweep through the middle of the region organized by the pair of 2:3 codim-2 points shown in figure 4.6. Figure 4.7 provides a summary of the various states and their stability in terms of the modal energy in their primary azimuthal wave number. Filled symbols indicate stable states in the full space ξ_1 and open symbols indicate unstable states which were computed in their respective subspaces ξ_m.

With $\Gamma = 1.45$ fixed, BS is stable for $Re \lesssim 122.5$. It becomes unstable for larger Re via the circle-pitchfork spawning the circle of steady states S2. At $Re \approx 125.5$, BS undergoes another circle-pitchfork bifurcation and spawns a circle of steady states S3, which are unstable since BS is also unstable. This bifurcation and the unstable S3 were computed in the subspace ξ_3. At $Re \approx 129.5$, the unstable S3 undergoes a bifurcation at which it is rendered stable. So far, all of these bifurcations were discussed in the context of figure 4.6, and are associated with the dynamics local to

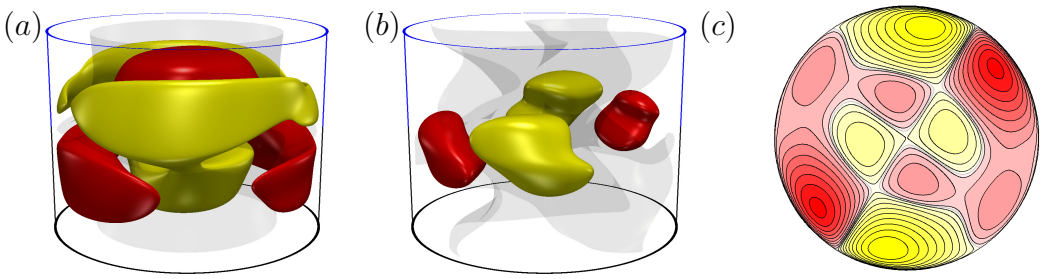


Figure 4.8: Isosurfaces of (a) w, (b) $w - w_0$, and (c) contours of w at $z = 0$, for RW at $(\Gamma, Re) = (1.45, 142)$. See the online movie for an animation of $w - w_0$.

the 2:3 codim-2 points. As Re approaches 138, a number of other events unfold. At $Re \approx 137.5$, S2 becomes unstable. At slightly larger Re, using S2 from slightly lower Re as the initial condition, the flow evolves to the stable S3. However, restricting the flow to the ξ_2 subspace, S2 remains stable until $Re \approx 137.9$, at which point it loses stability via a drift-pitchfork bifurcation [12, 13, 20, 35] at which a rotating wave, RW, with azimuthal wavenumber $m = 2$ is spawned. This RW will be described in detail in §4.4.5. S2 continues to exist beyond the drift-pitchfork bifurcation but it is unstable, both in ξ_1 and ξ_2, and we do not have a convenient way to compute it.

Also at $Re \approx 137.9$, BS undergoes a third circle-pitchfork bifurcation creating an unstable S4 which we are able to compute in the ξ_4 subspace. We have continued the S4 branch in ξ_4 to $Re = 200$. Note that S2 and S3 do not exist in ξ_4. In ξ_4, S4 is stable until it loses stability at $Re \approx 161.5$ in a supercritical Hopf bifurcation that breaks the $\mathcal{H}_\gamma$ symmetry of S4, spawning a direction-reversing wave DRW [40]. This DRW will be described in detail in §4.4.6.

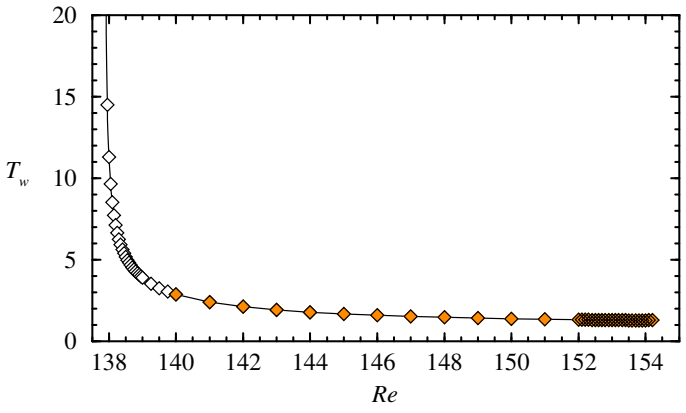


Figure 4.9: Drift period of RW, T_w, versus Re, together with a curve fit $T_w = 0.117 + 4.018/\sqrt{Re - 137.872}$. The unstable RW (open symbols) were computed in ξ_2.

4.4.5 Rotating Wave RW from a Drift-pitchfork Bifurcation

As mentioned above, the drift-pitchfork bifurcation takes place in ξ_2 as S2 is unstable in the full space ξ_1. A distinct characteristic of the drift-pitchfork bifurcation is that it breaks the $\mathcal{H}_\gamma$ symmetry. Like the S2 from which they bifurcate, RW have broken rotational invariance $\mathcal{R}_\alpha$ (for arbitrary α, except $\alpha = \pi$), and since $\mathcal{H}_\gamma$ is also broken, they drift slowly in θ near onset. Since the $\mathcal{H}_\gamma$ symmetry is broken, these rotating waves come in counter-rotating pairs; one is obtained by applying $\mathcal{H}_\gamma$ to the other, and which one is realized depends on initial conditions. The drift speed is zero at the bifurcation at $Re = Re_c$, and it grows as $\sqrt{|Re - Re_c|}$. A typical RW at $(\Gamma, Re) = (1.45, 142)$ is shown in figure 4.8. The broken $\mathcal{H}_\gamma$ symmetry is most clearly detected in the contour plot of w at the mid-plane, which has no straight $w = 0$ contour through the center of the cylinder (compare with the $w(z = 0)$ contour plot for S2 in figure 4.5, which has two such lines through the center).

Since rotating waves simply drift at a constant speed without change of shape (see the associated online movie), their modal kinetic energies are time invariant, but a

point-wise measure (a velocity component at some point) has a periodic signal. The period of such a signal, T_w, for RW as a function of Re is shown in figure 4.9. The open symbols correspond to RW computed in ξ_2 and the filled symbols correspond to RW computed in the full space ξ_1. The curve fit is $T_w = 0.117 + 4.018/\sqrt{Re - 137.872}$, indicating that the drift-pitchfork bifurcation happens at $Re \approx 137.872$. In summary, the RW have the invariances $\mathcal{R}_\pi \boldsymbol{u} = \boldsymbol{u}$, $\mathcal{R}_\alpha \boldsymbol{u} = \mathcal{T}_{(\alpha T_w)/2\pi} \boldsymbol{u}$ for arbitrary α, and $\mathcal{T}_{T_w} \boldsymbol{u} = \boldsymbol{u}$.

At $Re \approx 139.8$, the unstable RW undergoes a bifurcation in ξ_1 that renders it stable for larger Re. What is spawned at this bifurcation is unstable and we do not have any direct information to determine its features, but the bifurcation must be of subcritical symmetry-breaking type as RW in ξ_2 does not change stability type in this range of Re. RW remains stable up to $Re \approx 154.1$; simulations at slightly larger Re using RW at slightly lower Re as the initial condition evolve to a different time dependent state that has very different spatio-temporal characteristics compared to RW. We call this new state a pulse wave PWs, for reasons that will become evident when we describe it in section 4.4.7.

4.4.6 Direction-reversing Wave DRW from a Hopf Bifurcation

We now turn our attention to ξ_4 and S4 that bifurcates from BS at $Re \approx 137.9$. S4 loses stability in ξ_4 at $Re \approx 161.5$ in a supercritical Hopf bifurcation that breaks the $\mathcal{H}_\gamma$ symmetry. Figure 4.10 shows snap-shots over one period of the direction reversing wave DRW at $(\Gamma, Re) = (1.45, 165)$, and the accompanying movie animates the $w - w_0$ isosurfaces for this case, illustrating how the structure oscillates back and forth in the azimuthal direction with a swelling and deflation of the structure in a period T_E (the period of the modal kinetic energy variation). The key ingredient necessary for a direction-reversing wave is a Hopf bifurcation that breaks the reflection symmetry of

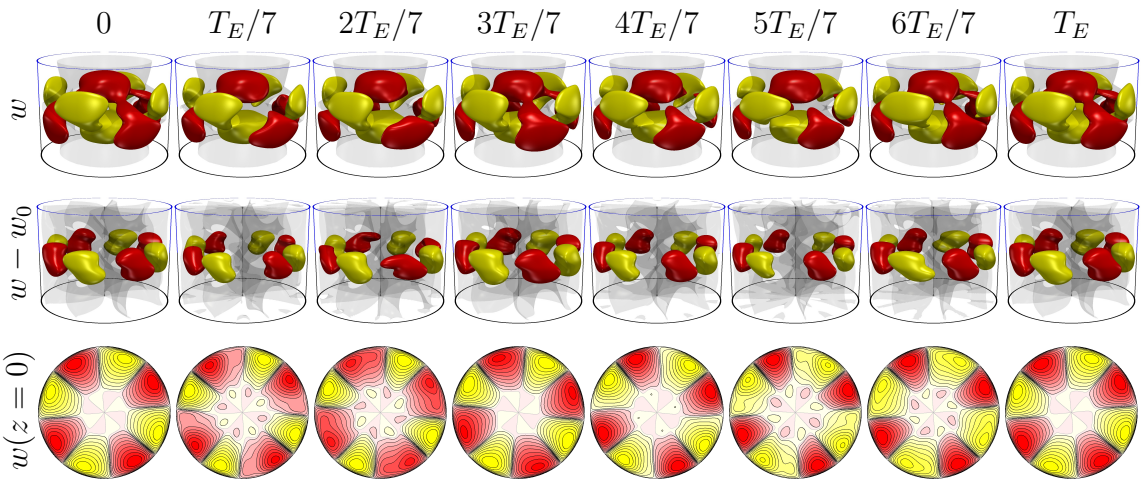


Figure 4.10: Snapshots over one T_E period relative to an arbitrary reference time of w-isosurfaces, $w - w_0$-isosurfaces, and w contours at $z = 0$ for DRW at $(\Gamma, Re) = (1.45, 165)$ computed in ξ_4. See the online movie for an animation of $w - w_0$.

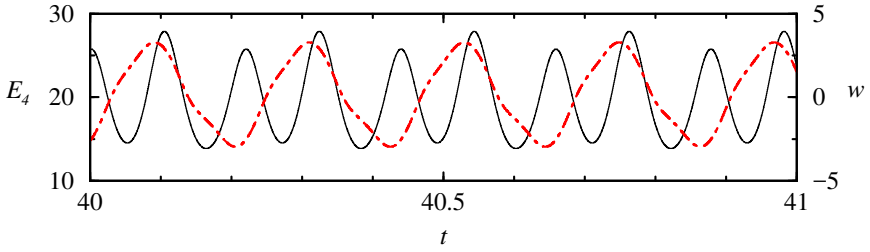


Figure 4.11: Time series of E_4 (solid line) and $w(0.98, 0, -0.4\Gamma)$ (dashed line) of DRW at $(\Gamma, Re) = (1.45, 165)$, computed in ξ_4.

a circle of non-trivial steady states, in our case these are S4 [40]. The breaking of the $\mathcal{H}_\gamma$ symmetry is most clearly seen by comparing the $w(z = 0)$ contour plots of DRW in figure 4.10 with those of S4 in figure 4.5, which is $\mathcal{H}$-symmetric about four lines through the axis.

Unlike RW which have constant modal kinetic energies, the modal kinetic energies of DRW are time periodic. Their frequency is associated with the Hopf frequency at

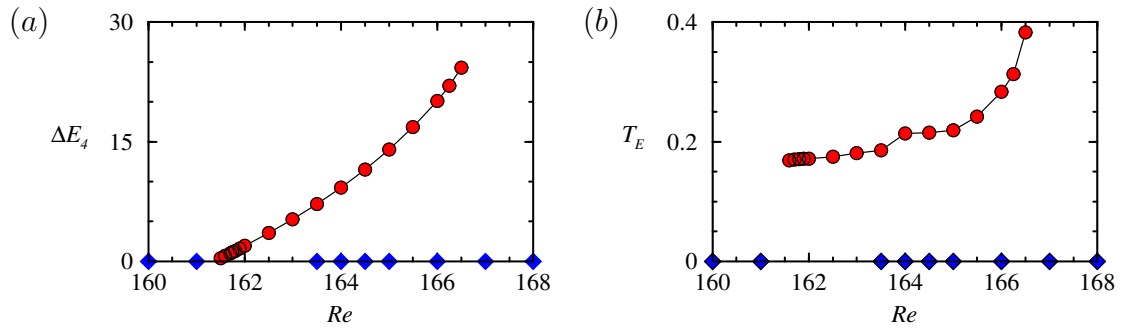


Figure 4.12: (a) Peak-to-peak amplitude and (b) period of E_4 for DRW at $\Gamma = 1.45$, computed in ξ_4. The stable S4 are indicated as (blue) diamonds in order to show the region of hysteresis between S4 and DRW.

the bifurcation and the peak-to-peak amplitude in the modal kinetic energies grow linearly from zero with $|Re - Re_c|$, for $Re \sim Re_c$. Figure 4.11 shows time series of modal kinetic energy E_4 and of $w(0.98, 0, -0.4\Gamma)$ for DRW at $(\Gamma, Re) = (1.45, 165)$; both are periodic with period T_E. Figure 4.12 shows the variations with Re of the peak-to-peak amplitude and period of E_4 for DRW. Near the bifurcation at $Re \approx 161.5$, the behavior of the amplitude and period is typical of a supercritical Hopf bifurcation [93]. DRW loses stability at $Re \approx 166.5$ in what is most likely a cyclic-fold bifurcation (saddle-node bifurcation of limit cycles), and S4 is stable for larger Re. We have continued S4 in ξ_4 up to $Re = 200$. Also, we have continued S4 to lower Re, and find that it becomes unstable at $Re \approx 163.5$ where is undergoes a subcritical Hopf spawning an unstable DRW to higher Re which is involved in the cyclic-fold bifurcation at $Re \approx 166.5$.

The fundamental difference between RW and DRW is that while both result from bifurcations of Sm that break $\mathcal{H}_\gamma$ (S2 for RW and S4 for DRW), the bifurcation leading to RW is steady (real eigenvalue crosses zero) while that leading to DRW is not (the real part of a complex-conjugate pair of eigenvalues changes sign), so for RW the

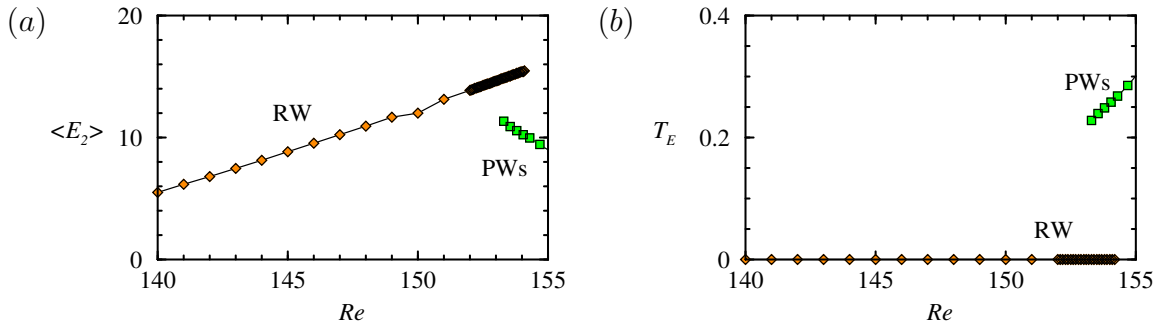


Figure 4.13: Variation with Re of (a) the time-averaged modal energy $\langle E_2 \rangle$ and (b) the period T_E of RW and PWs, for $\Gamma = 1.45$, computed in the full space ξ_1.

phase change is constant whereas for DRW it is periodic [40]. In summary, the DRW have the invariances $\mathcal{R}_{\pi/2}\boldsymbol{u} = \boldsymbol{u}$ and $\mathcal{T}_{T_E}\boldsymbol{u} = \boldsymbol{u}$.

4.4.7 Pulse Waves, PWs

Attempts to continue RW beyond $Re \approx 154.1$ in ξ_2 result in the same evolutions as in ξ_1, indicating that RW ceases to exist beyond $Re \approx 154.1$ due to a cyclic-fold bifurcation. For Re beyond this bifurcation, we find pulse wave states PWs. Like RW, PWs are invariant to $\mathcal{R}_\pi$, i.e. they reside in ξ_2. The PWs are stable to lower $Re \approx 153.3$, below which they are destroyed, presumably also in a cyclic-fold bifurcation, so that we have a region of hysteresis between RW and PWs over $Re \in (153.3, 154.1)$.

Figure 4.13(a) shows the time-averaged modal kinetic energy $\langle E_2 \rangle$ for RW and PWs over their hysteresis region in Re. Note that $\langle E_2 \rangle = E_2$ for RW. Figure 4.13(b) shows the corresponding energy period, T_E, of oscillation in E_2. For RW, $T_E = 0$ since the solution is only rotating, uniformly changing its azimuthal orientation, but not changing its structure.

PWs is an unsteady flow with slow-fast dynamics, as can be seen from the time series of E_2 and E_4 shown in figure 4.14(a). The fast dynamics consists of a rapid

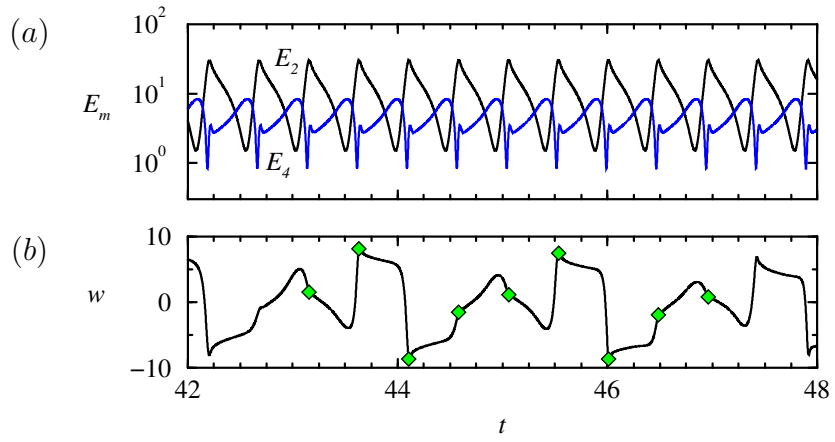


Figure 4.14: Time series of (a) modal kinetic energies E_2 and E_4, and (b) $w(0.98, 0, -0.4\Gamma)$ for PWs at $(\Gamma, Re) = (1.45, 153.5)$. The (green) diamonds correspond to the numbered diamonds in figure 4.16.

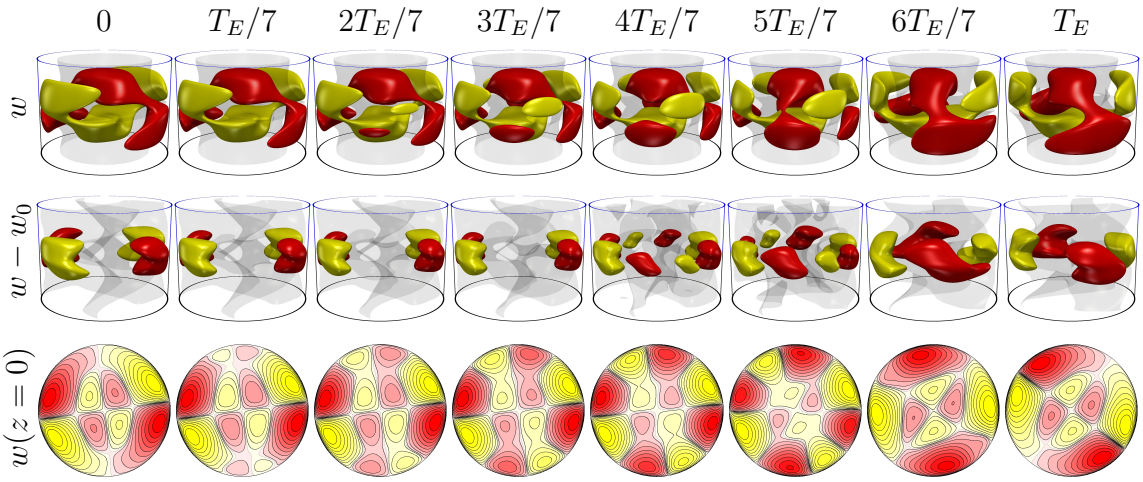


Figure 4.15: Snapshots over one T_E period relative to an arbitrary reference time of w-isosurfaces, $w - w_0$-isosurfaces, and w contours at $z = 0$ for PWs at $(\Gamma, Re) = (1.45, 153.5)$. See the online movie for an animation of $w - w_0$.

growth in E_2; when E_2 reaches its maximum, E_4 begins to grow and E_2 slowly decays, then the cycle repeats. The dynamics are easiest to visualize from isosurfaces of $w - w_0$. Figure 4.15 for PWs at $Re = 153.5$ shows snap-shots of w and $w - w_0$ isosurfaces and w contours at the mid-plane over one T_E period (the associated online movie animates the $w - w_0$ isosurfaces over $8T_E$ to better illustrate the slow-fast dynamics). The steady state S2 has two pairs of oppositely signed blobs of $w - w_0$ symmetrically distributed in azimuth about the mid-plane. In the slow phase of PWs, there are also two pairs of oppositely signed blobs of $w - w_0$. These blobs slowly diminish in size and the oppositely signed blobs in each pair slowly approach each other. In so doing, two increasingly wide swaths with near zero $w - w_0$ result about the mid-plane. Then, during the fast phase of the oscillation, two new pairs of blobs appear in the near zero swaths between the two existing pairs. When the new blobs are comparable to the pre-existing blobs, the positive new blobs and the negative old blobs move toward each other and the other blobs vanish, leaving a configuration that again closely resembles the S2 steady state, but rotated by approximately $\pi/4$ with respect to the earlier orientation. This occurs in one period T_E and the original orientation is almost regained in about $8T_E$.

Although the time series of the modal kinetic energies of PWs are T_E-periodic, PWs are not time periodic. This is evident from the time series of $w(0.98, 0, -0.4\Gamma)$, shown in figure 4.14 (b); the (green) diamonds in the figure are equispaced every T_E and correspond to maxima in E_2. What happens is that in exactly one period T_E, the structure of PWs is the same as its structure a period earlier, and hence has the same modal kinetic energies, but its orientation has changed by almost $\pi/4$, and so the local measure of w is different. If the orientation had changed by exactly $\pi/4$ (or some other rational fraction of π), the w signal would also be periodic, but this does not happen generically. Figure 4.16(a) shows a phase portrait of PWs at

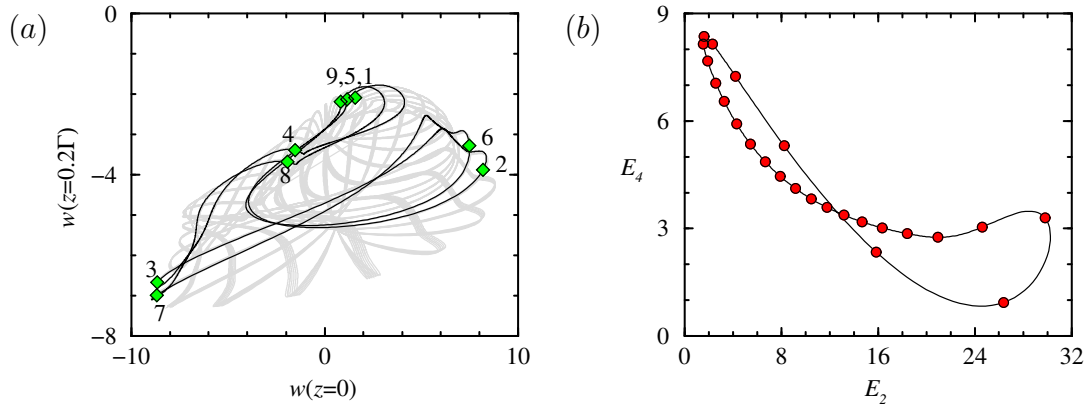


Figure 4.16: Phase portraits, (a) using $w(0.98, 0, 0, t)$ and $w(0.98, 0, 0.2\Gamma, t)$ and (b) using E_2 and E_4, for PWs at $(\Gamma, Re) = (1.45, 153.5)$; there are 25 equispaced-in-time circular markers over T_E.

$(\Gamma, Re) = (1.45, 153.5)$, using $w(0.98, 0, 0)$ and $w(0.98, 0, 0.2\Gamma)$, over many T_E, showing the structure of a 2-torus in gray. The line in black is a part of the trajectory over $8T_E$ and the (green) diamonds correspond to the same symbols in the corresponding time series in figure 4.14. The trajectory is almost a cycle that closes in on itself. However, it does not; the symbol labeled 9 does not coincide with that labeled 1, and the trajectory eventually covers the torus. Such states are sometimes referred to as relative periodic orbits, states that would appear to be periodic if viewed from a reference frame rotating at the angular rate corresponding to the angular change in orientation every T_E period. This is in the same sense that rotating waves are relative equilibria, states that would appear steady when viewed from a reference frame rotating at the angular rotation rate of the rotating wave. In figure 4.16(b), a phase portrait of the same PWs is shown using E_2 and E_4. This is a closed cycle, as expected. The symbols on the closed curve correspond to 25 uniformly spaced times over T_E, to show the slow-fast character of the oscillation.

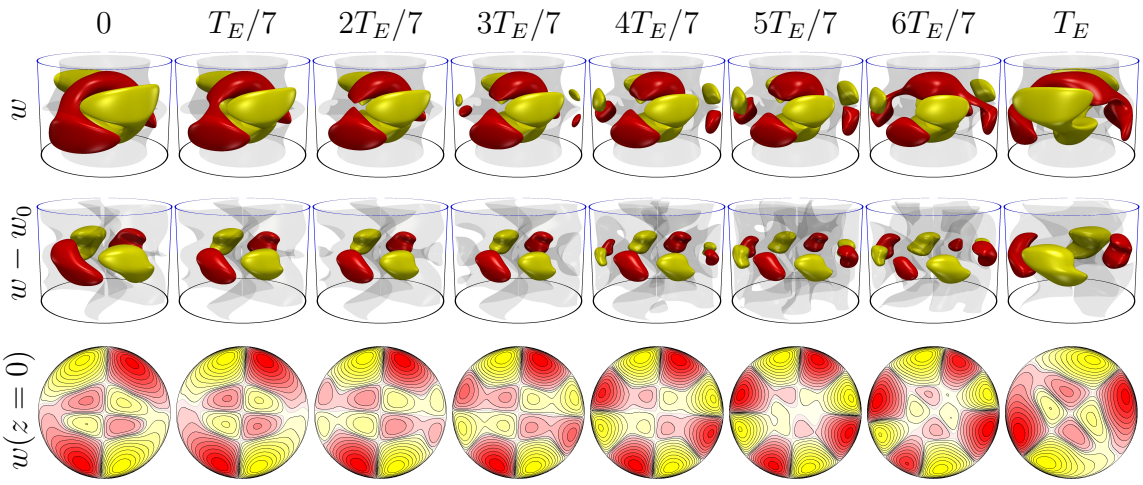


Figure 4.17: Snapshots over one T_E period relative to an arbitrary reference time of w-isosurfaces, $w-w_0$-isosurfaces, and w contours at $z = 0$ for PWa at $(\Gamma, Re) = (1.45, 160)$ computed in ξ_2. See the online movie for an animation of $w - w_0$.

In summary, the PWs have the invariances $\mathcal{R}_\pi \boldsymbol{u} = \boldsymbol{u}$ and $\mathcal{R}_\alpha \boldsymbol{u} = \mathcal{T}_{T_E} \boldsymbol{u}$ for some α that is not a rational fraction of π.

4.4.8 Symmetry-breaking to PWa

The pulse wave PWs is stable in ξ_1, but resides in ξ_2 since all of its odd azimuthal Fourier components have zero modal kinetic energy. PWs is stable up to $Re \approx 155.15$, where it loses stability in a supercritical symmetry-breaking bifurcation breaking the $\mathcal{R}_\pi$ rotational invariance. The state that is spawned is referred to as PWa. The bifurcation results in the $m = 3$ Fourier component being excited, and so PWa resides in the full space ξ_1. Like PWs, PWa has slow-fast dynamics, and for the most part looks very much like PWs, spending most of the time very close to the ξ_2 subspace, with a quick excursion out of it when E_3 is large. Figure 4.17 shows snap-shots of w and $w - w_0$ isosurfaces and w contours at the mid-plane over one T_E period for

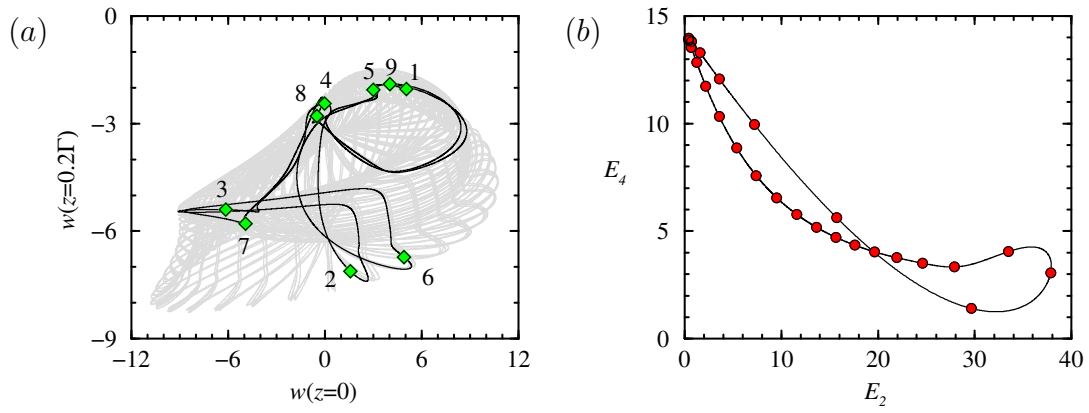


Figure 4.18: Phase portraits, (a) using $w(0.98, 0, 0, t)$ and $w(0.98, 0, 0.2\Gamma, t)$, and (b) using E_2 and E_4, for PWa at $(\Gamma, Re) = (1.45, 160)$; there are 25 equispaced-in-time circular markers over T_E.

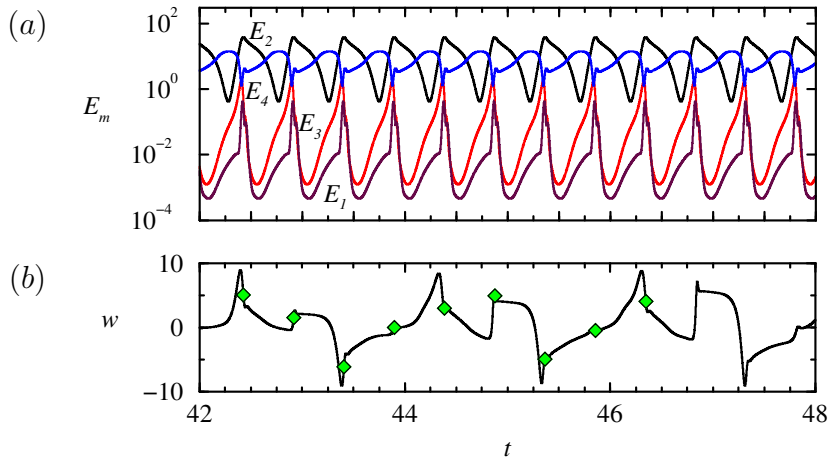


Figure 4.19: Time series of (a) modal kinetic energies E_1, E_2, E_3 and E_4, and (b) $w(0.98, 0, -0.4\Gamma)$ for PWa at $(\Gamma, Re) = (1.45, 160)$. The diamonds correspond to the numbered diamonds in figure 4.18.

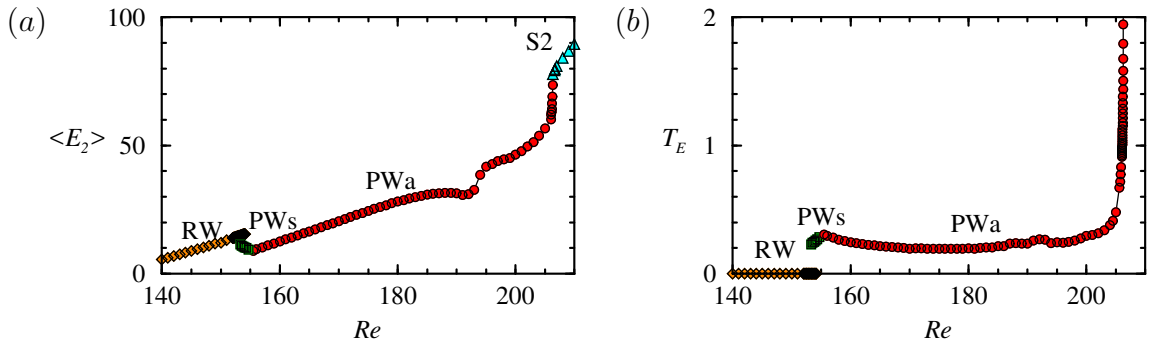


Figure 4.20: Variation with Re of (a) the time-averaged modal energy $\langle E_2 \rangle$ and (b) the period T_E of RW, PWs, PWa, and S2 for $\Gamma = 1.45$, computed in the full space ξ_1. Near $Re = 206$, the period of PWa has the fit $T_E = 0.285 + 0.831/\sqrt{206.312 - Re}$.

PWa at $(\Gamma, Re) = (1.45, 160)$. They are not very different from the corresponding images for PWs shown in figure 4.15. The phase portraits of PWa in figure 4.18 are also qualitatively the same as those for PWs shown in figure 4.16. However, the time series of E_1, E_2, E_3, E_4 and w in figure 4.19 clearly show how E_3 comes into play in the slow-fast dynamics. E_1 is smaller than and slaved to E_3, and comes about via the nonlinear interaction between E_3 with E_2 and E_4. Note that the E_m time series are also strictly T_E periodic, as for PWs. For both PWs and PWa, in exactly one period T_E, their structure is the same as it was a period earlier, and hence they have the same modal kinetic energies as they did one period earlier, but their orientation has changed, by almost $\pi/4$. They are both relative periodic orbits.

The PWa have the invariance $\mathcal{R}_\alpha \boldsymbol{u} = \mathcal{T}_{T_E} \boldsymbol{u}$ for some α that is not a rational fraction of π.

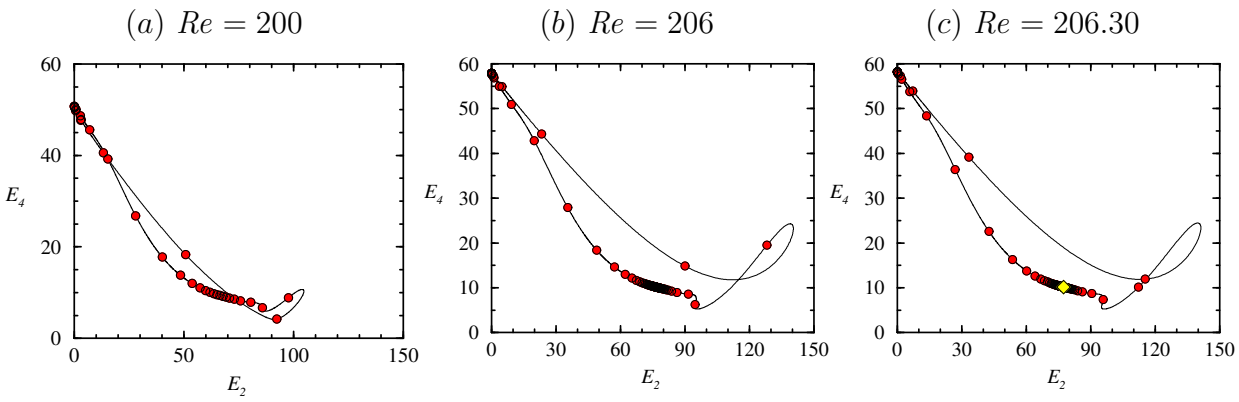


Figure 4.21: Phase portrait in (E_2, E_4) for PWa at $\Gamma = 1.45$ and Re as indicated. There are 25 equispaced-in-time circular markers over T_E, used to illustrate the slow-fast nonlinear oscillation. In (c), the (green) diamond corresponds to the steady S2 at $Re = 206.32$.

4.4.9 Saddle-Node-on-an-Invariant-Circle Bifurcation Destroying PWa

The period T_E of PWa does not vary very much from its onset following the symmetry-breaking instability of PWs at $Re \approx 155.15$ to $Re \approx 200$. As Re is increased beyond 200, T_E becomes increasing larger. Figure 4.20 shows how the amplitude (time-averaged E_2) and period T_E of RW, PWs and PWa vary with Re. Each symbol in the figure corresponds to an individual simulation that was run for many viscous times to establish its time-asymptotic behavior. For $Re > 200$, these simulations have been run for between 100 and 200 viscous times in order to accurately estimate the period T_E. Over this Re range, $T_E = 0.285 + 0.831/\sqrt{206.312 - Re}$ is a very good fit to the computed period, and indicates that the period becomes unbounded at $Re = 206.312$.

This inverse-square-root behavior of the period dependence on Re is typical of a SNIC bifurcation (a saddle-node-on-an-invariant-circle bifurcation). The slow-fast

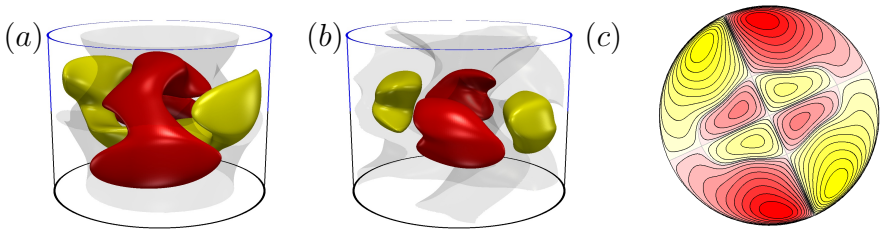


Figure 4.22: Isosurfaces of (a) w, (b) $w - w_0$, and (c) contours of w at $z = 0$, for S2 at $(\Gamma, Re) = (1.45, 206.32)$.

dynamics of PWa reaches a critical slowing down as $Re \to 206.312$. This is illustrated in figure 4.21, showing phase portraits of PWa at three Re approaching the critical value $Re = 206.312$. In the third portrait, corresponding to $Re = 206.30$, we find the (red) circles accumulate. On this same portrait we have included the (E_2, E_4) point as a (green) diamond, corresponding to the stable steady state that is found following the SNIC bifurcation at $Re = 206.32$. This steady state is S2; its features are illustrated in figure 4.22. It has the same features as PWa during it slow phase (e.g. compare with the 0 phase of figure 4.17).

4.4.10 Behavior over a Broader Range of Parameter Space

The one parameter sweep varying Re while keeping $\Gamma = 1.45$ revealed very rich dynamics and multiplicity of solutions, all associated with the manner in which the O(2) symmetry is broken. In this section, we provide a broader overview considering variations in Γ as well, although not in anywhere near as much detail. We have considered $\Gamma \in [0.5, 2.0]$ in increments of 0.05, and used the BS at $Re = 100$ for each of these Γ as the initial conditions for larger Re. For each Γ, solutions with Re up to 300, in increments of about 10 were computed until transients died off (up to a few dozen viscous time units). Some refinements in Re were done near the bifurcations

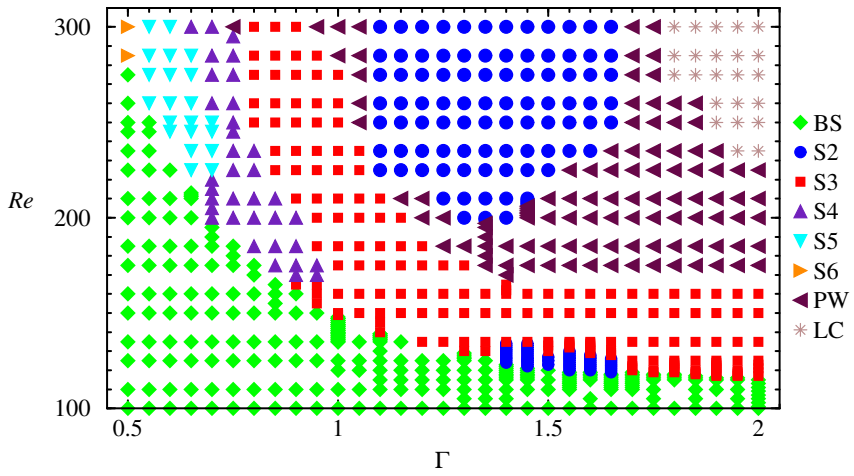


Figure 4.23: Loci of stable states in (Γ, Re), found by using BS at $Re = 100$ at each Γ as the initial condition for simulations for all Re at that Γ. No attempt was made to show loci of multiple stable states at the same point in parameter space that were found using other initial conditions.

for some of the cases. Figure 4.23 is a summary of the states computed using that process (about 800 simulations). Very close to the primary circle-pitchfork bifurcation curves, the corresponding Sm states are obtained. However, not too far after the circle-pitchfork bifurcations, the steady state S3 is obtained over a wide swath of parameter space. Then, the parameter space is dominated either by various types of pulse wave states (PWs and PWa, as well as others to be described below), or the S2 state that was found following the destruction of PWa via the SNIC bifurcation. Also, for a parameter region with $\Gamma \sim 2$ and $Re \sim 300$, a limit cycle state without any non-trivial spatial symmetry (the invariance to $\mathcal{R}_{2\pi}$ is trivial), but with a space-time symmetry, exists (described below). Of course, there are multiplicities of solutions throughout the parameter space, and the manner in which we have solved the sequences of initial value problems does not bring any of that richness out (repeating the procedure used

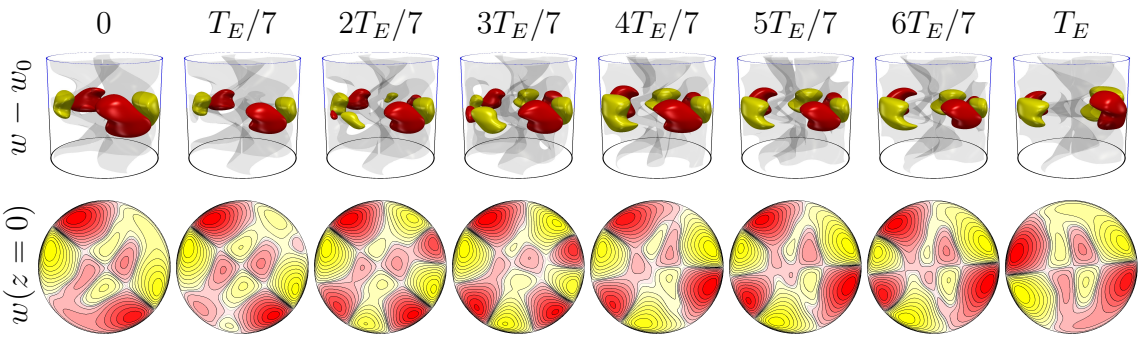


Figure 4.24: Snapshots over one T_E period relative to an arbitrary reference time $w - w_0$-isosurfaces and w contours at $z = 0$ for PWa at $(\Gamma, Re) = (1.80, 175)$. See the online movie for an animation of $w - w_0$.

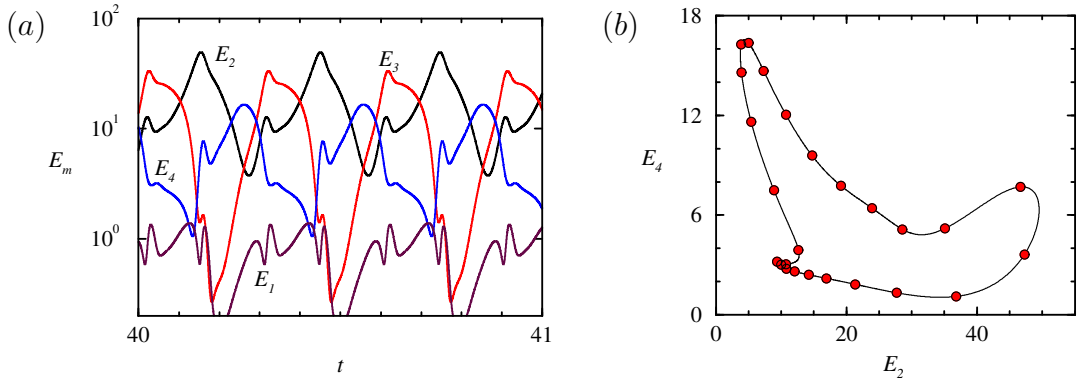


Figure 4.25: (a) Time series of E_m and (b) phase portrait using E_2 and E_4 for PWa at $(\Gamma, Re) = (1.80, 175)$.

in the one parameter sweep at $\Gamma = 1.45$ for the 30 other values of Γ is beyond the scope of the present study). However, it does provide an indication of which solution types are likely to be found.

We now address, to a very small degree, the changes in the pulse waves for different aspect ratios. In the parameter sweep varying Re and keeping $\Gamma = 1.45$ fixed, the level to which E_3 grows for PWa remains relatively small. However, by varying Γ

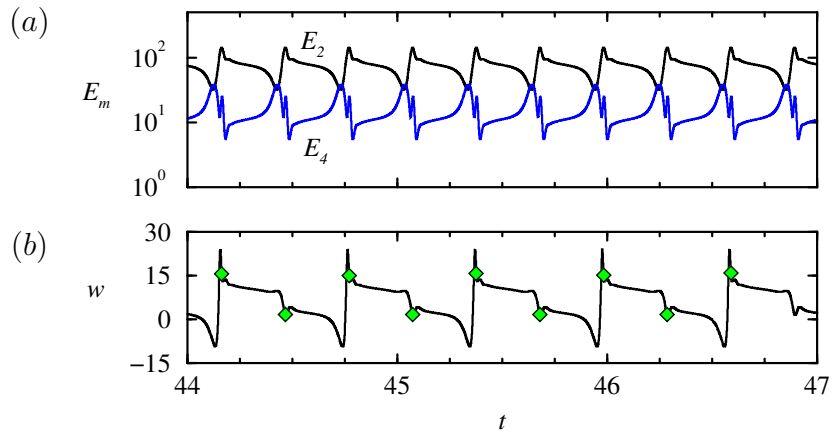


Figure 4.26: Time series of (a) modal kinetic energies E_2 and E_4 and (b) $w(0.98, 0, -0.4\Gamma)$ for PWo at $(\Gamma, Re) = (1.5, 210)$.

we have also found PWa in which E_3 is the dominant modal kinetic energy during a part of the oscillation. Figures 4.24 and 4.25 show snap-shots of $w - w_0$ isosurfaces and contour plots of w at the mid-plane, as well as time series of the modal kinetic energies and a phase portrait of PWa at $(\Gamma, Re) = (1.80, 175)$. While the PWa is of the same type as described earlier at $(\Gamma, Re) = (1.45, 160)$, it has a very different apparent dynamic due to E_3 being dominant over some time intervals. This is easiest to visualize from the online movie showing $w - w_0$ isosurface.

Another different pulse wave, PWo, was found at $(\Gamma, Re) = (1.50, 210)$. It only has 2 plateaus of E_2 energy instead of the 8 plateaus of PWs and PWa. Figure 4.26 shows the E_2 time evolution with the w evolution, showing that PWo is a periodic solution, with period $2T_E$, but the modal energies are T_E periodic. Figure 4.27 shows snapshots of w at the mid-plane together with isosurfaces of $w - w_0$. It pulses back-and-forth every $2T_E$, periodically switching its orientation, much like the direction-reversing waves DRW do. However, the oscillation is not smooth, but pulse-like. PWo have broken $\mathcal{R}_\alpha$ symmetry, for any angle α except π, so there is a group orbit of PWo

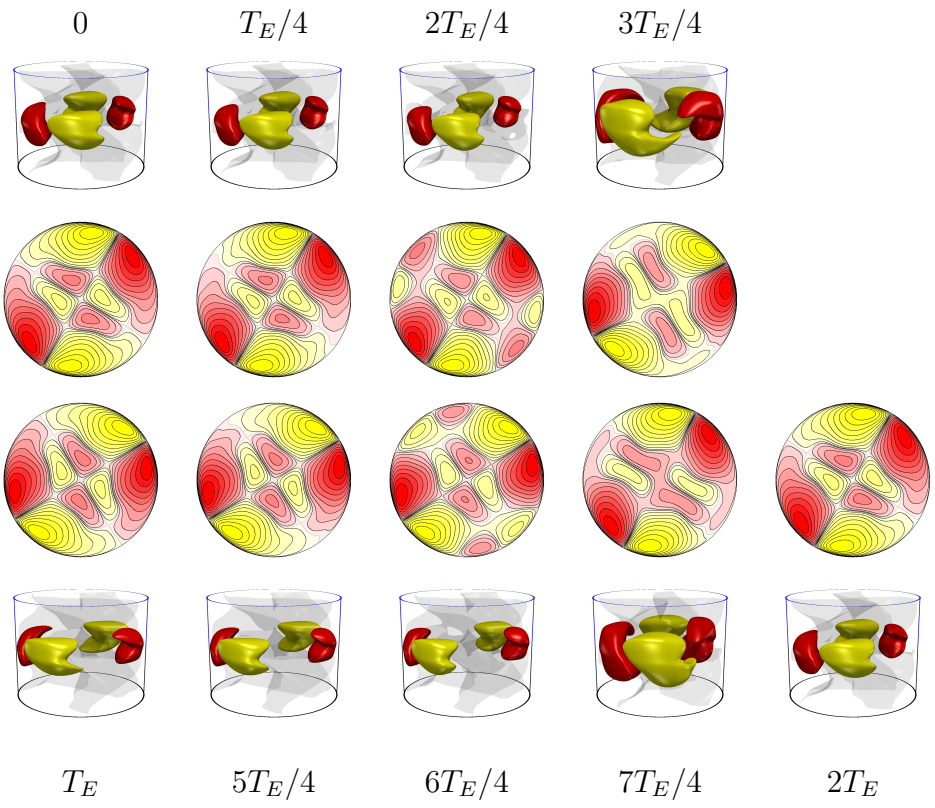


Figure 4.27: Snapshots of $w - w_0$ isosurfaces and w contours at $z = 0$ over $2T_E$ relative to an arbitrary reference time for PWo at $(\Gamma, Re) = (1.50, 210)$. See the online movie for an animation of isosurfaces of $w - w_0$.

obtained by applying $\mathcal{R}_\alpha$. Furthermore, since PWo have broken $\mathcal{H}_\gamma$ symmetry, there are two group orbits, one obtained by applying $\mathcal{H}_\gamma$ to the other (the angle γ is arbitrary, different values of γ will give a PWo on the other group orbit with a different orientation). PWo also have a space-time symmetry, a half-period-flip symmetry, where the flip is a composition of $\mathcal{H}_\gamma$ with a rotation. This half-period-flip symmetry can be seen by comparing the solution at some time t with the solution at $t + T_E$, particularly in the contours of w at the mid-plane as shown in figure 4.27.

In summary, the PWo has invariances $\mathcal{R}_\pi \boldsymbol{u} = \boldsymbol{u}$, $\mathcal{T}_{2T_E} \boldsymbol{u} = \boldsymbol{u}$, and $\mathcal{T}_{T_E} \boldsymbol{u} =$

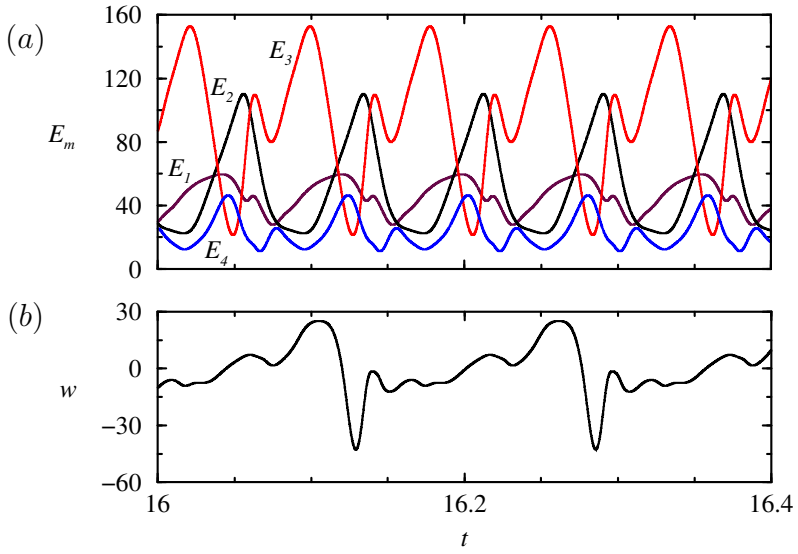


Figure 4.28: Time series of (a) modal kinetic energies E_1, E_2, E_3, and E_4, and (b) $w(0.98, 0, -0.4\Gamma)$ for LC at $(\Gamma, Re) = (1.9, 275)$.

$\mathcal{R}_{\phi-2\gamma}\mathcal{H}_\gamma \boldsymbol{u}$ for γ arbitrary and a given ϕ.

In the upper ranges of parameter space investigated, with $\Gamma \sim 2$ and $Re \sim 300$ (indicated in the upper right corner of figure 4.23) we have encountered limit cycles, LC, which do not have any non-trivial spatial symmetry. Figure 4.28 shows the time evolution of the leading modal kinetic energies and $w(0.98, 0, -0.4\Gamma)$ for LC at $(\Gamma, Re) = (1.90, 275)$. Unlike the pulse wave states, LC does not exhibit slow-fast dynamics. The period in w is $2T_E$, twice the period in the modal energies. This suggests that like PWo, LC has a space-time symmetry. Figure 4.29 shows snap-shots of $w - w_0$ isosurfaces and of w contours at $z = 0$, and together with the associated online movie, these allows us to determine the space-time symmetry of LC. Just like with PWo, applying $\mathcal{H}_\gamma$, for any γ, followed by the rotation $\mathcal{R}_{\phi-2\gamma}$ for a specific ϕ, to LC at any time t_0 results in LC at $t_0 + T_E$. To better illustrate this space-time symmetry and to provide a way to determine ϕ for a given γ, we defined a symmetry

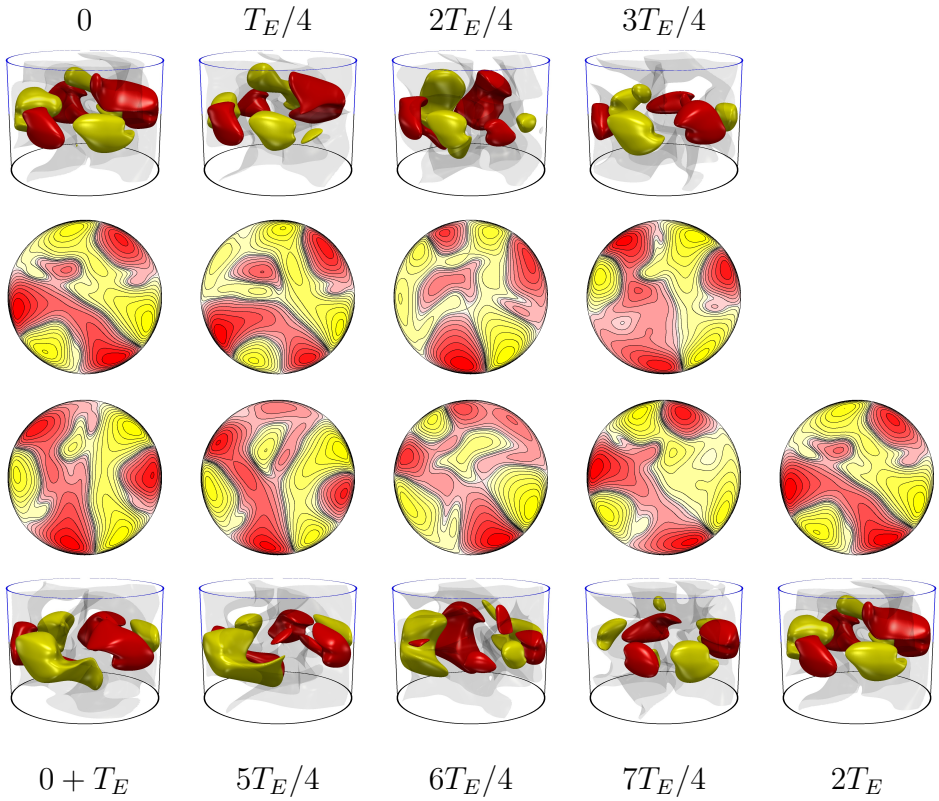


Figure 4.29: Snapshots of $w - w_0$ isosurfaces and w contours at $z = 0$ over $2T_E$ relative to an arbitrary reference time for LC at $(\Gamma, Re) = (1.90, 275)$. See the online movie for an animation of isosurfaces of $w - w_0$.

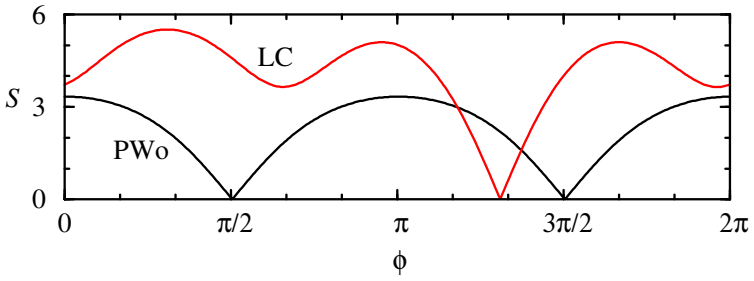


Figure 4.30: Variation of the symmetry measure S, using $\mathcal{H}_0$, with the rotation angle ϕ for PWo at $(\Gamma, Re) = (1.50, 210)$ and LC at $(\Gamma, Re) = (1.90, 275)$.

measure

$$S = ||\mathcal{R}_{\phi-2\gamma}\mathcal{H}_\gamma \boldsymbol{u} - \mathcal{T}_{T_E}\boldsymbol{u}||_2 \,. \tag{4.8}$$

Without lost of generality, figure 4.30 shows the symmetry measure S, calculated for a PWo state and a LC state when $\mathcal{H}_0$ is applied and considering $\phi \in [0, 2\pi]$. The symmetry measure is zero only for a specific $\phi = \phi_0$ (for PWo, $S = 0$ also for $\phi = \phi_0 \pm \pi$ because PWo is $\mathcal{R}_\pi$ symmetric). For any other γ, $S = 0$ at $\phi = \phi_0 - 2\gamma$. Apart from not having slow-fast behavior, the other main difference between LC and PWo is that while both have comparable levels of E_2, for LC the level of E_3 is significantly larger than any other E_m most of the time, and this leads to LC not having any non-trivial spatial symmetry.

In summary, LC has invariances $\mathcal{T}_{2T_E}\boldsymbol{u} = \boldsymbol{u}$ and $\mathcal{T}_{T_E}\boldsymbol{u} = \mathcal{R}_{\phi-2\gamma}\mathcal{H}_\gamma\boldsymbol{u}$ for γ arbitrary and a given ϕ.

4.5 Discussion and Conclusions

The dynamics of the flow in the split counter-rotating cylinder are dominated by the O(2) symmetry of the system. The O(2) symmetric basic state consists of two counter-rotating bodies of fluid, each completely contained within their respective half cylinders, separated by a plane at the cylinder mid-height to which the vortex lines are tangential. The vortex lines being tangential to the mid-plane results in an azimuthal shear layer that also has a radial jet profile due to the vortex line bending. This basic state configuration becomes unstable with increasing counter rotation (quantified non-dimensionally by Re); the critical Re is smaller for larger cylinder aspect ratios Γ. The primary instabilities are circle-pitchfork bifurcations, spawning group orbits of steady states Sm with azimuthal wavenumbers m. The value of m depends on Γ, and for the range considered ($\Gamma \in [0.5, 2.0]$), m ranges from 6 to 2. There are a number of codim-2 points where two curves of circle-pitchfork bifurcations cross in

(Γ, Re) parameter space, one curve corresponding to azimuthal wavenumber m and the other to $m+1$. We have studied in detail the dynamics in the neighborhood of the 2:3 codim-2 point, and the resulting mode interactions are well described by the associated normal form.

Further away in parameter space from the primary circle-pitchfork bifurcations, we have found a number of other bifurcations and states. Some of these states are unstable due to broken symmetries, and by computing in the appropriate symmetric subspaces we have been able to study their dynamics. We have found rotating waves and direction reversing waves that result from either steady or Hopf bifurcations breaking the involution $\mathcal{H}$ symmetry of the Sm from which they bifurcate. These time-periodic states are typical of O(2) symmetric systems. However, over much of the parameter space studied, these are not the predominant unsteady states found. Instead, we find that a variety of pulse wave states dominate the unsteady flow regimes. These are primarily characterized by slow-fast dynamics, with the slow phase corresponding to a particular orientation of a steady non-axisymmetric state, typically S2, and the fast phase corresponds to a rapid shift to a different orientation in the S2 group. Some pulse waves (PWs and PWo) reside in the symmetric subspace with only even Fourier azimuthal modes, while others (PWa) do not. We have also found other limit cycle solutions. All of these can be viewed as different choreographies as the vortex lines from one half of the cylinder try to penetrate into the other half, and the two sets of counter-rotating vortex lines negotiate their respective penetrations via flow configurations with different spatio-temporal symmetries.

All of the dynamics we have described are inherently related to how the O(2) symmetry of the system is broken as Re and Γ are varied. The O(2) symmetry owes its presence to the exact counter rotation of the two halves of the cylinder. Any slight difference in the rotation rates or the cylinder not being exactly split in

half would result in the system only having SO(2) symmetry. This then raises the question of how robust are the dynamics reported to slight imperfections. In the related von Kármán swirling flow, Nore *et al.* [73] showed experimentally that much of the O(2)-related dynamics persists in the face of experimental imperfections and noise. The details of the basic state and its bifurcations for the von Kármán swirling flow differ from those of the split cylinder flow, primarily due to the viscous drag from the stationary sidewall leading to very different vortex line distributions in the basic state and consequently undergoing different bifurcations. Yet, there are many similarities between the two flows and this is due to both systems being O(2) symmetric. In both cases the basic state first loses stability via circle-pitchfork bifurcations to three-dimensional steady states Sm, but the azimuthal wavenumber m in the two cases differs. In both cases there are mode interactions where two circle-pitchfork bifurcations occur simultaneously, and these codim-2 points organize the dynamics over a sizable region of parameter space, displaying various rotating and pulse waves. Given the experimentally observed robustness of the O(2) dynamics in the von Kármán swirling flow, it would be of interest to determine the effects of imperfections on the split cylinder flow. In particular, the pulse waves can be viewed as a dynamic where the flow is a structure pinned to one particular orientation undergoing a very slow change until it de-pins and then quickly pins to another orientation. We found that the pulse waves PWa cease to exist via a SNIC bifurcation, whereby the structure remains pinned in a particular orientation indefinitely. Pinning and depinning of rotating waves in SO(2) differentially rotating systems have also been reported and the role of imperfect symmetry has been investigated [1, 53, 65, 78]. These studies showed that SNIC bifurcations are predominant in the associated dynamics, but the details get extremely complicated. An investigation of imperfect O(2) symmetry in the split cylinder flow would be an interesting future exercise.

Acknowledgements

This work was supported by the U.S. National Science Foundation grant CBET-1336410.

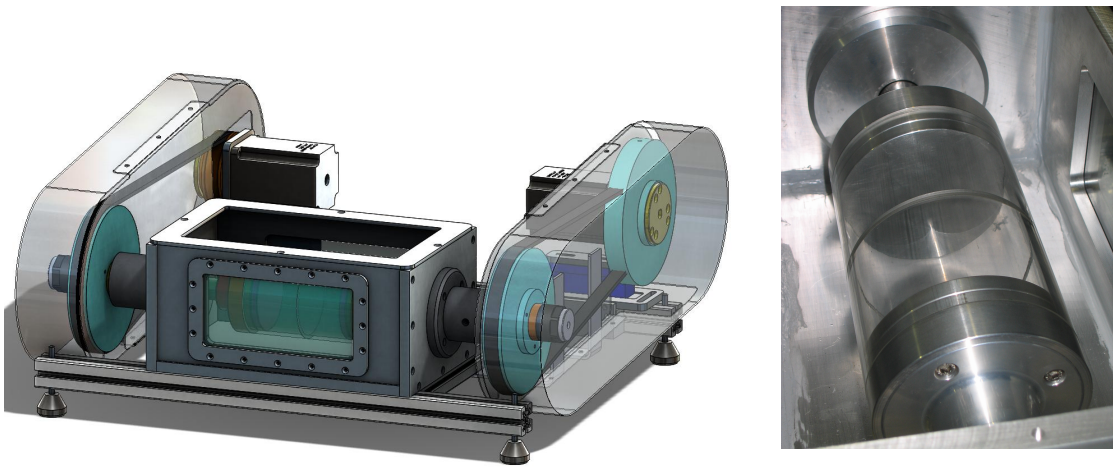
Chapter 5

PRELIMINARY EXPERIMENTAL COUNTER-ROTATING SPLIT CYLINDER

5.1 Experimental Setup

An experimental device was set up to reproduce the counter-rotating split configuration to supplement the extensive numerical study of the split-cylinder geometries. As it was explained in chapter 4, this counter-rotating geometries are frequently used as dynamo generators. The split-cylinder case generates more helicity which makes this geometry attractive for experimentalists The work presented in this chapter was completed in collaboration with the Fluids Lab of the University of Navarra team led by Dr. Javier Burguete who hosted me there for one and half month in Fall 2016.

The experimental device main feature is a transparent split-cylinder completely



(a) (b)

Figure 5.1: (a) Schematic of the experimental device and (b) experimental cylinder.

filled with a fluid. The cylinder size is internal radius 5 cm and height variable with the split being at half of the height. This split creates a gap was which designed to be the smallest possible to avoid interchange of fluid and at the same time to prevent friction between both halves of the cylinder. The size of the gap is 0.2 mm. Since the device has this division, the fluid leaks to outside of the cylinder. To avoid this leak, the cylinder is contained in a pool of size 37x25x18 cm. The pool and the shafts that rotate both halves of the cylinder are metallic, and due to the contact with the liquid, all the used materials have to be stainless. The pool has two lateral transparent windows of 24x12 cm, and it is opened in its top part making possible measurements.

Both halves of the cylinder rotate independently, each of one is connected to a stepper motor using rotating shafts and a system of straps. Figure 6.1 (a) shows a schematic of the experimental device and (b) shows a picture of the actual cylinder without fluid. Note that even though in the figures of the simulation the cylinder axis was vertical and the experimental device has the axis horizontal both systems are equivalent since the influence of the gravity is negligible.

The movement of these steppers motor produces unwanted vibrations in the system. A new design of the experimental table and adjustment of the tension of the straps connected to both motors was made improving the issue of the vibrations but without solving the problem completely. To avoid this phenomenon the motors were programmed to work in micro-steps producing 25600 micro-steps in every steps using a microstep driver. Also, the signals were filtered before arriving to the steppers motors using a home made LC system. After several tries, it was found that the best results are obtained using coils equivalent to 82 mH and condensers to 1 μF in each motor. Figure 5.2 shows a picture of the lab equipment to generate the signals. Since the viscosity and the geometry remains nominatively constant during an experiment, the relation between the frequency of the input signal and the Re associated to the



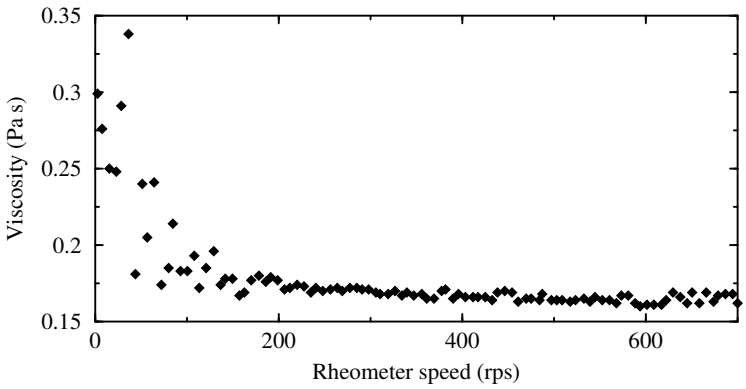
Figure 5.2: Signal generator.

problem is linear.

To obtain the desired range of Re the fluid used was glycerine with about a 10% of water. The viscosity of this handmade mixture was measured using a rheometer. Figure 5.3 (a) shows a picture of the equipment used. Notice that both fluids has to be well mixed before making a reliable measurement. Figure 5.3 (b) shows the viscosity measurements obtained using a rheometer. After neglecting the smaller speed measures, where both fluids were not well mixed yet, we can appreciate that the kinematic viscosity is about 0.17 Pa s. Notice also that during the viscosity measurements the temperature was measured simultaneously checking that it is varying in a range of $\pm 0.2°C$. Therefore, the influence of the change in temperature in the viscosity is negligible.

Note that one of the many difficulties of the set up is that the symmetries of the problem are crucial for the behavior of the flow in this configuration. There are some troublesome points as the alignment of the halves, the eccentricity of the cylinder, etc. To impose exact counter rotation is also problematic since both motors are independent. The error obtained by using as input the same signal in both motors





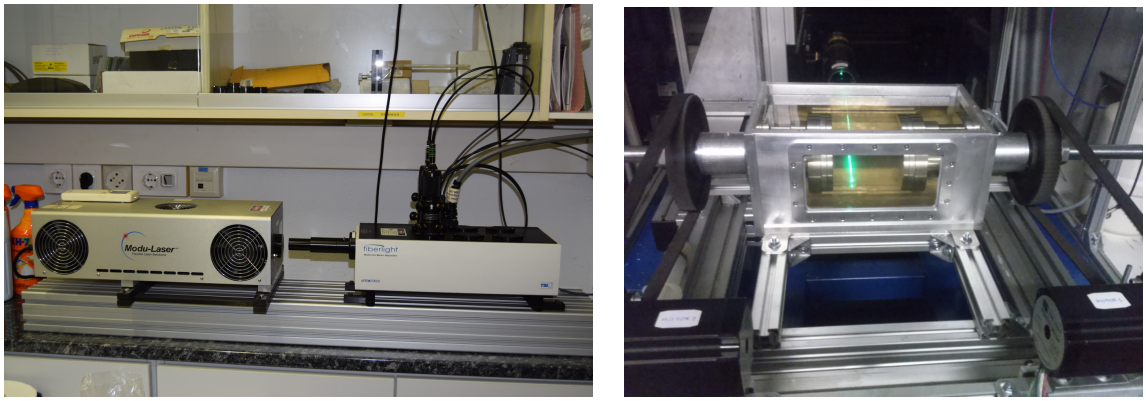
(a) (b)

Figure 5.3: (a) Picture of the rheometer and (b) measurement of the glycerine viscosity using a rheometer.

is less than 1% but this small error is significant since it is breaking the symmetries. One effect of breaking the symmetries does not allow the system to contain static waves. Instead, very slow rotating waves are expected.

5.2 Measurements

Two techniques are projected to obtain measurements of the flow velocity. Laser Doppler Anemometry (LDA) and Particle Image Velocimetry (PIV). Both of them required the use of a laser. The laser employed in this experiment for LDA measurements is an Argon laser which can generate three colors. Two of them were filtered and only the green one was used. Its wavelength is 314.5nm and power 3mW. LDA measurements require the use of two coherent laser beams. To ensure this property, both laser beams were obtained by splitting a single beam Figure 5.6 (a) shows a picture of the laser generator used for LDA. For the PIV measurements a double



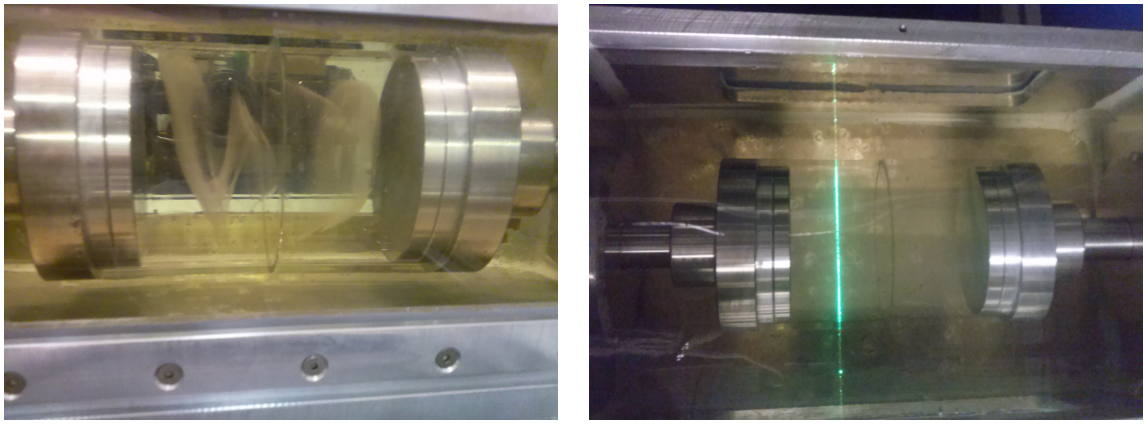
(a) (b)

Figure 5.4: (a) Picture of the laser generator and (b) picture of the experimental device with the laser on.

Nd-YAG laser will be used.

Using LDA technique, every instant is possible to measure only one component of the velocity in the area where two laser beams intersect. The desired component is contained in the coherent beams plane in the direction of connecting both beams. The area of intersection is an ellipse of dimensions 2.6 mm and 180 μm. The position of the laser beams with the experimental setup is illustrated in figure 5.6 (b). In that configuration, the device is prepared to measure the azimuthal velocity component.

Furthermore, the visualizations also need some particles to be able to trace the movement of the flow. It is important to include small particles which do not alter the flow properties. The visualizations were made using Silver-Coated Hollow glass spheres MD=8-12,100 cc. These particles are added to the flow using a syringe. After the injection, the particles are concentrated in some areas of the cylinder, see figure 5.5 (a) which shows a snapshots short time after the particles addition. However, before doing any measurement is it important to obtain a homogeneous mixture. Therefore, we provided movement to the cylinder to help the mixture of the particles until achieving



(a) (b)

Figure 5.5: (a) Picture of cylinder filled with particles and (b) picture of an even distribution of the particles.

an even distribution. Also note that if some air bubbles were included while injecting the particles, these bubbles have to be removed completely before any measurement. Figure 5.5 shows a snapshot of an even distributed mixture and the laser prepared to start measurements.

The laser is held in a traverse that allows its controlled movement. This transverse can control movement with the precision of 0.5 mm. Furthermore, to use LDA technique, since the laser beams to through different transparent surfaces an adjustment has to be made to calculate the area where both beams meet. The optics of the laser are calculated using the Snell laws which relate the angles of incidence and refraction. The refractive index of the liquid used has to be considered, in this case equal to 1.473. Figure 5.6 shows a scheme of the laser going through the different surfaces. The key of this process is to be able to calculate which position of the transverse corresponds to each point that is going to be measure. Note also that since the cylinder is a curve surface when the measurement of an equispaced grid inside of it is

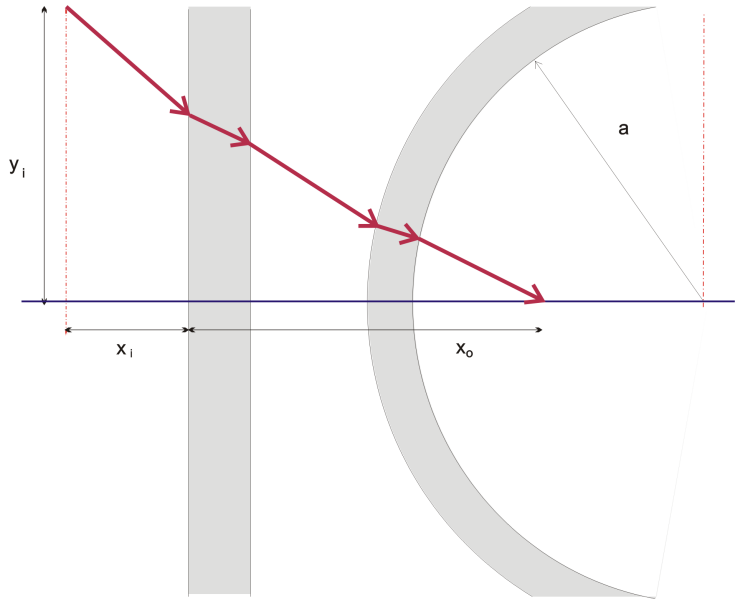


Figure 5.6: Scheme of the laser going through the different surfaces.

required, the change in the position of the transverse is not equispaced. This conversion between the movement of the laser and the displacement of the measurement point was automatized thus the transverse can be programmed to move automatically to generate a measurement grid mesh.

Before doing any LDA measurement, the laser has to be calibrated assuring the correct position of the laser. For doing so, the walls are used as a reference point because the system saturates in a very short time there making them easy to identify. This calibration prevents any possible error produced by an accidental displacement of the experimental table.

Figure 5.7 is an example of half-plane velocity map calculated with collected data using LDA technique for a case with the cylinder containing water with $\gamma = 1.2$ and $Re = 3808$ using a mesh of 6 radial points and 9 points in the z direction. To try to get a reliable measure, the system takes measures in each positioned during 2 minutes to have enough particles passing trough the area of intersection of both laser beams.

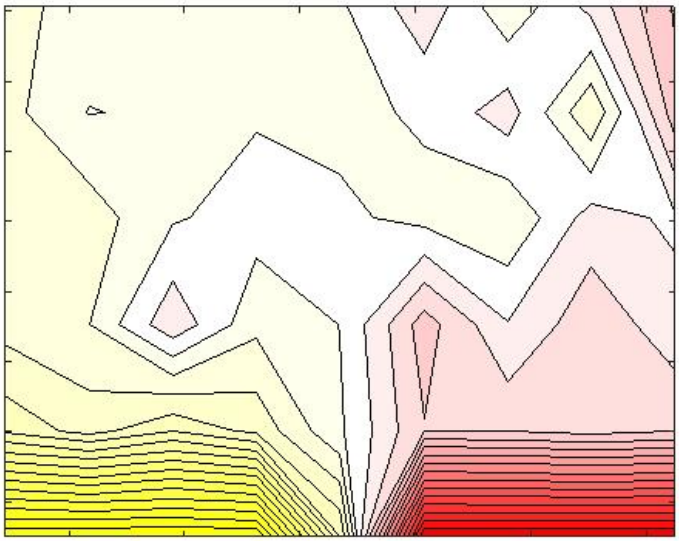


Figure 5.7: Velocity contour measured in a meridional plane for a case with the cylinder containing water for $\gamma = 1.2$ and $Re = 3808$.

From obtained measurements close to the wall of the cylinder we have the velocity of at least 14 particles for each point that is enough for reliable measurement. However, near the axis of the cylinder most of the mesh positions only contain 3 or 4 particles measurements which is not enough. This discrepancy is probably due to the problem with the alignment of both halves of the cylinder and has to be solved.

For the PIV measurement, the idea is different since this technique basically compares two pictures taken in a short interval and obtain the velocity of each particle measuring the space traveled provided the time elapsed. In this case, the laser is opened using a cylindrical lens to illuminate a plane and the camera located perpendicular to it. A transparent lid is needed to avoid the disturbances of the free surface in the picture. Since this lid was not ready during my stay time these measurements were not possible, but they are working progress now.

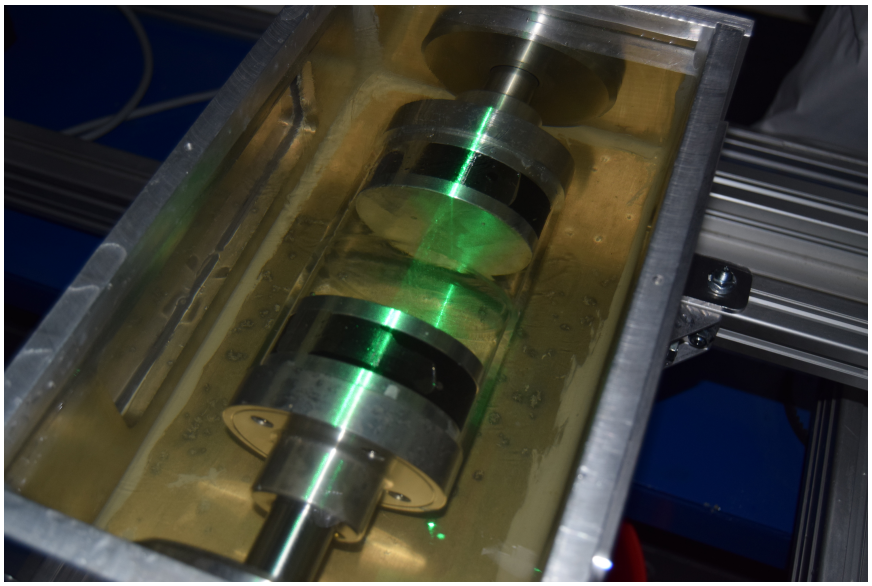


Figure 5.8: Snapshot of the pool with light up with a laser plane.

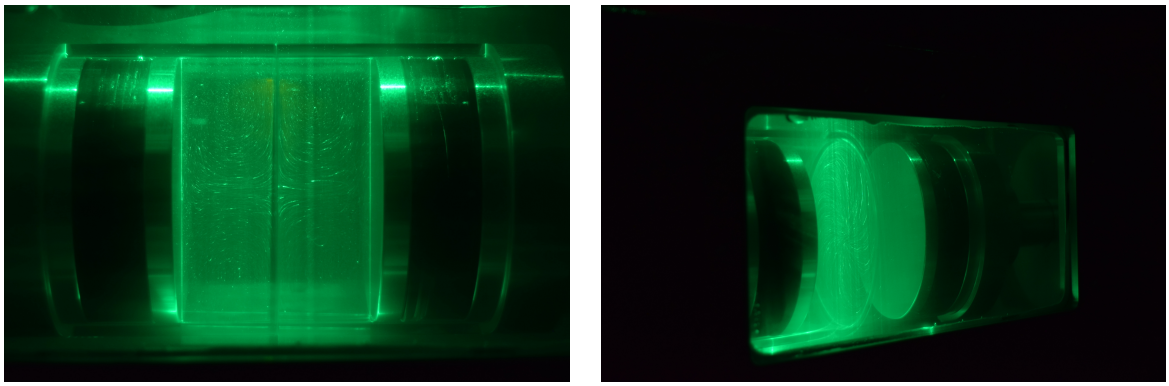


Figure 5.9: Snapshot of a light up of a rectangular and circular sections section at $Re = 136.56$.

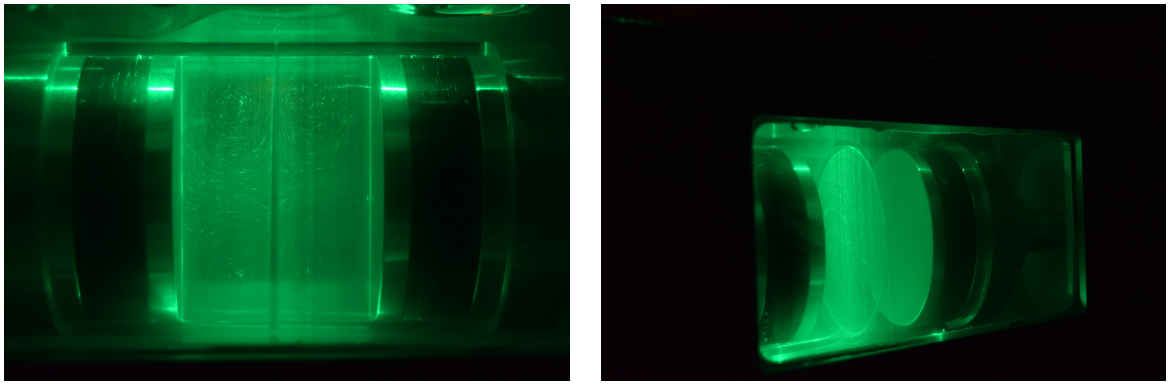


Figure 5.10: Snapshot of a light up of a rectangular and circular sections for at $Re = 236.71$.

Additionally, the laser plane generated can be used for vague visualizations obtained using with a high resolution camera. In this case we have used the Argon laser. To have a first insight of the flow behavior created for different halves speed visualizations were recorded for the range of 15-30KHz fixing $\gamma = 1.444$. This gamma was selected to be very close to $\gamma = 1.45$ which was extensively studied numerically. Figure 5.9 shows snapshots of a rectangular and circular sections for a case with a frequency equal to 15KHz equivalent to $Re = 136.56$. In the rectangular section, we can vaguely appreciate the recirculation sections. We can compare the results with figure 5.10 which shows snapshots of a rectangular and circular sections for a frequency equal to 26KHz equivalent to $Re = 236.71$ without observing a significant change in behavior.

Furthermore, the pictures previous presented are an instantaneous representation of the flow. However, it is useful to obtain the stream functions of the flow which were obtained using around 400 frames. Figure 5.11 shows the stream functions of the same two cases in which is possible to appreciate the recirculation cells. There is no clear difference between both solutions other than the clear increase of the speed. This result is no in agreement with the numerical results presumably due to the

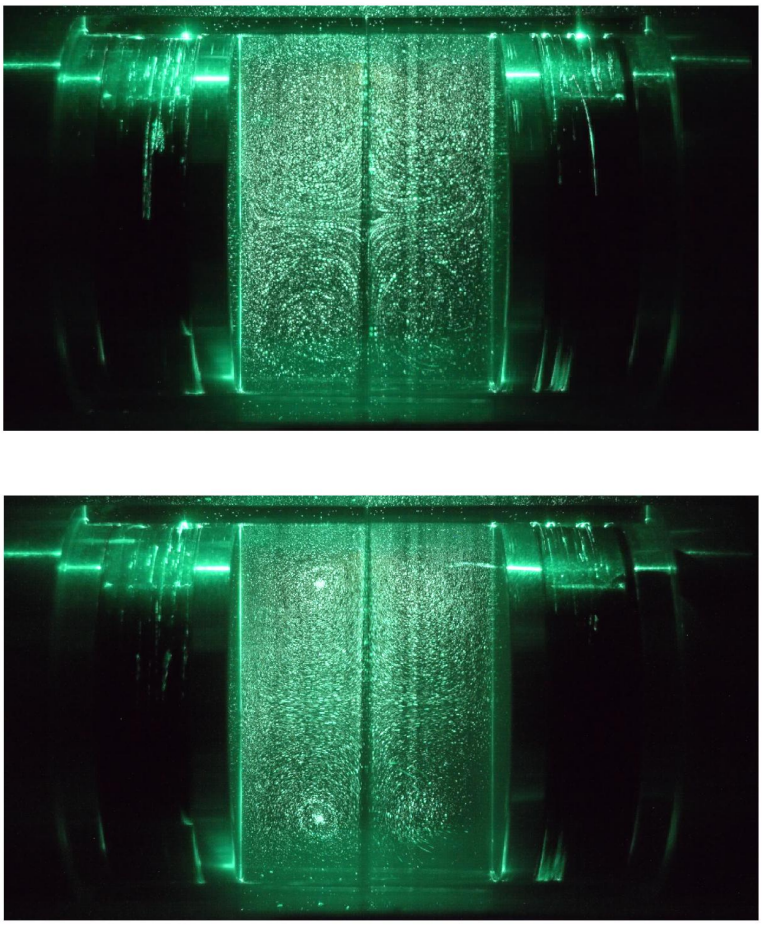


Figure 5.11: Stream functions calculated using the experimental visualizations for $Re = 136.56$ (top) and $Re = 236.71$ (bottom).

imperfections of the experimental device breaking the symmetries of the problem.

In conclusion, during the time I was working in Navarra, we were able to create a preliminary design for a setup and appreciate some of the expected features of the flow. However, the experimental device needed some improvements to retain the same symmetries that the numerical geometry has. Our collaborators have already solved some of these initial problems during their winter work, including a new pair of cylinders more circular and improving the alignment of both halves. These improvements, which are still in process, will allow to obtain measurements close enough to an ideal symmetric system.

Chapter 6

MODULATED DIFFERENTIALLY RAPIDLY ROTATING SPLIT CYLINDER FLOW

6.1 Abstract

The flow in a rapidly rotating cylinder is studied numerically. The cylinder is split in half, and the rapid rotation in the two halves is modulated harmonically with a small amplitude. We consider modulation frequencies ranging from zero to twice the background rotation frequency, so that the system supports inertial waves. The split in the cylinder at mid-height provides a localized perturbation from which inertial wave beams emanate, but so too do the corners where the endwalls and the sidewall meet. There is no discontinuity in the boundary condition at these corners, but the thin modulated endwall and sidewall boundary layers meet at the corners and this leads to a localized perturbation to the rapid background rotation. This interaction produces inertial wave beams that over wide parameter regimes are more intense than those from the split at the cylinder mid-height. Due to finite viscosity and nonlinear flow conditions, the wave beams produce intricate patterns formed by constructive and destructive interference as they self intersect and reflect off cylinder boundaries and the axis. These patterns are very sensitive to the modulation frequency. Additionally, a phase difference between the modulations of the two cylinder halves was imposed. The phase difference impacts the symmetries of the system and its response to the modulations. In particular, some low-order Kelvin modes are driven resonantly, and their selection depends not only on the frequency but also on the phase of the differential modulation.

6.2 Introduction

The study of small perturbations to rapidly rotating flows has a long history, going back at least to Lord Kelvin [32]. Much fundamental insight has been gleaned by studying the linear inviscid limit; see the texts by Greenspan [24], and more recently by Davidson [17], for overviews. The linear inviscid theory results in a linear hyperbolic partial differential equation eigenvalue problem when the perturbation frequency ω_p is less than twice the solid-body rotation frequency Ω. The eigenmodes are called Kelvin modes. Being hyperbolic, the system supports waves – inertial waves. The group velocity of the inertial waves, which is the velocity at which energy propagates away from a disturbance in the form of wave-packets, is perpendicular to their phase velocity. Thus a wave-packet propagates at right angles to the apparent direction of propagation of the wave crest. The inertial waves travel in the direction of the characteristics – the so-called rays, and in cylindrical geometries, they travel on cones of angle $\beta = \arccos(\omega_p/2\Omega)$ with respect to a plane normal to the rotation axis. In a weakly nonlinear, almost inviscid setting, the characteristics are regularized into wave beams. These have been visualized in many experimental settings, and simulated numerically as well, by subjecting the system to spatially localized harmonic forcing [23]. In the experimental and numerical studies, the perturbed solid-body rotation flow is confined in a container and subjected to some particular forcing. Numerous container geometries have been considered, including spheres, spherical shells, cylinders, annuli and cubes, and the perturbations have been forced in a variety of ways, including precession, libration and differential rotation of parts of the container boundary (see [43, 58] for recent reviews). From the dispersion relation, it is clear that the perturbation frequency plays an important role in determining the flow response to the forcing. The spatial symmetry of the forcing also seems to play a

role in determining the response [7], but this is an aspect that has not receive much attention and motives our study.

We select a simple geometry, a circular cylinder, and a class of perturbations that allows us to explore the role of symmetry. In order to keep the flow relatively simple, the chosen perturbations do not alter the direction of the mean rotation vector, keeping it aligned with the cylinder axis. This, together with restricting the forced perturbations to be of small amplitude keeps the flow axisymmetric. Specifically, we consider the split-cylinder arrangement, where the cylinder is split at mid-height and the two halves rotate differentially. Both halves rotate very fast so that their rotation period is very short compared to the viscous diffusion time scale, and the periodic modulations of their mean rotation rates are of very small magnitude. We impose the same period of modulation on the two halves, so that the system is periodically forced, but consider variations in the phases. This phase variation allows us to consider forcings that are either symmetric or non-symmetric about the cylinder mid-height. In particular, when the two cylinder halves are modulated in phase, the modulation is the well-studied libration case [10, 55, 71, 86, 88, 101]. In this case, the system is equivariant to a reflection about the mid-height. In contrast, when the two halves are modulated exactly out of phase, the system is equivariant to a spatio-temporal symmetry corresponding to the reflection composed with a half-period translation in time, and for any other phase difference there is no spatial or spatio-temporal symmetry in the axial direction. In the following sections, we report on numerical simulations detailing how the various forced modulations lead to different responses in the flow that not only depend on the frequency (as has been previously studied), but also on the phase difference, and how the dependence on the phase difference is intrinsically tied to the symmetry of the system.

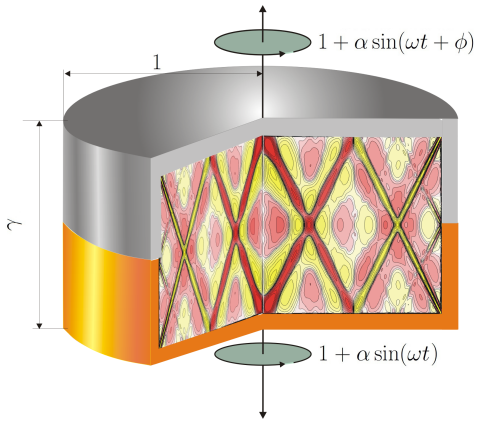


Figure 6.1: Schematic of the flow system. The inset shows azimuthal vorticity η for $Re = 10^6$, $\gamma = 1$, $\alpha = 10^{-4}$, $\omega = 0.88$ and $\phi = \pi$.

6.3 Governing Equations and Numerical Methods

Consider a circular cylinder of radius a and height h, filled with a fluid of kinematic viscosity ν, rotating with a mean angular speed Ω. The cylinder is split in two at its mid-height. The rotations of the two halves are subjected to modulations with the same amplitude and frequency, but with a relative a phase difference between the two. The flow is governed by the Navier–Stokes equations, which are non-dimensionalized by using a as the length scale and $1/\Omega$ as the time scale to give

$$(\partial_t + \boldsymbol{u}\cdot\nabla)\boldsymbol{u} = -\nabla p + \frac{1}{Re}\nabla^2\boldsymbol{u}, \qquad \nabla\cdot\boldsymbol{u} = 0, \tag{6.1}$$

where $Re = \Omega a^2/\nu$ is the Reynolds number, p is the pressure, and $\boldsymbol{u} = (u, v, w)$ is the velocity field in cylindrical coordinates $(r, \theta, z) \in [0, 1] \times [0, 2\pi] \times [-\gamma/2, \gamma/2]$, where $\gamma = h/a$ is the aspect ratio, and the corresponding vorticity field is $\nabla \times \boldsymbol{u} = (\xi, \eta, \zeta)$. In rotating flows, the Ekman number is often used instead of the Reynolds number, where $\mathrm{Ek} = \nu/(2\Omega\, h^2) = 1/(2Re\,\gamma^2)$.

The boundary conditions are no-slip; on all walls the radial and axial velocity

components are zero, $u = w = 0$, and only the azimuthal component is non-trivial:

$$\begin{aligned}
&\text{top endwall, } z = \gamma/2: && v = r[1 + \alpha \sin(\omega t + \phi)],\\
&\text{bottom endwall, } z = -\gamma/2: && v = r[1 + \alpha \sin(\omega t)],\\
&\text{top half of sidewall, } r = 1,\ z \in (0, \gamma/2]: && v = 1 + \alpha \sin(\omega t + \phi),\\
&\text{bottom half of sidewall, } r = 1,\ z \in [-\gamma/2, 0): && v = 1 + \alpha \sin(\omega t),
\end{aligned} \tag{6.2}$$

where α, ω and ϕ are the amplitude, frequency and phase of the modulation. The forcing amplitude α can be thought of as Rossby number Ro measuring the differential rotation with respect to the background rotation. A schematic of the flow system is shown in Fig. 6.1.

Since we are interested in the response to small amplitude periodic perturbations to solid-body rotation, we shall fixed $\alpha = 10^{-4}$. For such weak forcing, the flow is expected to remain axisymmetric, and so we only consider here the axisymmetric Navier–Stokes equations. The axisymmetric Navier–Stokes equations (6.1) together with the boundary conditions (6.2) are solved numerically using a second-order time-splitting method, with space discretized using Chebyshev collocation points in r and z:

$$\boldsymbol{u}(r, z, t) = \sum_{n=0}^{2n_r+1} \sum_{m=0}^{n_z} \hat{\boldsymbol{u}}_{mn}(t) \Xi_n(r) \Xi_m(2z/\gamma), \tag{6.3}$$

where Ξ_n is the n-th Chebyshev polynomial. The spectral solver is based on that described in [66] and it has been used extensively in a wide variety of enclosed cylinder flows. Since the system is harmonically forced, it is convenient to have an integer number of time-steps n_t per modulation period $\tau = 2\pi/\omega$, such that the time-step is $\delta t = \tau/n_t$. For the cases presented here, the required time resolution was $n_t = 10\,000$ and the spatial resolution was $n_r = 150$ and $n_z = 151$. This resolution provides at least seven collocation points in the boundary layers ensuring that they are well resolved.

The discontinuous sidewall boundary condition can lead to Gibb's phenomenon

when using a spectral solver. To avoid this, the discontinuity was regularized over a small distance. Specifically, the boundary condition for v at the sidewall is replaced by

$$\begin{aligned} v(r=1,\theta,z) &= 1+\alpha\tanh(\epsilon z)\sin(\omega t+\phi), \qquad && \text{for } z\in(0,\gamma/2], \\ v(r=1,\theta,z) &= 1+\alpha\tanh(\epsilon z)\sin(\omega t), && \text{for } z\in[-\gamma/2,0), \end{aligned} \tag{6.4}$$

where ϵ governs the distance over which the discontinuity is smoothed out. Based on a study of this type of regularization for the same cylindrical geometry [25], $\epsilon = 50$ was selected.

The axisymmetric Navier–Stokes equations are invariant to arbitrary translations in time and to a reflection in z; the action of these symmetries on the velocity $\boldsymbol{u}$ and the vorticity $\boldsymbol{\nabla}\times\boldsymbol{u} = (\xi,\eta,\zeta)$ are:

$$\begin{aligned} \mathcal{T}_\rho(u,v,w,\xi,\eta,\zeta)(r,z,t) &= (u,v,w,\xi,\eta,\zeta,)(r,z,t+\rho), \quad \text{for any real } \rho, \\ \mathcal{K}(u,v,w,\xi,\eta,\zeta)(r,z,t) &= (u,v,-w,-\xi,-\eta,\zeta)(r,-z,t). \end{aligned} \tag{6.5}$$

However, the boundary conditions (6.2) are not invariant to either of these symmetries in general. The system (equations and boundary conditions) is equivariant to a specific temporal symmetry $\mathcal{T}_\tau$ due to the harmonic forcing, for any phase difference ϕ. Also, for any value of ϕ, the flow for $-\phi$ is obtained from the flow for ϕ by applying $\mathcal{T}_{-\phi/\omega}\mathcal{K}$ to it, so that only $\phi\in[0,\pi]$ need be considered. The system is invariant to the reflection $\mathcal{K}$ only for $\phi = 0$ (libration). For $\phi = \pi$, where the two cylinder halves are half a period out of phase, the system is invariant to the spatio-temporal reflection $\mathcal{T}_{\tau/2}\mathcal{K} = \mathcal{H}$, whose action is

$$\mathcal{H}(u,v,w,\xi,\eta,\zeta)(r,z,t) = (u,v,-w,-\xi,-\eta,\zeta)(r,-z,t+\tau/2). \tag{6.6}$$

For other values of ϕ, there are no spatial or spatio-temporal symmetries.

The aim of this study is to investigate the response to harmonic forcing in a regime that is close to the linear inviscid regime. This regime is asymptotically reached

with $Re \to \infty$ and $\alpha \to 0$. Numerically, we approximate this regime by taking Re large and α small. Specifically, in this study we fix $Re = 10^6$ and $\alpha = 10^{-4}$, and consider variations in the forcing frequency, $\omega \in (0, 2]$, and phase, $\phi \in [0, \pi]$. Note that $Re = 10^6$ corresponds to Ekman number $\mathrm{Ek} \sim 5 \times 10^{-7}$ (depending on γ), which is one to two orders of magnitude smaller than what is typically accessible in laboratory experiments involving measurements of inertial waves and beams.

6.4 Results

6.4.1 Response with $\phi = \pi$

We begin by considering the response when the modulations of the two cylinder halves are out of phase by exactly half a period, i.e. $\phi = \pi$. The consequences of changing the forcing frequency are illustrated in Fig. 6.2, which shows snapshots of the azimuthal vorticity η in a meridional plane, $(r, z) \in [0, 1] \times [-\gamma/2, \gamma/2]$, for several different ω. These and all subsequent contour plots of η in this paper are shown at the same phase of the modulation, corresponding to when $t = (k + 1/2)\tau$, with k an arbitrary integer and $\tau = 2\pi/\omega$ is the modulation period. Also, all the contour plots of η use the same contour levels and color map (detailed in the caption of Fig. 6.2), so that they can all be directly compared for the different values of ω, γ and ϕ used. As ω varies, the beam angle changes in accord with the dispersion relation. The beams emerging from the corners are more intense than those emerging from the sidewall split, irrespective of the value of ω. This is due to the secondary flow in the endwall boundary layers being periodically pumped into the corner region, resulting in a large amplitude perturbation there, whereas the boundary layer flow in the region of the sidewall split is relatively weak. Furthermore, the finite viscosity and nonlinearity lead to constructive and destructive interactions between the beams as they intersect,

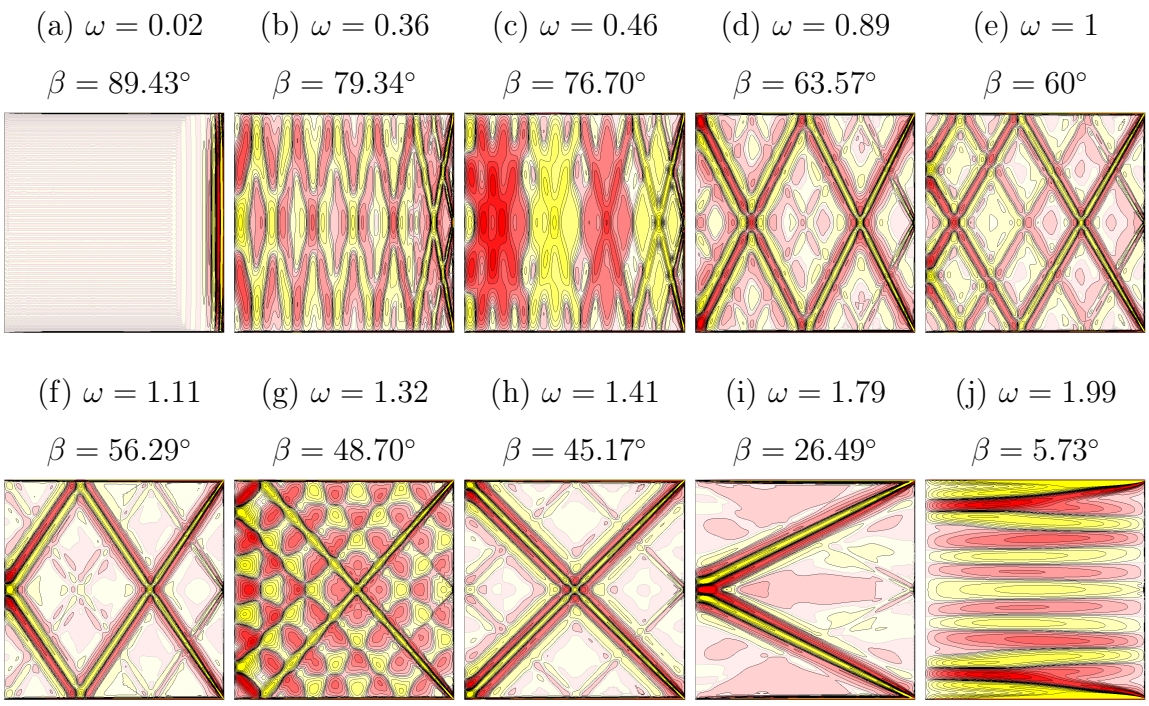


Figure 6.2: Azimuthal vorticity contours in the meridional plane $(r, z) \in [0, 1] \times [-\gamma/2, \gamma/2]$, with $\phi = \pi$ at various ω as indicated (the corresponding beam angle β according to the dispersion relation is also indicated). An animation of snapshots at the same phase of the period for frequencies $\omega = 0.01i$ for $i \in [2, 200]$ is available online. There are ten contour levels in the range $\eta \in [-0.0005, 0.0005]$, quadratically spaced, with positive being red and negative being yellow. Note that all isocontour plots in this paper use the same contour levels and color map.

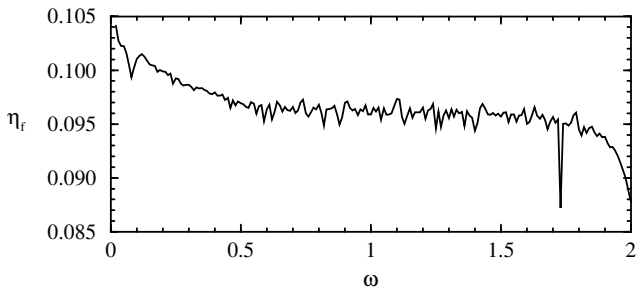


Figure 6.3: Variation of η_{f} with forcing frequency ω for $\gamma = 1$ and $\phi = \pi$.

producing large variations in the intensity of η with small changes in ω. The online movie shows an animation of η contours, with each frame corresponding to $\omega = 0.01i$ for $i \in [2, 200]$, illustrating how the beams behave as they cross and reflect off walls and the axis.

In order to quantify the intensity of the response in the bulk to the harmonic forcing, we use the maximum of $|\eta|$ (which is zero for solid-body rotation) over the forcing period τ and the cylindrical domain $\mathcal{D}$, $\eta_{\mathrm{f}} = \max_{\mathcal{D}}^{\tau} |\eta|$. Figure 6.3 shows how η_{f} varies with ω; the figure includes results for $\omega = 0.01i$ with $i \in [2, 200]$. For $\omega \in (0.5, 1.8)$ there is very little variation in η_{f}, which is in sharp contrast to what one would expect from viewing the η contours in Fig. 6.2 and the online movie, which give the impression of very intense η for particular values of ω. On closer inspection, the lack of peak responses in Fig. 6.3 is attributable to having used the whole cylindrical domain to determine η_{f}; the maximum in η occurs in the very thin boundary layers on the top and bottom endwalls. Hence, in order to quantify the response to the modulation in the bulk flow, the contributions from the boundary layers should be excluded.

We now estimate the boundary layer thickness in order to exclude their contribution. The thickness of the endwall boundary layers varies with ω, as is to be expected for an oscillating Ekman boundary layer. This type of boundary layer was previously

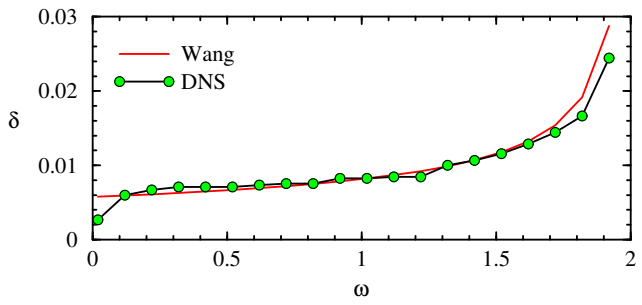


Figure 6.4: Endwall boundary layer thickness δ obtained from simulations (DNS) and estimated using Wang's theory [101] with $c = 8.14$.

studied for a librating cylinder [101], and the same analysis is applicable to the split cylinder with arbitrary ϕ. In terms of the non-dimensional parameters used here, the boundary layer analysis of Wang [101] gives the endwall boundary layer thickness, for $\omega < 2$, to be $\delta = c/\sqrt{|\omega - 2|Re}$, where δ is the boundary layer thickness divided by the height of the cylinder and c is a constant of proportionality. In order to compare the boundary layer thickness obtained from our simulations (DNS) with the estimates of [101], we have measured the thickness of the boundary layer using the azimuthal vorticity, taking the edge of the boundary layer to be where the fluid is rotating almost as solid body rotation, with $\eta \approx 0$. Although the endwall boundary layer is not of uniform thickness, the variations are negligible, and so we report the thickness at $r = 0.8$. Furthermore, even though the boundary layer is oscillatory, its thickness is time invariant. This was already noted for the libration case, with $\phi = 0$, [55], and here we have also found this to be the case for $\phi \neq 0$.

Figure 6.4 shows a comparison between δ obtained from simulations (DNS) and the theoretical prediction from Wang [101], with $c = 8.14$. The agreement is generally very good, with some discrepancies at the extreme values of ω. For $\omega \approx 2$, Wang's estimate becomes unbounded. Determining δ from the simulations for $\omega \approx 2$ is also

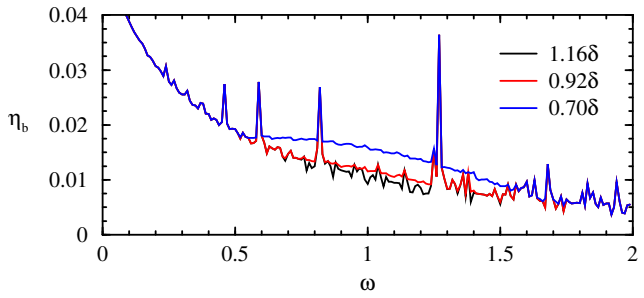


Figure 6.5: Variation of η_{b} with ω, for $\gamma = 1$ and $\phi = \pi$, with the excluded portions of the boundary layers indicated.

troublesome as the beams at these frequencies are nearly horizontal and it becomes difficult to distinguish between the edge of the boundary layer and the beams.

With an estimate of the boundary layer thickness δ in hand, we now consider the maximum of $|\eta|$ over a period and over the cylindrical domain excluding the boundary layer regions, $\eta_{\mathrm{b}} = \max^{\tau}_{\mathcal{D}/\mathcal{B}} |\eta|$. The thickness of the endwall boundary layers is calculated using Wang's scaling, with a modification to avoid the unrealistic effect of δ becoming unbounded for $\omega \sim 2$. The modification is to fix the maximum thickness for the exclusion zone at the endwalls to be no larger than 4% of the cylinder height. In contrast, the sidewall boundary layer thickness does not vary with ω, and a fixed value of 0.66% of the cylinder radius is excluded for all cases. The robustness of the results to variations in the excluded boundary layer regions was checked by using slightly different multiples of δ to define the exclusion zone. Figure 6.5 shows η_{b} determined using various multiples near one of δ to define the boundary layer exclusion zones. It is evident that if all of the boundary layer is not removed when computing η_{b}, much of the response is swamped by boundary layer vorticity contributions. The difference in η_{b} between using 1.16δ and 0.92δ is very small, whereas η_{b} is noticeably larger for 0.70δ, especially for $\omega \in (0.5, 1.8)$; this being due to residual contributions

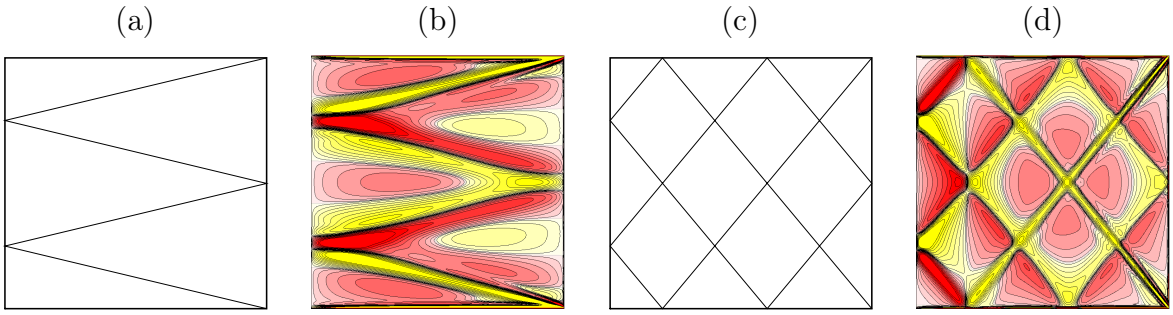


Figure 6.6: Retracing rays (a) R_{41} at $\omega = 1.94$, and (c) R_{45} at $\omega = 1.25$ and, (b, d) η contours at the corresponding frequencies with $\phi = \pi$.

from the parts of the boundary layers that were not excluded. Hence all the results we will present for η_{b} will use 1.16δ to ensure that the boundary layer is entirely excluded. Furthermore, the value of η_{b} at the peaks is invariant to how much of the boundary layer is excluded, indicating that the peaks are due to a bulk flow response to the modulations. It is also interesting to note that for $\omega \in (0.5, 1.8)$, $\eta_{\mathrm{b}}/\eta_{\mathrm{f}} \sim 0.1$.

6.4.2 Nonlinear Waves Beams, Inviscid Kelvin Modes and Retracing Rays.

In order to determine how the bulk flow responds to the modulations, particularly for frequencies corresponding to peak values in η_{b}, we check to see if those frequencies correspond to either low-order retracing rays or low-order Kelvin modes. The retracing rays are characteristics of the linear inviscid problem that retrace themselves after a certain number of reflections at the walls (and the axis). For the cases in which the beams only emerge from the corners, such as the $\phi = 0$ libration case, the corresponding retracing rays can be described by the number of reflections in the axial direction, $(n-1)$, and in the radial direction, $(k-1)$ [57]. Using n, k, and the aspect ratio of the cylinder, the beam angle is $\beta = \arccos(\omega/2) = \arccos(2n/\sqrt{n^2 + k^2\gamma^2})$. With $\phi = \pi$, since the cylinder is split exactly in half, the retracing rays associated

with beams starting at a corner and ending at the split, or starting and ending at the split, are equivalent to the retracing rays associated only with corners sources but for a cylinder of aspect ratio $\gamma/2$. These cases are equivalent to the retracing rays with k an even integer, associated only to corner beams in the cylinder of aspect ratio γ. Therefore, no extra cases have to be considered to account for the split cylinder geometry. Two examples of such retracing rays, R_{41} and R_{45} are shown in Figs. 6.6(a) and (c), together with the contours of η at the corresponding values of ω for $\phi = \pi$ in Figs. 6.6(b) and (d).

The peaks in $\eta_{\rm b}$ could also correspond to resonant forcing at the frequency of a low-order Kelvin mode. Kevin modes are the eigenfunctions of the inviscid Euler equations linearized about solid-body rotation. The azimuthal vorticity of the axisymmetric Kelvin eigenmodes K_{nk} are given by $\eta_{nk}(r,z) = J_1(\sigma_k r)\sin(n\pi[z/\gamma + 1/2])$, where n and k are positive integers and the frequency associated with K_{nk} is $\omega = 2\cos[\arctan(\gamma\sigma_k/n\pi)]$ (see [57] for details).

The frequencies associated with the low-order retracing rays R_{nk} and the low-order Kelvin modes K_{nk}, with $n \leq 5$ and $k \leq 5$, for three different γ, are listed in Table 6.1. Figure 6.7 shows the bulk flow response $\eta_{\rm b}$ to the modulation for three different aspect ratios; included are red squares corresponding to the frequencies associated with the low-order retracing rays and black triangles corresponding to the low-order Kelvin modes that are listed in Table 6.1. What becomes clear from the figure is that the predominant peaks in $\eta_{\rm b}(\omega)$ do not correspond to retracing rays, but that they in fact coincide with the frequencies corresponding to K_{1k} with $k \in [1,4]$. This feature of the bulk flow response is independent of γ.

The first row of Fig. 6.8 shows azimuthal vorticity contours of the Kelvin modes K_{1k} with $k \in [1,4]$, and the subsequent rows show the azimuthal vorticity contours from the simulations at the same frequencies, with different rows corresponding to the

	$\gamma = 1$	$\gamma = 0.8$	$\gamma = 0.6$		$\gamma = 1$	$\gamma = 0.8$	$\gamma = 0.6$
R_{11}	1.4142	1.5617	1.7150	K_{11}	1.2681	1.4315	1.6140
R_{12}	0.8944	1.0600	1.2804	K_{12}	0.8174	0.9769	1.1962
R_{13}	0.6325	0.7692	0.9713	K_{13}	0.5901	0.7202	0.9152
R_{14}	0.4851	0.5965	0.7692	K_{14}	0.4590	0.5654	0.7315
R_{15}	0.3922	0.4851	0.6325	K_{15}	0.3747	0.4638	0.6059
R_{21}	1.7889	1.8570	1.9157	K_{21}	1.7075	1.7975	1.8782
R_{22}	1.4142	1.5617	1.7150	K_{22}	1.3343	1.4916	1.6616
R_{23}	1.1094	1.2804	1.4866	K_{23}	1.0509	1.2222	1.4345
R_{24}	0.8944	1.0600	1.2804	K_{24}	0.8531	1.0156	1.2359
R_{25}	0.7428	0.8944	1.1094	K_{25}	0.7128	0.8608	1.0731
R_{31}	1.8974	1.9325	1.9612	K_{31}	1.8527	1.9019	1.9430
R_{32}	1.6641	1.7647	1.8570	K_{32}	1.6043	1.7184	1.8261
R_{33}	1.4142	1.5617	1.7150	K_{33}	1.3592	1.5137	1.6787
R_{34}	1.2000	1.3679	1.5617	K_{34}	1.1550	1.3248	1.5252
R_{35}	1.0290	1.2000	1.4142	K_{35}	0.9933	1.1635	1.3803
R_{41}	1.9403	1.9612	1.9779	K_{41}	1.9130	1.9430	1.9673
R_{42}	1.7889	1.8570	1.9157	K_{42}	1.7463	1.8261	1.8964
R_{43}	1.6000	1.7150	1.8238	K_{43}	1.5544	1.6787	1.7990
R_{44}	1.4142	1.5617	1.7150	K_{44}	1.3723	1.5252	1.6875
R_{45}	1.2494	1.4142	1.6000	K_{45}	1.2131	1.3803	1.5721
R_{51}	1.9612	1.9749	1.9858	K_{51}	1.9430	1.9630	1.9789
R_{52}	1.8570	1.9048	1.9448	K_{52}	1.8261	1.8834	1.9318
R_{53}	1.7150	1.8030	1.8818	K_{53}	1.6787	1.7758	1.8642
R_{54}	1.5617	1.6845	1.8030	K_{54}	1.5252	1.6550	1.7824
R_{55}	1.4142	1.5617	1.7150	K_{55}	1.3803	1.5323	1.6928

Table 6.1: Frequencies ω associated with retracing rays R_{nk} and Kelvin modes K_{nk}, for $n \in [1, 5]$ and $k \in [1, 5]$, and γ as indicated.

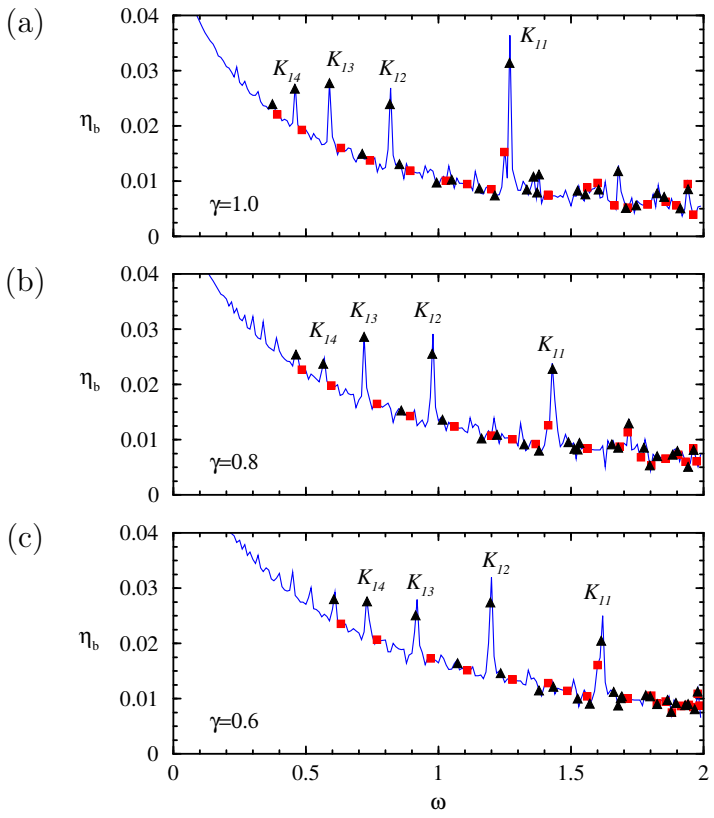


Figure 6.7: Variation with forcing frequency of the maximum value of azimuthal vorticity over the forcing period in the bulk flow (excluding the endwall and sidewall boundary layers to the level 1.16δ) for $\phi = \pi$ and γ as indicated. The red squares are the responses at frequencies corresponding to low-order retracing rays and the black triangles are the responses at frequencies corresponding to low-order Kelvin mode frequencies.

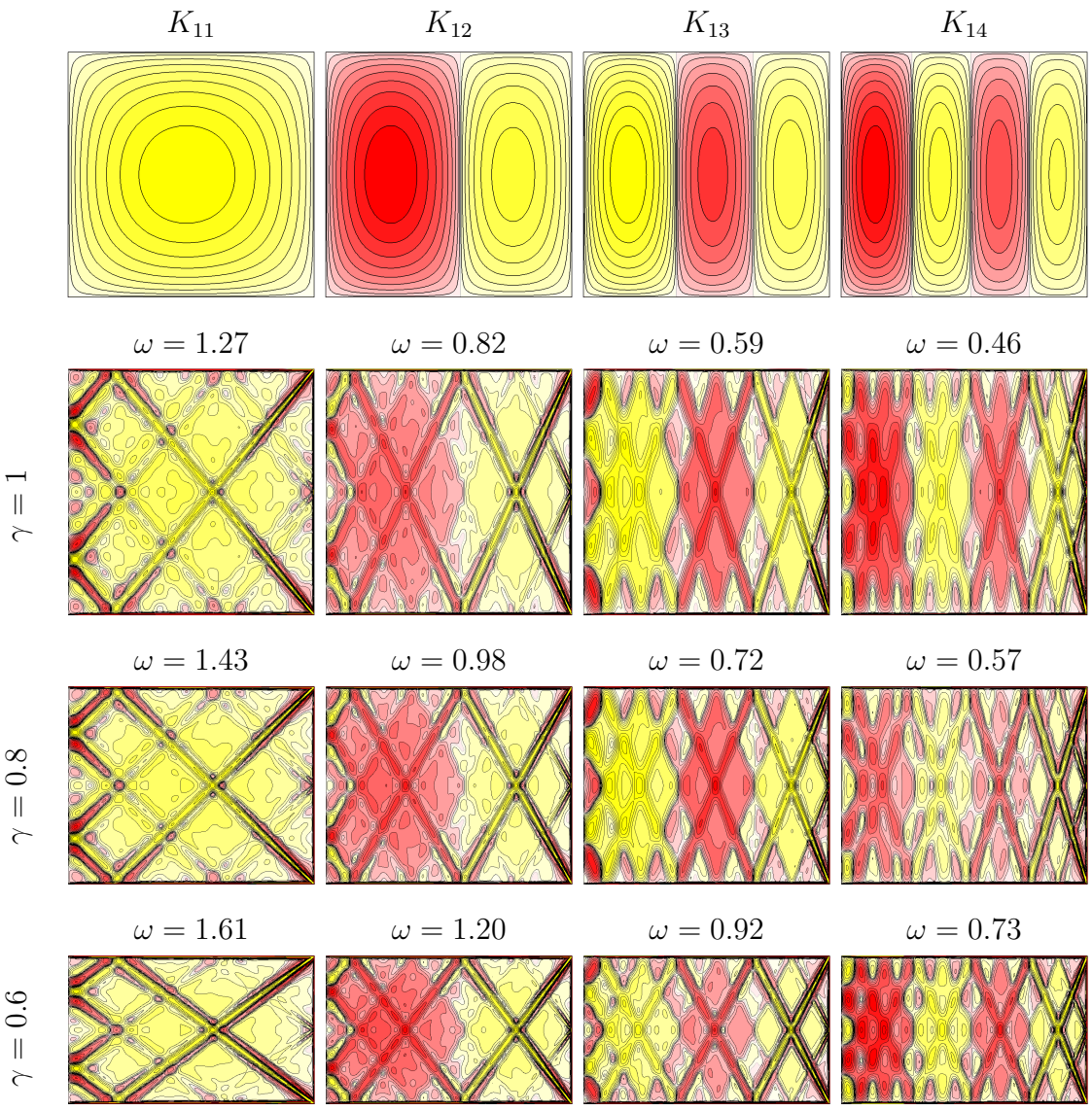


Figure 6.8: Comparison between the Kelvin eigenmodes (first row) and azimuthal vorticity contours at the resonant frequency, for $\phi = \pi$ and γ as indicated.

three aspect ratios shown in Fig. 6.7. Although the beams emanating from the corners and the sidewall split are striking, it is also striking that the bulk flow η has the same spatial distribution as in the Kelvin modes (compare red and yellow regions). Also evident from Fig. 6.8 is that for all the considered γ, the beams are very close to being retracing; this is a consequence of the frequencies associated with K_{11} being close to the frequencies associated with R_{45} (they differ by about 1–2%, however this is not necessarily a small difference). The beams for the other frequencies in the figure are also close to higher-order retracing rays (the corresponding frequencies are not listed in the Table 6.1). The point however, is not that there are retracing rays arbitrary close to the simulated peaks, but rather that the low-order retracing rays do not result in peaks. Notice also that for $\phi = \pi$ the flow is $\mathcal{H}$-symmetric and so are the odd axial Kelvin modes, which are associated with the bigger peaks in Fig. 6.7.

6.4.3 Influence of the Phase Difference

We now consider the impact of the phase difference between the harmonic forcing of the two cylinder halves. Figure 6.9 shows the variation of η_{b} with ω for five different values of ϕ. For $\phi = \pi$ (Fig. 6.9a, which essentially is the same as Fig. 6.6a and included here for ease of comparison with the rest of the cases), the peaks in η_{b} occur at frequencies ω corresponding to the frequencies of the leading odd axial Kelvin modes, K_{1j} with $j \in [1, 4]$, as discussed in the previous section. For $\phi = 3\pi/4$ (Fig. 6.9b), the larger peaks still correspond to the same Kelvin modes. Further decreasing ϕ (Figs. 6.9c and d), these same peaks are still present but their intensity is lower and some other peaks are evident. Finally, for $\phi = 0$ (the libration case, Fig. 6.9e), the peaks corresponding to the odd axial Kelvin modes disappear and instead, the peaks that are present correspond to frequencies of even axial Kelvin modes, K_{2j} with $j \in [1, 3]$; some of these are the additional peaks that were found in Figs. 6.9(c) and

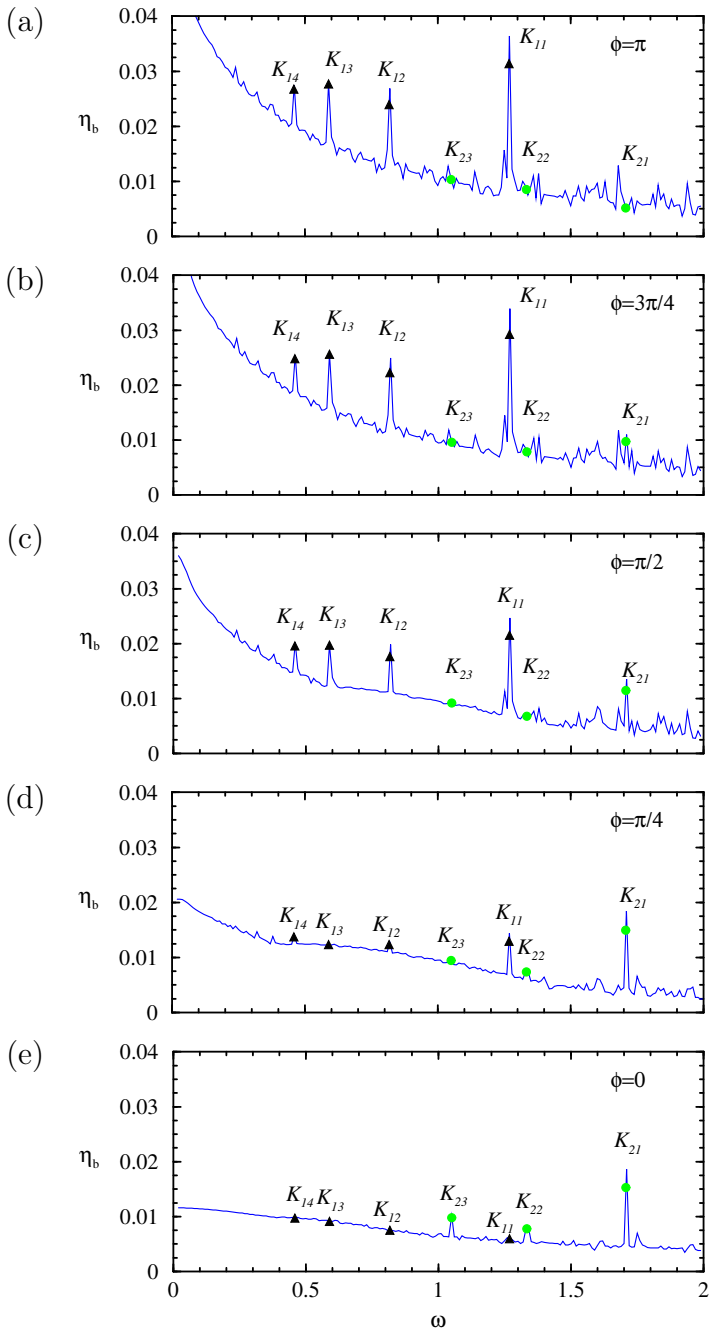


Figure 6.9: Variation of η_b with ω, for $\gamma = 1$ and ϕ as indicated. The black triangles are the responses at frequencies corresponding to K_{1k} with $k \in [1, 4]$ and the green circles corresponding to K_{2k} with $k \in [1, 3]$.

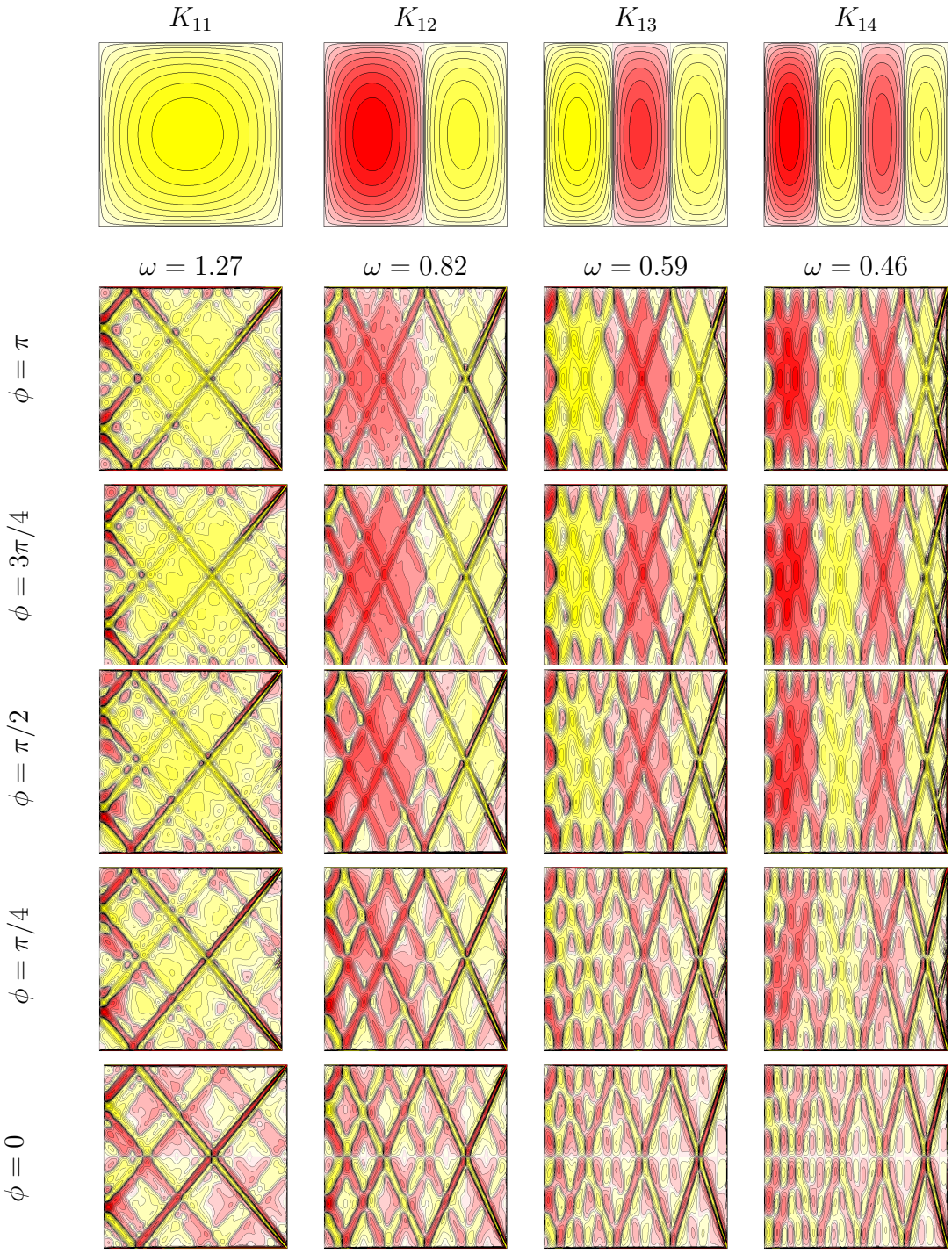


Figure 6.10: Comparison between the Kelvin modes and azimuthal vorticity contours at the given frequencies ω, corresponding to peaks in η_{b}, for $\gamma = 1$ and ϕ as indicated.

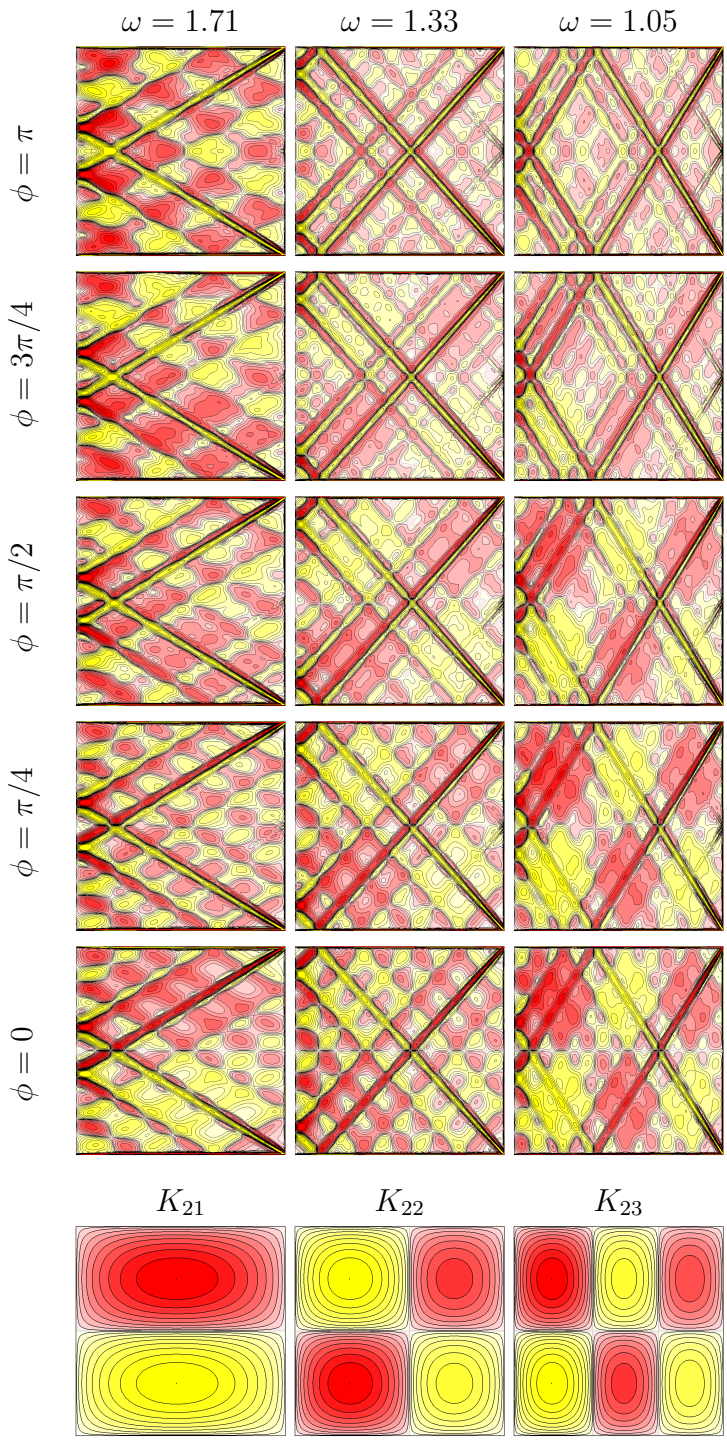


Figure 6.11: Comparison between the Kelvin modes and azimuthal vorticity contours at the given frequencies ω, corresponding to peaks in η_{b}, for $\gamma = 1$ and ϕ as indicated.

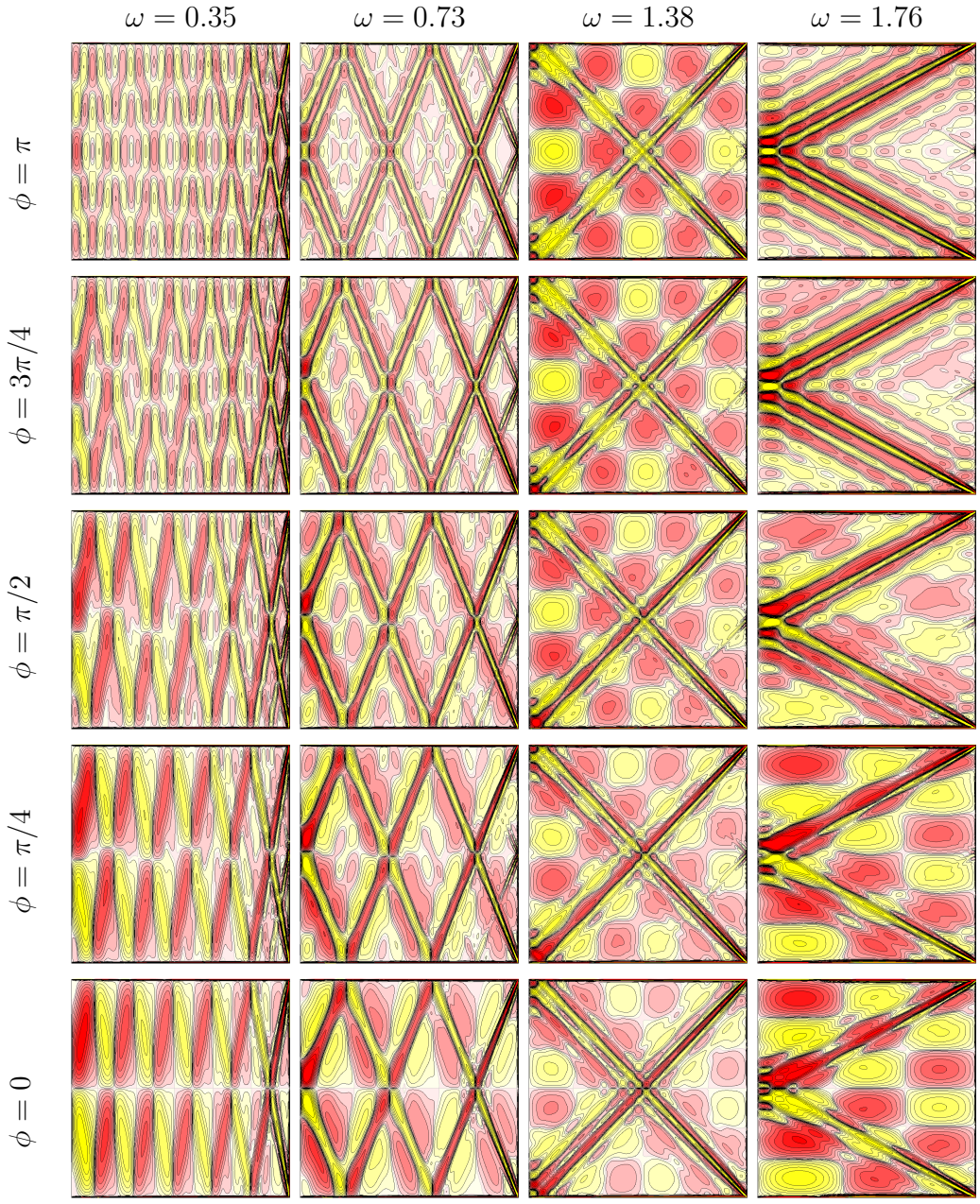


Figure 6.12: Azimuthal vorticity contours for $\gamma = 1$ at ω and ϕ as indicated.

(d), and are absent in Fig. 6.9(a).

Figure 6.10 shows snapshots of η at the frequencies corresponding to the odd Kelvin modes which correspond to the frequencies of the stronger peaks in η_{b} for $\phi = \pi$. The odd Kelvin modes are shown in the first row of the figure, and the other rows correspond to simulations at different ϕ. The flow structure is akin to the superposition of odd axial Kelvin modes and wave beams. With decreasing ϕ, the flow is slightly different, it loses the features associated with the odd axial Kelvin mode, but the beam structure persists. When $\phi = 0$, the flow no longer has features related to an odd axial Kelvin mode, but instead it is similar to an even axial Kelvin mode. This behavior with variable ϕ is consistent with the flow for $\phi = 0$ being $\mathcal{H}$ invariant, as are the odd Kelvin modes, whereas for $\phi = \pi$ the flow is $\mathcal{K}$ invariant, as are the even Kelvin modes. These results are congruent with the stronger peaks found for each case in Fig. 6.9.

In Fig. 6.11, we consider the leading even axial Kelvin modes in the first row, and the other rows show simulations at the corresponding frequencies for different ϕ. The similarities between the simulations for $\phi = 0$ and the even Kelvin modes is quite striking. With increasing ϕ, the flow still has features in common with the corresponding even Kelvin mode until $\phi = \pi$, in which case the flow characteristics are more similar to an odd Kelvin mode. The results illustrated in Figs. 6.10 and 6.11 indicate that the phase difference ϕ is crucial in the selection of which Kelvin mode is resonantly excited, and this selection is predicated by the symmetry of the system.

The influence of ϕ on the behavior of the bulk of the flow is remarkable even for ω not associated with peaks in $\eta_{\mathrm{b}}(\omega)$. Figure 6.12 shows snapshots of η for $\phi = \pi, 3\pi/4, \pi/2, \pi/4$ and 0 for various ω. The $\phi = \pi$ states are similar to even Kelvin modes and the $\phi = 0$ states are similar to odd Kelvin modes (similar in the sense that they have the same symmetry, $\mathcal{K}$ or $\mathcal{H}$). However, for the other ϕ values, for which

the system is neither $\mathcal{K}$ or $\mathcal{H}$ symmetric, the flows (which are not symmetric) can have similarities with one or the other case, or with neither of the odd or even Kelvin modes.

6.5 Discussion and Conclusion

We have studied the response to small amplitude harmonic forcing in a simple rapidly rotating system whose configuration can be tuned continuously between having a spatial reflection symmetry ($\mathcal{K}$) and a spatio-temporal reflection symmetry ($\mathcal{H}$). The rapid rotation regime corresponds to Ekman numbers $\mathrm{Ek} \sim 10^{-6}$, which is typically the lower limit achieved in laboratory experiments, and the considered forcing amplitude corresponds to a differential rotation Rossby number $Ro \sim 10^{-4}$. The low Ek puts us in the low-viscosity regime, while $Ro\mathrm{Ek}^{-1/2} \ll 1$ is needed for negligible nonlinear effects. We have $Ro\mathrm{Ek}^{-1/2} \sim 0.1$, so while the forcing amplitude is small, the response may still be too large to simply neglect nonlinear effects. Nevertheless, typical laboratory experiments have larger $Ro\mathrm{Ek}^{-1/2}$ due to signal-to-noise ratio constraints of their measurement techniques. We find that when the forcing has either $\mathcal{K}$ or $\mathcal{H}$ symmetry, the flow responds with peaks at frequencies corresponding to low order Kelvin modes with the same symmetry. This is consistent with the experimental observation of [7], but their system, a librating cube, had but a single symmetry group ($\mathcal{K}$). They concluded that it is of interest to consider other forcings that result in a system with what they call anti-symmetric modes (essentially this would correspond to a system with $\mathcal{H}$ symmetry, such as the $\phi = \pi$ case in our problem) to see if the odd axial Kelvin modes would be excited, and indeed we find that they are. They also suggested that it is of interest to examine what happens in systems with broken symmetry, and that corresponds to the cases with $\phi \neq 0$ and $\phi \neq \pi$. We find in these cases that both odd and even Kelvin modes can be excited, and the degree to which one or other is

excited depends on the degree to which the symmetries are broken.

Weak perturbations to rapidly rotating flows have responses which are not straight forward to predict. The very rapid rotation limit suggests that viscous effects may be small enough to neglect, and if the imposed perturbation levels are sufficiently small, then nonlinearities may also be negligible. In the classical approach to the problem, viscous terms in the governing equations are neglected, and the system is linearized by considering infinitesimal perturbations to solid-body rotation. For perturbation frequencies less than twice the rotation frequency, the resulting linear equation is of hyperbolic form. This oscillator system results from the restoring nature of the Coriolis force. The eigenmodes, Kelvin modes, are neutral, i.e. the real parts of the eigenvalues are zero. However, solid-body rotation is stable (viscous eigenmodes are damped) and the higher order eigenmodes are more rapidly damped. So to observe the eigenmodes in a physical setting, the perturbations need to be continuously applied. The details of this forcing will impact what is observed. For a damped oscillator system, the response is composed of both the eigenmodes of the unforced system (which are damped, and take care of the initial condition) and the forced response which is all that survives after some time. The expectation is that if the harmonic forcing has the spatio-temporal structure of one of the eigenmodes of the unforced system, then it can be resonantly excited with a very small amplitude forcing. Of course, in practice, one does not have complete control of the spatio-temporal structure of the forcing, but typically only controls boundary forcing at a selected frequency. Nevertheless, in practice, responses that have much in common with the target eigenmode result.

A complication, however, is that the harmonic forcing in the physical system often leads to the formation of boundary layers. In the singularly perturbed problem (neglecting viscous effects) these do not exist. In rapidly rotating flows, a fundamental issue is whether there is a one-to-one correspondence between solutions of the singularly

perturbed problem (Ek = 0) and the full problem ($0 < \mathrm{Ek} \ll 1$) [24]. Various asymptotic analyses have tried to address this issue, typically employing expansions based on $\mathrm{Ek}^{1/2}$, but have not been able to show one-to-one correspondence (e.g. [44]). Then there is the further issue of whether the nonlinear terms are negligible [104]. The problem here is subtle. On the one hand, you are relying on resonance in the very low viscosity limit using a very low amplitude forcing to excite an eigenmode to an observable level, but if it is observable it is because the flow deviation away from solid-body rotation is not small, and so nonlinear effects may not be negligible.

The harmonic forcing may excite a low order eigenmode, but temporally periodic viscous boundary layers are also formed. These tend to drive wave beams into the interior from corners along the characteristics of the linear inviscid system. These beams are omnipresent, and become narrower and more intense for smaller Ek. Note that they do not exist in the singularly perturbed system. So now we have that the solutions for Ek = 0 and $0 < \mathrm{Ek} \ll 1$ differ not only in the boundary layer regions, but also throughout the entire flow because of the presence of the beams.

At the end of the day, the details of how a rapidly rotating flow responds to small amplitude harmonic forcing requires the consideration of the full system of governing equations.

Chapter 7

CONCLUSION AND FUTURE WORK

The aim of this dissertation was bringing light to the behavior of the flow contained in a split-cylinder geometry by imposing different kinds of boundary conditions. This geometry was too unrepresented in literature, only some asymptotic cases for the differentially rotating case were previously studied. During this dissertation, it was shown that there exist a very rich variety of possible behaviors depending on imposed boundary conditions. The approach used to solve the flow in most of this dissertation was obtaining numerical results using spectral methods. A dynamical systems approach was used to characterize all the states and bifurcations for each of the geometries. Additionally, in Chapter 5 a preliminary experimental research is shown. This approach is still in progress, and it will be finished by our collaborators.

Since most of the work presented in this dissertation have been already published in international journals, the detailed conclusions for each particular geometry are included at the end of each chapter. Therefore, this final chapter only covers some general comments and remarks regarding the most significant finding in this dissertation without repeating previous conclusions.

In the differentially rotating case, different kind of instabilities were found creating for some of the cases three-dimensional waves which perturb the bulk of the cylinder whereas in other cases they remain in the boundary layer. It was found that always the first symmetry breaking is the axisymmetry making a three-dimensional study necessary.

In the counter-rotating case, it was found that our geometry can generate more helicity than the geometry of a cylinder with both lids counter-rotating which was

extensively studied in literature due to its application in dynamos of magnetic fields. Therefore, this split-cylindrical geometry could open a new branch of studies and applications.

In the oscillatory case, a phase difference was imposed between both halves of the cylinder creating a collection of different states. By changing this phase difference, different Kelvin modes are excited producing maximums in vorticity and therefore, helicity desired for many of the applications. This phase difference was not included in literature as far as we know and it is an interesting approach to open a new line of research.

In conclusion, it is possible to find a very rich variety of flows in the split-cylinder geometry and they were characterized along this dissertation. This geometry has some practical advantages respect to the geometries traditionally presented in literature making it an attractive line of research.

7.1 Future Work

Some of the initial problems of the experimental setup have been solved during the winter work in Navarra lab. Since then, an improved version of the experiment has been developed. From now on, there is a systematic and careful process necessary to acquire the measurements. This project is still in progress and our collaborators will continue working on it in the following years and it will be the main topic of Jesus Oscar Rodriguez-Garcia dissertation.

For that setup with counter-rotating cylinders, the symmetries of the problems are crucial for the behavior of the flow. Since in the experimental device is impossible to have exactly the speed of both halves, a numerical study of the effect of both halves of the cylinder rotating a slightly different speed is necessary. We want to

characterize the influence of this symmetry breaking parameter. Some preliminary results were obtained finding very slow rotating waves instead of stationary waves. These results were expected since the new system does not present O(2) symmetry. A more extensive study is needed, and it is a future line of investigation opened in this dissertation.

Furthermore, it is also possible to expand the study of split-cylinder flows imposing simultaneously other physical properties as temperature gradient or stratification but this is beyond the scope of this dissertation.

[1] Abshagen, J., M. Heise, C. Hoffmann and G. Pfister, "Direction reversal of a rotating wave in Taylor-Couette flow", J. Fluid Mech. **607**, 199–208 (2008).

[2] Albridge, K. D. and A. Toomre, "Axisymmetric inertial oscillations of a fluid in a rotating spherical container", J. Fluid Mech. **37**, 307–323 (1969).

[3] Armbruster, D., J. Guckenheimer and P. Holmes, "Heteroclinic cycles and modulated travelling waves in systems with $O(2)$ symmetry.", Physica D **29**, 257–282 (1988).

[4] Batchelor, G. K., "Note on a class of solutions of the Navier–Stokes equations representing steady rotationally-symmetric flow", Q. J. Mech. Appl. Math. **4**, 29–41 (1951).

[5] Blackburn, H. M. and J. M. Lopez, "Symmetry breaking of the flow in a cylinder driven by a rotating end wall", Phys. Fluids **12**, 2698–2701 (2000).

[6] Blackburn, H. M. and J. M. Lopez, "Modulated rotating waves in an enclosed swirling flow", J. Fluid Mech. **465**, 33–58 (2002).

[7] Boisson, J., C. Lamriben, L. R. M. Maas, P. P. Cortet and F. Moisy, "Inertial waves and modes excited by the libration of a rotating cube", Phys. Fluids **24**, 076602 (2012).

[8] Bourgoin, M., L. Marié, F. Pétrélis, C. Gasquet, A. Guigon, J.-B. Luciani, M. Moulin, F. Namer, J. Burguete, A. Chiffaudel, F. Daviaud, S. Fauve, P. Odier and J.-F. Pinton, "Magnetohydrodynamics measurements in the von Kármán sodium experiment", Phys. Fluids **14**, 3046–3058 (2002).

[9] Busse, F. H., "Mean zonal flows generated by librations of a rotating spherical cavity", J. Fluid Mech. **650**, 505–512 (2010).

[10] Busse, F. H., "Zonal flow induced by longitudinal librations of a roating cylindrical cavity", J. Fluid Mech. **240**, 208–211 (2010).

[11] Cortet, P., C. Lamriben and F. Moisy, "Viscous spreading of an inertial wave beam in a rotating fluid", Phys. Fluids **22**, 086603 (2010).

[12] Coullet, P. and G. Iooss, "Instabilities of one-dimensional cellular patterns", Phys. Rev. Lett. **64**, 866–869 (1990).

[13] Crawford, J. D. and E. Knobloch, "Symmetry and symmetry-breaking bifurcations in fluid dynamics", Phys. Rev. A **23**, 341–87 (1991).

[14] Crespo del Arco, E., J. J. Sánchez-Álvarez, E. Serre, A. de la Torre and J. Burguete, "Numerical and experimental study of the time-dependent states and the slow dynamics in a von Kármán swirling flow", Geophys. Astrophys. Fluid Dyn. **103**, 163–177 (2009).

[15] Crespo del Arco, E., E. Serre, P. Bontoux and B. E. Launder, "Stability, transition and turbulence in rotating cavities", in "Instability in Flows", edited by M. Rahman, pp. 141–195 (WIT Press, 2005).

[16] Dangelmayr, G., "Steady-state mode interactions in the presence of O(2)-symmetry", Dynamics and Stability of Systems **1**, 159–185 (1986).

[17] Davidson, P., *Turbulence in Rotating, Stratified and Electrically Conducting Fluids* (Cambridge, 2013).

[18] de la Torre, A. and J. Burguete, "Slow dynamics in a turbulent von Kármán swirling flow", Phys. Rev. Lett. **99**, 054101 (2007).

[19] Dijkstra, D. and G. J. F. van Heijst, "The flow between two finite rotating disks enclosed by a cylinder", J. Fluid Mech. **128**, 123–154 (1983).

[20] Fauve, S., S. Douady and O. Thual, "Drift instabilities of cellular patterns", J. Phys. II **1**, 311–322 (1991).

[21] Gauthier, G., P. Gondert, F. Moisy and M. Rabaud, "Instabilities of the flow between co and counter-rotating disks", J. Fluid Mech. **473**, 1–21 (2002).

[22] Giesecke, A., F. Stefani and J. Burguete, "Impact of time-dependent nonaxisymmetric velocity perturbations on dynamo action of von Kármán-like flows", Phys. Rev. E **86**, 066303 (2012).

[23] Görtler, H., "On forced oscillations in rotating fluids", in "Proceedings of the Fifth Midwestern Conference on Fluid Mechanics", pp. 1–10 (April 1–2, 1957).

[24] Greenspan, H. P., *The Theory of Rotating Fluids* (Cambridge University Press, 1968).

[25] Gutierrez-Castillo, P. and J. M. Lopez, "Instabilities of the sidewall boundary layer in a rapidly rotating split cylinder", Eur. J. Mech. B-Fluids **52**, 76–84 (2015).

[26] Gutierrez-Castillo, P. and J. M. Lopez, "Nonlinear mode interactions in a counter-rotating split-cylinder flow", J. Fluid Mech. **816**, 719–745 (2017).

[27] Hart, J. E. and S. Kittelman, "Instabilities of the sidewall boundary layer in a differentially driven rotating cylinder", Phys. Fluids **8**, 692–696 (1996).

[28] Hewitt, R. E. and A. L. Hazel, "Midplane-symmetry breaking in the flow between two counter-rotating disks", J. of Engineering mathematics **57**, 273–288 (2007).

[29] Higuera, M., H. Riecke and M. Silber, "Near-resonant steady mode interaction: periodic, quasi-periodic, and localized patterns", SIAM J. App. Dyn. Sys. **3**, 463–502 (2004).

[30] Hocking, L. M., "An almost-inviscid geostrophic flow", J. Fluid Mech. **12**, 129–134 (1962).

[31] Jones, C. A. and M. R. E. Proctor, "Strong spatial resonance and travelling waves in Bénard convection", Phys. Rev. A **121**, 224–228 (1987).

[32] Lord Kelvin, "Vibrations of a columnar vortex", Phil. Mag. **10**, 155–168 (1880).

[33] Kerswell, R. R., "On the internal shear layers spawned by the critical regions in oscillatory Ekman boundary layers", J. Fluid Mech. **298**, 311–325 (1995).

[34] Klein, M., T. Seelig, M. V. Kurgansky, A. Ghasemi V., I. Dan Borcia, A. Will, E. Schaller, C. Egbers and U. Harlander, "Inertial wave excitation and focusing in a liquid bounded by a frustum and a cylinder", J. Fluid Mech. **751**, 255–297 (2014).

[35] Kness, M., L. S. Tuckerman and D. Barkley, "Symmetry-breaking bifurcations in one-dimensional excitable media", Phys. Rev. A **46**, 5054–5062 (1992).

[36] Knobloch, E., "Symmetry and instability in rotating hydrodynamic and magnetohydrodynamic flows", Phys. Fluids **8**, 1446–1454 (1996).

[37] Krupa, M., "Bifurcations of relative equilibria", SIAM J. Math. Anal. **21**, 1453–1486 (1990).

[38] Kunen, R. P. J., H. J. H. Clercx and van Heijst G. J. F, "The structure of sidewall boundary layers in confined rotating rayleigh-benard convection", J. Fluid Mech. **727**, 509–532 (2013).

[39] Kuznetsov, Y. A., *Elements of Applied Bifurcation Theory* (Springer, 2004), third edn.

[40] Landsberg, A. S. and E. Knobloch, "Direction-reversing traveling waves", Phys. Rev. A **159**, 17–20 (1991).

[41] Lappa, M., *Rotating Thermal Flows in Natural and Industrial Processes* (John Wiley & Sons, 2012).

[42] Launder, B., S. Poncet and E. Serre, "Laminar, transitional, and turbulent flows in rotor-stator cavities", Phys. Fluids A **42**, 229–248 (2010).

[43] Le Bars, M., D. Cebron and P. Le Gal, "Flows driven by libration precession and tides", Annu. Rev. Fluid Mech. **47**, 163–193 (2015).

[44] Liao, X. and K. Zhang, "On viscous decay factors for spherical inertial modes in rotating planetary fluid cores: Comparison between asymptotic and numerical analysis", Phys. Earth Planetary Int. **169**, 211–219 (2008).

[45] Lopez, J. M., "Axisymmetric vortex breakdown: Part 1. Confined swirling flow", J. Fluid Mech. **221**, 533–552 (1990).

[46] Lopez, J. M., "Characteristics of endwall and sidewall boundary layers in a rotating cylinder with a differentially rotating endwall", J. Fluid Mech. **359**, 49–79 (1998).

[47] Lopez, J. M., "Rotating and modulated rotating waves in transitions of an enclosed swirling flow", J. Fluid Mech. **553**, 323–346 (2006).

[48] Lopez, J. M. and P. Gutierrez-Castillo, "Three-dimensional instabilities and inertial waves in a rapidly rotating split-cylinder flow", J. Fluid Mech. **800**, 666–687 (2016).

[49] Lopez, J. M., J. Hart, F. Marques, S. Kittelman and J. Shen, "Instability and mode interactions in a differentailly-driven roating cylinder", J. Fluid Mech. **462**, 383–409 (2002).

[50] Lopez, J. M., J. E. Hart, F. Marques, S. Kittelman and J. Shen, "Instability and mode interactions in a differentially-driven rotating cylinder", J. Fluid Mech. **462**, 383–409 (2002).

[51] Lopez, J. M. and F. Marques, "Small aspect ratio Taylor-Couette flow: Onset of a very-low-frequency three-torus state", Phys. Rev. E **68**, 036302 (2003).

[52] Lopez, J. M. and F. Marques, "Mode competition between rotating waves in a swirling flow with reflection symmetry", J. Fluid Mech. **507**, 265–288 (2004).

[53] Lopez, J. M. and F. Marques, "Centrifugal effects in rotating convection: nonlinear dynamics", J. Fluid Mech. **628**, 269–297 (2009).

[54] Lopez, J. M. and F. Marques, "Sidewall boundary layer instabilities in a rapidly rotating cylinder driven by a differentially co-rotating lid", Phys. Fluids **22**, 114109 (2010).

[55] Lopez, J. M. and F. Marques, "Instabilities and inertial waves generated in a librating cylinder", J. Fluid Mech. **687**, 171–193 (2011).

[56] Lopez, J. M. and F. Marques, "Rapidly rotating cylinder flow with an oscillating sidewall", Phys. Rev. E **89**, 013013 (2014).

[57] Lopez, J. M. and F. Marques, "Three-dimensional instabilities in a discretely heated annular flow: Onset of spatio-temporal complexity via defect dynamics", Phys. Fluids **26**, 064102 (2014).

[58] Lopez, J. M. and F. Marques, "Inertial waves in rapidly rotating flows: a dynamical systems perspective", Physica Scripta **91**, 124001 (2016).

[59] Lopez, J. M., F. Marques, I. Mercader and O. Batiste, "Onset of convection in a moderate aspect-ratio rotating cylinder: Eckhaus-Benjamin-Feir instability", J. Fluid Mech. **590**, 187–208 (2007).

[60] Lopez, J. M. and J. Shen, "An efficient spectral-projection method for the Navier-Stokes equations in cylindrical geometries I. Axisymmetric cases", J. Comput. Phys. **139**, 308–326 (1998).

[61] Machicoane, N., P. Cortet, B. Voisin and F. Moisy, "Influence of the multipole order of the source on the decay of an inertialwave beam in a rotating fluid", Phys. Fluids **27**, 066608 (2015).

[62] Marques, F., A. Y. Gelfgat and J. M. Lopez, "A tangent double Hopf bifurcation in a differentially rotating cylinder flow", Phys. Rev. E **68**, 016310 (2003).

[63] Marques, F. and J. M. Lopez, "Influence of wall modes on the onset of bulk convection in a rotating cylinder", Phys. Fluids **20**, 024109 (2008).

[64] Marques, F., J. M. Lopez and J. Shen, "Mode interactions in an enclosed swirling flow: a double Hopf bifurcation between azimuthal wavenumbers 0 and 2", J. Fluid Mech. **455**, 263–281 (2002).

[65] Marques, F., A. Meseguer, J. M. Lopez, J. R. Pacheco and J. M. Lopez, "Bifurcations with imperfect SO(2) symmetry and pinning of rotating waves", Proc. Roy. Soc. Lond. A **469**, 20120348 (2013).

[66] Mercader, I., O. Batiste and A. Alonso, "An efficient spectral code for incompressible flows in cylindrical geometries", Computers & Fluids **39**, 215–224 (2010).

[67] Moisy, F., O. Doare, T. Pasutto, O. Daube and M. Rabaud, "Experimental and numerical study of the shear layer instability between two counder-rotating disks", J. Fluid Mech. **507**, 175–202 (2003).

[68] Moisy, F., O. Doaré, T. Pasutto, O. Daube and M. Rabaud, "Experimental and numerical study of the shear layer instability between two counter-rotating disks", J. Fluid Mech. **507**, 175–202 (2004).

[69] Monchaux, R., M. Berhanu, M. Bourgoin, M. Moulin, P. Odier, J.-F. Pinton, R. Volk, S. Fauve, N. Mordant, F. Pétrélis, A. Chiffaudel, F. Daviaud, B. Dubrulle, C. Gasquet, L. Marié and F. Ravelet, "Generation of a magnetic field by dynamo action in a turbulent flow of liquid sodium", Phys. Rev. Lett. **98**, 044502 (2007).

[70] Munroe, J. R. and B. R. Sutherland, "Internal wave energy radiated from a turbulent mixed layer", Phys. Fluids **26**, 096604 (2014).

[71] Noir, J., M. A. Calkins, J. Cantwell and J. M. Aurnou, "Experimental study of libration-driven zonal flows in a straight cylinder", Phys. Earth Planetary Int. **182**, 98–106 (2010).

[72] Noir, J., G. Hemmerlin, J. Wicht, S. M. Baca and J. M. Aurnou, "An experimental and numercal study of librationally driven flow in planetary cores and subsurface oceans", Phys. Earth Planetary Int. **173**, 141–152 (2009).

[73] Nore, C., F. Moisy and L. Quartier, "Experimental observation of near-heteroclinic cycles in the von Kármán swirling flow", Phys. Fluids **17**, 064103 (2005).

[74] Nore, C., M. Tartar, O. Daube and L. S. Tuckerman, "Survey of instability thresholds of flow between exactly counter-rotating disks", J. Fluid Mech. **511**, 45–65 (2004).

[75] Nore, C., L. S. Tuckerman, O. Daube and S. Xin, "The 1:2 mode interaction in exactly counter-rotating von Karman swirling flow", J. Fluid Mech. **477**, 51–88 (2003).

[76] Nore, C., L. M. Witkowsi, E. Foucault, J. Pecheux, D. O. and P. Le Quere, "Competition betwwen axisymmetric and three-dimensional patters between exactly counter-rotating disks", Phys. Fluids **18**, 054102 (2006).

[77] Nore, C., L. M. Witkowski, E. Foucault, J. Pécheux, O. Daube and P. Le Quéré, "Competition between axisymmetric and three-dimensional patterns between exactly counter-rotating disks", Phys. Fluids **18**, 054102 (2006).

[78] Pacheco, J. R., J. M. Lopez and F. Marques, "Pinning of rotating waves to defects in finite Taylor–Couette flow", J. Fluid Mech. **666**, 254–272 (2011).

[79] Pecheux, J. and E. Foucault, "Axisymmetric instabilities between coaxial rotating disks", J. Fluid Mech. **563**, 293–318 (2006).

[80] Porter, J. and E. Knobloch, "New type of complex dynamics in the 1:2 spatial resonance", Physica D **159**, 125–154 (2001).

[81] Pratt, J. M., I. I. Rypina, T. M. Özgökmen, P. Wang, H. Childs and Y. Bebieva, "Chaotic advection in a steady, three-dimensional, Ekman-driven eddy", J. Fluid Mech. **738**, 143–183 (2014).

[82] Ravelet, F., L. Marie, A. Chiffaudel and F. Daviaud, "Multistability and memory effect in a highly turbulent flow: Experimental evidence for a global bifurcation", Phys. Rev. Lett. **93**, 164501 (2004).

[83] Ravelet, F., R. Monchaux, S. Aumaître, A. Chiffaudel, F. Daviaud, B. Dubrulle, M. Bourgoin, P. Odier, N. Plihon, J.-P. Pinton, R. Volk, S. Fauve, N. Mordant and F. Pétélis, "Chaotic dynamos generated by a turbulent flow of liquid sodium", Phys. Rev. Lett. **101**, 074502 (2008).

[84] Redekopp, L. G., "Side-wall boundary layers in rotating axial flow", J. Fluid Mech. **55**, 565–576 (1972).

[85] Rott, N. and W. S. Lewellen, "Boundary layers and their interactions in rotating flows", Prog. Aerospace Sci. **7**, 111–144 (1966).

[86] Rubio, A., J. M. Lopez and F. Marques, "Interacting oscillatory boundary layers and wall modes in modulated rotating convection", J. Fluid Mech. **625**, 75–96 (2009).

[87] Saric, W. S., "Görtler vortices", Annu. Rev. Fluid Mech. **26**, 379–409 (1994).

[88] Sauret, A., D. Cebron, M. Le Bars and S. Le Dizes, "Fluid flows in a librating cylinder", Phys. Fluids **24**, 026603 (2012).

[89] Schlichting, H. and K. Gersten, *Boundary-Layer Theory* (Springer, 2003), eighth edn.

[90] Smith, S. H., "The development of geostrophic flow within a split cylinder", J. Eng. Math. **25**, 137–150 (1991).

[91] Stewartson, K., "On the flow between two rotating coaxial disks", Proc. Cambridge Phil. Soc. **49**, 333–341 (1953).

[92] Stewartson, K., "On almost rigid rotations", J. Fluid Mech. **3**, 17–26 (1957).

[93] Strogratz, S. H., *Nonlinear dynamics and chaos* (Addisn-Wesley Publishing Company, 1994).

[94] Sutherland, B. R. and P. F. Linden, "Internal wave excitation from stratified flow over a thin barrier", J. Fluid Mech. **377**, 223–252 (1998).

[95] Tuckerman, L. S. and D. Barkley, "Bifurcation analysis of the eckhaus instability", Physica D **46**, 57–86 (1990).

[96] van Heijst, G. J. F., "The shear-layer structure in a rotating fluid near a differentially rotating sidewall", J. Fluid Mech. **130**, 1–12 (1983).

[97] Veronis, G., "The analogy between rotating and stratified fluids", Annu. Rev. Fluid Mech. **2**, 37–66 (1970).

[98] Vo, T., L. Montabone, P. Read and G. Sheard, "Non-axisymmetric flows in a differential-disk rotating system", J. Fluid Mech. **775**, 349–386 (2015).

[99] Vo, T., L. Montabone and G. Sheard, "Linear stability analysis of a shear layer induced by differential coaxial rotation within a cylindrical enclosure", J. Fluid Mech. **738**, 299–334 (2014).

[100] Vo, T., L. Montabone and G. Sheard, "Effect of enclosuse height on the structure and stability of shear layers induced by differential rotation", J. Fluid Mech. **765**, 45–81 (2015).

[101] Wang, C., "Cylindrical tank of fluid oscillating about a state of steady rotation", J. Fluid Mech. **41**, 581–592 (1970).

[102] Wood, W. W., "Inertial modes with large azimuthal wavenumbers in an axisymmetric container", J. Fluid Mech. **105**, 427–449 (1981).

[103] Zandbergen, P. J. and D. Dijkstra, "Von Kármán swirling flows", Annu. Rev. Fluid Mech. **19**, 465–491 (1987).

[104] Zhang, K. and X. Liao, "On the initial-value problem in a rotating circular cylinder", J. Fluid Mech. **610**, 425–443 (2008).

APPENDIX A

CO-AUTHOR PERMISSIONS

I certify that my co-author, Dr. Juan M. Lopez have given me permission, in writing, to include all material in my PhD thesis for Chapters 2,3 and 4.